
PROPERTIES OF ARCTIC AEROSOLS BASED ON PHOTOMETER LONG-TERM MEASUREMENTS IN NY-ÅLESUND



MASTER THESIS

SANDRA KAREN GRASSL
April 3, 2019

Supervisors:
Prof. Dr. Bernhard Mayer
Ludwig-Maximilians University Munich
Faculty of Physics
Meteorology

Dr. Christoph Ritter
Alfred Wegener Institute, Helmholtz Centre for polar and marine research, Potsdam
Section Physics of the Atmosphere

EIGENSCHAFTEN VON ARKTISCHEM AEROSOL ANHAND VON LANGZEIT-PHOTOMETERDATEN IN NY-ÅLESUND



MASTERARBEIT

SANDRA KAREN GRASSL
April 3, 2019

Betreuer:
Prof. Dr. Bernhard Mayer
Ludwig-Maximilians Universität München
Fakultät für Physik
Meteorologie

Dr. Christoph Ritter
Alfred-Wegener-Institut, Helmholtz-Zentrum für Polar- und Meeresforschung, Potsdam
Sektion Physik der Atmosphäre

Abstract

On the base of sun and star photometer measurements located at the German-French polar research base in Ny-Ålesund (78.923°N , 11.928°E), Svalbard, long-term changes (2001-2017 with focus on 2009-2017) of aerosol properties in the European Arctic are analysed. The main focus were physical aerosol properties like aerosol optical depth (AOD) or Ångström exponent, during the Arctic Haze season in spring compared to summer months. The presence of polar night and day is the limiting factor of available photometer measurement data. To get a full year-round data set a star photometer was also taken into account for the time between October and March.

In order to gain more information out of the measurement data of the photometers and to reduce the error of fitting the data to the Ångström law a new ansatz is also discussed in this thesis. With the radiative transfer calculator libRadtran artificial aerosol distributions were created to analyse the information content of real (noisy) photometer data. Indeed it was found that the new ansatz with wavelength dependent Ångström exponent reveals valuable information about the Arctic aerosol.

Monthly means of the measured AOD of the years 2009-2017 are compared with monthly means of previous studies to see changes in the properties of aerosol. Additionally, a comparison of sun and star photometer at the same site and the same years is also done.

Because photometer data has no height information a comparison with the Lidar is presented.

To study possible sources and sinks of aerosol, 5-days back-trajectories were calculated with the FLEXTTRA model at three different arriving heights (500m , 1000m and 1500m) at 12 UTC over Zeppelin Station, at Zeppelin mountain 474m above sea level and close to the village Ny-Ålesund.

Beside of the pathway of the aerosol into the European Arctic based on the calculated back-trajectories the influence of the lowermost 100hPa atmospheric layer is also analysed. Especially aerosol is highly affected by cloud formation and is removed out of the atmosphere by precipitation, areas with a high probability of cloud formation is also taken into account.

Contents

1. Introduction	7
2. Theory on tropospheric aerosol	9
2.1. Sources and sinks	10
2.2. Interaction of aerosols and molecules with radiation	12
2.3. Aerosol Optical Depth	13
2.4. Impact of aerosols on polar climate	15
3. Data Processing and Methods	18
3.1. Instruments	18
3.1.1. Raman Lidar "KARL"	18
3.1.2. Sun Photometer	19
3.1.3. Star Photometer	20
3.2. Data fitting and processing	26
3.3. Mie Calculus	35
3.4. Case study	41
3.5. Error Estimation	43
3.6. Back-trajectory analysis	44
4. Results	47
4.1. Trends in the AOD	47
4.1.1. Polar day	47
4.1.2. Polar night	50
4.2. Comparison of sun and star photometer	52
4.3. Trend of AOD over the whole year	54
4.4. Comparison with previous measurements	54
4.5. Aerosol load during polar night	55
4.6. Changes of heat transfer from mid latitudes	55
4.7. Aerosol load and properties	57
4.8. FLEXTTRA back-trajectories	59
4.8.1. Aerosol origin due to arriving air pollution	60
4.8.2. Aerosol sources and sinks	62
4.8.3. Remarks on the advection altitude	64
5. Conclusion	68
6. Outlook	69
7. Danksagung	76
A. Appendix	77
B. Abbreviations	86

1. Introduction



Figure 1: Location of Ny-Ålesund in Svalbard (source: <https://toposvalbard.npolar.no/>)

While technology in every part of life is becoming better and better, the humanity changes all ecosystems on Earth and also the atmosphere. Due to these changes both the weather and the climate change, especially in the Arctic. When both poles change their actual habit, it will influence also the life of people living in the mid-latitudes. The Arctic as a whole ecosystem can be seen as an early warning system for anthropogenic effects on the global climate. Especially here the impact is visible due to rapid decreases of glaciers and sea ice as well as an increasing active layer of the permafrost. The impact of increasing temperature is such large and reinforces itself, that it is known as Arctic Amplification (Pithan and Mauritsen, 2014). That's why lots of research is done at very remote places in high latitudes, like in Ny-Ålesund, a small research village in north-west of Svalbard.

As time goes by more and more fossil fuel is required to deal with the global need of energy for transport, industry and heating.

Most of the aerosol is emitted on the ground and mostly exuded into the lowermost 10 km of the atmosphere, the so-called troposphere. Also in this part of the atmosphere the weather takes place. Because water droplets can not be formed with a typical saturation in the atmosphere, aerosols as starting cores for droplets are needed. Due to the changes of releasing aerosols in air, cloud formation itself and their probability of appearance change because more condensation nuclei are available in the atmosphere. With the changes of cloud appearance the radiation to the Earth's surface is effected as well. While solar shortwave radiation is scattered into space, the thermal radiation, emitted by the Earth itself, is back-scattered to the ground again which leads to a temperature increase there.

A main challenge for climate modeling are aerosols because they can have a cooling as well as a warming effect for the surface depending on its albedo. The ocean has a quite low albedo. When clouds, which have a much higher albedo, cover the sea, the albedo rises and the back into space scattered solar radiation as well. On the other hand, when black carbon is deposited over ice or snow it absorbs more energy, the ice melts and the ground starts to warm up.

When the ice starts to melt more and more each year, more and more energy is deposited to Earth and the effect becomes stronger and stronger. Especially in the Arctic this is a major

problem and is measured in winter times with a temperature increase of $3K$ per decade (Maturilli and Kayser, 2017).

Continuously the whole Earth is monitored by ground and space born instruments detecting global changes on short terms. But due to extreme conditions the Arctic is really hard to cover, even with satellites. For space-born observations it is hard to determine between ice, snow and clouds because the contrast is very low. Flying on polar orbits costs much more energy, which reduces the life-time of them. Additionally, lots of instruments have problems with the high albedo of the snow (Curry et al., 1996) and ice or need direct solar radiation for measurements, like measuring the total ozone concentration in a vertical column. During polar night these instruments can not operate and one has to take ground-based data of only a few polar research stations in the Arctic. Therefore, it is even a bigger challenge to interpret the few available data correctly.

Every spring (March, April) the so-called Arctic Haze is observed in the Arctic (Quinn et al., 2007). It dramatically reduces the visibility whereas the aerosol concentration on the other hand rises significantly during that time compared to summer months. In the dark season the aerosol sinks are reduced due to a larger snow and ice cover. Thus, the boundary layer is thermodynamically stably stratified, which leads to a smaller vertical atmospheric mixing. Also the relative humidity is very low and aerosols are not washed out. Both effects increase the life time of the particles in the air. With in-situ measurements Shaw (1995) and Eckhardt et al. (2003) showed that mainly anthropogenic pollutants, like soot or CO, accumulate and are transported into the Arctic.

When the snow is already gone, mostly small particles are observed (Engvall et al., 2008; Tunved et al., 2013). But it is not completely clear where this size of particles comes from.

To understand more about the polar atmosphere, especially the origin of the Arctic Haze, aerosol properties, their annual cycle and longterm changes of the atmosphere, the aerosol optical depth (AOD) is measured by sun photometers (summer) and a star photometer (winter) from 2001 to 2017 with the main focus on the years 2009 to 2017 because Stock (2010) has already done an evaluation of the sun photometer data from 1995 to 2008. As these instruments do not have a height information and the calibration of water vapor channels has very high uncertainties, Lidar (Light Detection and Ranging) and Radiosondes were also used. Apart from that the origin and the path of air masses arriving in the Arctic are investigated using 5-days back-trajectories.

All used instruments are obtained from Ny-Ålesund, a small research village at Kongsfjord in north-west of Svalbard at 78.923°N , 11.928°E .

2. Theory on tropospheric aerosol

The troposphere is the lowermost atmospheric layer, has a height of several kilometers (equator: 0-17 km, pole: 0-7 km) and concentrates around 80% of the total atmospheric mass. Beside the main two constituents, nitrogen (78%) and oxygen (21%), lots of trace gases and wafting solid or liquid particles like sea salt, black carbon, organic materials, desert dust or soil, form the atmosphere. All of these non gaseous constituents of the atmosphere are called aerosols. A typical aerosol size distribution is shown in figure 2 with the classification of aerosols by Junge (1963) (table 1).

Declaration	Size
Ultra-fine particle	$< 0.01\mu m$
Aitken particle	$0.01 - 0.1\mu m$
Accumulation particle	$0.1 - 1\mu m$
Giant particle	$> 1\mu m$

Table 1: Size distribution of aerosols characterized by Junge (1963)

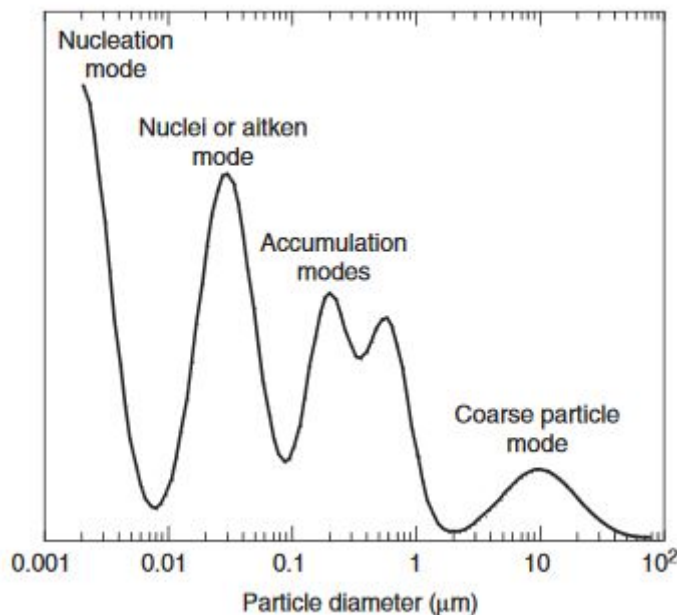


Figure 2: Particle size distribution for mid-latitude aerosol in arbitrary units of concentration (Buseck and Schwartz, 2003)

Depending on their origin, aerosols and their trajectories through the atmosphere have different and changing properties and chemical components because they are strongly affected by the surrounding atmosphere.

Most of the aerosols measured by in-situ measurements in Gruvebadet, Ny-Ålesund, are composed of the cations Na^+ , NH_4 and the anions SO_4^{2-} and Cl^- (Udisti et al., 2016).

The interaction with light strongly depends on particle radii as they have to reach a certain radius of about $0.1\mu m$ to become visible for photometers. Usually photometers detect the two modes with the largest aerosol particles whereas they are called in literature "fine" and "coarse" mode particles.

2.1. Sources and sinks

In general aerosols are classified in two categories depending on their primary origin, natural or anthropogenic. With the aid of vertical winds they are advected over thousands of kilometers. Hence, lots of different types of aerosols can get into the Arctic within a few days (Park et al., 2017)

Anthropogenic aerosols, which reach the Arctic, are usually emitted as sulfates or black carbon by combustion processes in the mid-latitudes. Due to chemical reactions these particles contain mainly sodium with diameters of $0.2 - 2\mu m$ (Udisti et al., 2016).

Another kind of aerosols have a natural origin and therefore a great number of origins and enter the atmosphere as sea salt, pollen or dust due to mechanical forces, such as sea spray, volcanic eruption or erosion. Beside marine biogenic produced dimethyl sulfide, aerosols with natural origin are larger than anthropogenic ones and are characterised as giant particles within the Arctic Haze season (Quinn et al., 2007; Park et al., 2017). In summer the aerosol is smaller than in spring time (Udisti et al., 2016).

The other possible manifestation for aerosols are secondary ones which can be created via homogeneous or heterogeneous nucleation. By phase transition from gaseous to solid or liquid state new particles are created. This process is called homogeneous. Such gases are made by anthropogenic emission of sulfur compounds in exhaust gases of fuel as well as naturally containing dimethylsulphid or methane. These gas molecules have to accumulate via collisions of more than two slowly moving particles by Brownian motion. The new formed larger particle saves most of the kinetic energy whereas two slower moving particles remain. In this case the kinetic energies of all involved particles are sufficiently small enough so that in the end gas molecules condensate and reach a critical radius to become stable. The probability for a collision of three particles is roughly proportional to the oversaturation of the molecules in the surrounding gas (Tunved et al., 2013). Because these new formed particles have only reached the critical radius they belong to the class of ultra-fine or Aitken particles. As time goes by molecules accumulate to the already existing ones and create larger particles.

When the particles are sufficiently large enough, the new formed particles are now called cloud condensation nuclei (CCN) and water condenses onto the surface because they support condensation at supersaturation values (relative humidity $> 100\%$) below the required size for homogeneous nucleation. For highly hygroscopic particles, like sodium chloride ($NaCl$) or ammonium sulfate ($(NH_4)_2SO_4$) this effect is much more relevant. The resulting saturation vapor pressure e_s significantly decreases below the one of pure water because e_s only depends on the absolute concentration of water molecules on the surface of the droplet. This leads to Raoult's law:

$$e(T) = e_s(T) \cdot \frac{n_w}{n_w + n_d} \quad (2.1)$$

Where e is the equilibrium vapour pressure over a solution with n_w molecules of water and n_d molecules of solute. e_s is the saturation vapour pressure with respect to a plane surface of water at the temperature of the system.

In theory it is also possible to create droplets only of pure water. But for this process a relative humidity of about 115% is required which is a very rare incident in nature. This accumulation has a big impact on the chemical and physical properties of the original particles because chemical reactions can take place in the liquid phase. This process is called heterogeneous nucleation.

The lifetime of aerosols strongly depends on their size and chemical composition. Ultra-fine and Aitken particles have a much stronger motion than larger ones due to Brownian motion or diffusion. Because they move randomly, the probability of collisions with each other is very likely. This leads to larger particles with simultaneously decreasing particle number density. The first very important sink is sedimentation or dry deposition. In this process aerosol finally hits obstacles, like buildings, trees or the ground, by Brownian motion and sticks to them. Oriented motion induced by gradients or gravitation forces particles to sediment. The sedimentation velocity strongly depends on their size and density and is proportional to the squared radius of the particle. The larger aerosols become the more inert they get and do not follow streamlines of air as precisely as lighter ones. Therefore, they stick to obstacles more easily. On the other hand accumulation mode particles with a diameter of around $0.2 \mu\text{m}$ (see table 2) are too large for Brownian motion but too light for self sedimentation by gravity. These kind of aerosols have the longest dwelling time. But the dwelling times are strongly affected by vertical wind motions.

aerosol diameter	ultra-fine $< 0.02 \mu\text{m}$	Aitken $0.02 - 0.2 \mu\text{m}$	accumulation $0.2 - 2 \mu\text{m}$	giant $> 2 \mu\text{m}$
lower troposphere	<1-24 h	6 d	8 d	1-7 d
upper troposphere	<1-24 h	12 d	8 d	2-10 d
stratosphere	<1-24 h	24 d	300 d	<100 d

Table 2: Dwelling time of different types of aerosols in the atmosphere, classified by Junge (1963)

In contrast to the dry sedimentation aerosols also can be washed and rained out when they form clouds. This is called wet deposition after the hygroscopic growth of the aerosol already has taken place. Accumulation particles are the main sources for water droplets and cloud formation in case they have a hydrophilic chemical composition. At the so-called deliquescence point the relative humidity is sufficiently high enough to create a water shell around the aerosol which now has a solid core. How fast a particle grows is determined by its chemical composition and the quotient of its moist and dry diameter depending on the relative humidity around that particle. The more hydrophilic the core is the faster it grows and the larger it becomes. This quotient plotted over relative humidity leads to the typical hysteresis for this particular aerosol (figure 3). In case the aerosol comes out of a wet atmospheric layer and moves into a dry one,

the surrounding water shell remains up to a relative humidity of about 70% for sulfates plotted in figure 3. Having a relative humidity smaller than this threshold the aerosol is not affected by water vapour. On the other side an aerosol particle coming out of a dry layer and being pushed into a wet one remains without liquid water shell up to a relative humidity of about 80%. This process is more important than the dry one because it directly affects the life-time of aerosols. Hence, the age of the air mass with the aerosol depends on the time of the last precipitation event.

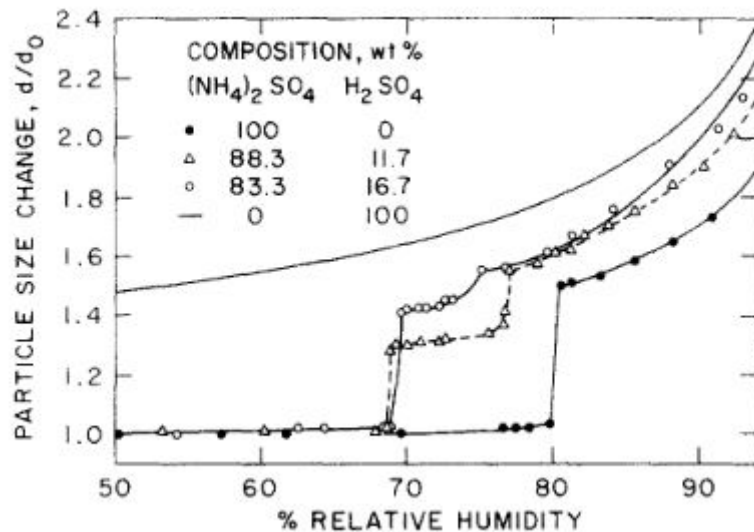


Figure 3: Hysteresis of the hygroscopic growth of sulfuric acid and ammonium sulphate at 25°C (Tang et al., 1978)

2.2. Interaction of aerosols and molecules with radiation

Direct solar radiation measured at the ground is strongly affected by particles in the whole atmosphere via scattering, reflection, absorption, re-emission and extinction. The efficiency of all these processes depends on the incoming wavelength. The most important possibilities of interaction between aerosols and radiation are absorption and scattering.

Whereas absorption converges radiation into heat depending on wavelength and atmospheric constituents, scattering changes direction and intensity of the radiation. Elastic scattering takes place if energy and momentum of the photons are conserved before and after the scattering event. If due to light-matter interaction the particle is excited into a higher state and falls down to the initial state or a slightly higher one, the event is called inelastic scattering and is described as Raman scattering.

For a given wavelength λ the scattering properties depend on size, shape and index of refraction. In general no analytic solution can be found because the scattering is too complicated. Only for special cases theories exist describing these scattering events. For spherical particles

Mie theory is used which is valid for arbitrary particle sizes. For small particles, compared to the wavelength of scattered light, Mie and Rayleigh theory become equal. As a consequence, scattering is described as Hertzian Dipole and classical electrodynamics.

Mie scattering

Mie scattering describes scattering of electromagnetic radiation on spherical particles. Only in case of spherical particles an analytical solution exists. In other cases the theory is analytically not closed.

This theory is valid for all sizes of spherical particles. Size parameter $x = \frac{2\pi r}{\lambda}$ and complex index of refraction determine the spatial properties of the refracted light field. The photon gets mainly scattered in forward direction (Mie, 1908).

Rayleigh scattering

Rayleigh scattering is one limit of Mie scattering for small particles. It describes the interaction between tiny particles with a diameter much smaller than the wavelength and electromagnetic radiation. Particles may be individual atoms or molecules and have to have only a real part of an index of refraction with a value of about 1, which is more or less given for clear sky conditions and responsible for the blue colour of the sky.

Rayleigh scattering is a process of electric polarizability of the particles. Incoming radiation is an electromagnetic wave. The oscillating electric field of the radiation acts on the charges within a particle and forces them to move at the same frequency of the light. Therefore, Maxwell's equations are simplified and the particle becomes a small radiating, Hertzian dipole which emits radiation. The scattering cross-section is proportional to λ^{-4} . This leads to a very strong wavelength dependent interaction between radiation and particles. The shorter the wavelengths are the larger the probability is the photon gets scattered at the particle.

Raman scattering

Raman scattering is the inelastic scattering of photons by molecules. When photons are scattered by atoms or molecules most of them are elastically Rayleigh scattered. So Raman scattering has also the λ^{-4} wavelength dependency. Only 1 out of 1000 photons is inelastically scattered by excitation. In the terrestrial atmosphere, most of the outgoing photons have a lower energy than the initial one. The easier an atom gets excited the higher the probability of such a scattering event becomes. This type of scattering becomes important for Lidar measurements.

2.3. Aerosol Optical Depth

The monochromatic extinction of the total vertical atmosphere α can always be written as the sum of the extinction coefficients of the Rayleigh scattering of air molecules α_{Ray} , the Mie scattering of aerosols α_{Aer} and absorptive contributions of some gases α_{Gas} like ozone, oxygen or water vapour:

$$\alpha = \alpha_{Ray} + \alpha_{Aer} + \alpha_{Gas} \quad (2.2)$$

With equation 2.2 the total optical depth τ_{ext} up to an height H as the integral over the total atmospheric optical depth τ is defined as follows:

$$\begin{aligned}\tau_{ext} &= \int_0^H a(z) dz \\ &= \int_0^H [a_{Ray}(z) + a_{Aer}(z) + a_{Gas}(z)] dz \\ &= \tau_{Ray} + \tau_{Aer} + \tau_{Gas}\end{aligned}\quad (2.3)$$

Using Lambert-Beer's law aerosol optical depth (AOD) can be measured and computed. Splitting the integral in three independent integrals is possible due to the assumption of only single scattering in the atmosphere. It is assumed that the intensity of direct solar radiation I_0 decreases from top of the atmosphere to the ground depending on physical properties of the penetrated medium. The integral over possible types of extinction in the atmosphere of equation 2.3 can be simplified to three independent integrals in general because only direct solar radiation is considered. In case one photon is extinguished by aerosol it can not be extinguished anymore by another particle. Equation 2.4 shows the modified intensity decay for a ground based measurement.

$$I = I_0 \cdot e^{-m \cdot \tau_{ext}} \quad (2.4)$$

Here I is the radiation at the ground and m the penetrated air mass. Atmospheric refraction is also considered in this ansatz. In general m is defined as the length of the path through the atmosphere the light had to travel to reach the ground. The exact solution calculated in Kasten and Young (1989) can be simplified for a solar zenith angle $\theta > 45^\circ$:

$$m = \frac{1}{\cos \theta} \quad (2.5)$$

The refraction index of the atmosphere increases continuously coming from outer space because the particle density increases exponentially in the same direction. Extraterrestrial radiation is refracted more and more the closer it gets to the ground because the refraction index n is proportional to the pressure p :

$$n = \frac{77.6}{T} \cdot \left(p + \frac{4810 \cdot e}{T} \right) \quad (2.6)$$

Where p is in milibars, T in Kelvin and e is expressed as the partial pressure of water vapor in millibars. This leads to a curved path through the atmosphere. The closer the sun reaches the horizon the stronger the refraction takes place (figure 4).

To get a more precise result relative air masses for aerosol, Rayleigh atmosphere and ozone have to be calculated separately.

Using the formula by (Kasten, 1965) to receive the relative aerosol air mass:

$$m_{Aer} = \frac{1}{\sin(h_{sun}) + 0.0548 \cdot (h_{sun} + 2.65)^{-1.452}} \quad (2.7)$$

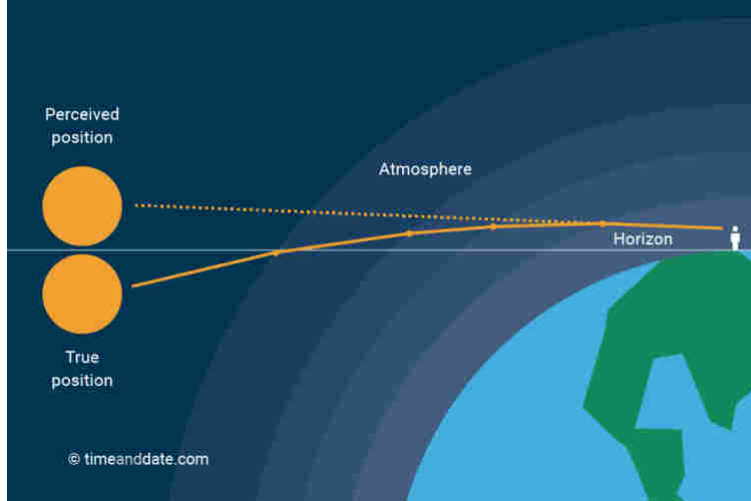


Figure 4: Changed apparent position of extraterrestrial objects due to atmospheric refraction (source: <https://www.timeanddate.com/astronomy/refraction.html>).

Where h_{sun} denotes the apparent solar elevation in degrees, which is always greater than the geometrical height of the sun due to a continuously changing refraction index of the atmosphere from top of atmosphere to the ground. To get h_{sun} temperature as well as pressure profiles have to be known.

The relative Rayleigh air mass is calculated using (Kasten and Young, 1989):

$$m_{Ray} = \frac{1}{\sin(h_{sun}) + 0.50572 \cdot (h_{sun} + 6.07995)^{-1.6364}} \quad (2.8)$$

The relative ozone air mass is calculated using WMO (2008):

$$m_{O_3} = \frac{r + H_{O_3}}{\sqrt{(r + H_{O_3})^2 - (r_E + H_s)^2 \cdot \cos^2(h_{sun})}} \quad (2.9)$$

Where $H_{O_3} = 22\text{km}$ is the height of the ozone layer, $H_s = 10\text{m}$ the station height and $r = 6370\text{km}$ the earth's radius.

2.4. Impact of aerosols on polar climate

There are two possible ways, directly and indirectly, how aerosols can act on the climate. Directly means that aerosols interact with the direct, short-wave solar radiation via scattering and absorption. In this case the aerosol can either have a warming or cooling effect to the atmosphere also depending on the surface albedo. Dark aerosol, like soot, forces a warming over a snow-covered surface because the total albedo of this system gets reduced (Shine and de F Forster, 1999). On the other hand strong scattering aerosol, like sulfur-containing particles, over dark surfaces, like forests, increase the total albedo and cause a cooling to the underlying atmospheric layers (Sand et al., 2017; Haywood and Boucher, 2000).

The indirect effect describes the impact of aerosols on radiation properties and the lifetime of clouds. Aerosols always start as cores on which water molecules condensate and form droplets or ice crystals depending on the temperature of the current layer. Twomey (1974) showed for the first time that cloud formation is directly proportional to the number of aerosols while having a constant liquid water content. Water droplets in polluted air have smaller sizes than ones formed under clearer atmospheric conditions. Additionally, the cloud albedo increases with smaller cloud particles because the smaller they are the more efficiently they reflect incoming direct solar radiation back to the upper atmosphere. Hence, the atmosphere becomes cooler. This effect is called Twomey effect. The cooling is also amplified by the absence of larger droplets which causes rain. So the cloud has a longer life-time (Sand et al., 2017; Albrecht, 1989) and also increases its vertical extend (Pincus and Baker, 1994).

There are several definitions of the Arctic. In general it is the area farther north than the polar circle (66.56°N). Whereas the climatological Arctic is the area on the northern hemisphere with a mean summer temperature less than 10°C and an area with a permanent frozen ground. Because the warm gulf stream is heading northwards, subtropical atlantic water is transported to higher latitudes. The boundary of the climatological Arctic is much more shifted to the North in the European continent compared to Siberia or Northern America. In the following the climatological definition is used to determine the Arctic which is shown in figure 5.

The Arctic climate is dominated by the annual changes of incoming solar radiation between polar day and night during summer and winter times, respectively. The large temperature gradient between equator and pole is the main contributor to the atmospheric circulation. In the beginning this meridional flow is forced by the rotation of the earth and consequentially by the Coriolis force on a more zonal flow. During winter times the polar atmosphere is in stagnation. Based on the high albedo of the snow cover the surface layer constantly cools and the atmosphere is stable stratified because turbulent mixing of atmospheric layers is inhibited (Shaw, 1995). The temperature gradient is maximal between equator and polar regions and thus leads to a stronger meridional flow than in summer. When the polar night in spring ends the global temperature gradient decreases and more warmer air can reach the Arctic. With these changes of winds aerosols produced in the South can be advected into the Arctic more easily and form the Arctic Haze in the beginning of spring (Quinn et al., 2007). On the other hand the wet aerosol deposition is reduced during polar night because precipitating clouds are less frequent than in other seasons (Shaw, 1995).

Due to the already in the introduction mentioned Arctic Amplification the polar atmosphere is very sensitive to even small changes in the temperature. Additionally, the surface albedo in the Arctic is very high over snow and ice covered areas. Contrary to mid-latitudes and the tropics aerosols have a warming contribution to the large-scale energy budget because they reduce the initially high albedo. For this reason it is very important to look at aerosol properties and long term trends in polar regions.



Figure 5: Climatological Arctic is located within the red line (source: https://legacy.lib.utexas.edu/maps/islands_oceans_poles/arctic_region_pol_2007.pdf)

3. Data Processing and Methods

3.1. Instruments

In general, there are two ways of observing aerosols: in-situ and remote sensing instruments. For in-situ measurements an aircraft or balloon is needed to fly directly into the atmospheric layer containing the aerosol. With this method micro-physical and chemical properties, like size, shape, composition or index of refraction, can be determined directly and very precisely for example by using filters or particle sizers. But the atmospheric cover is very small. Using remote sensing instruments, like satellites or ground based instruments, nearly the whole Earth is covered. But, compared to in-situ measurements, with a lower accuracy.

Additionally there are two different types of optical remote sensing instruments - active and passive ones. Active instruments emit electromagnetic radiation and receive the signal backscattered by aerosols or clouds in the atmosphere. Lidar is an example of this category. On the other hand passive instruments measure light transmitted through the whole atmosphere. Sun, stars or the moon are sources for these types of instruments. Photometers or radiometers are examples of this category.

To describe the atmospheric radiation balance it is necessary to measure aerosol properties which change the incoming solar radiation. One of the most important properties is aerosol optical depth (AOD). There are several possibilities for measuring it like Lidar, sun and star photometers. Because every instrument measures different aerosol properties at different times and to reduce typical errors of each instrument, the results should be combined for a better understanding of the Arctic Haze. To fill the measuring gaps in the polar night a star photometer is used with a small overlap in March and October with the sun photometer.

3.1.1. Raman Lidar "KARL"

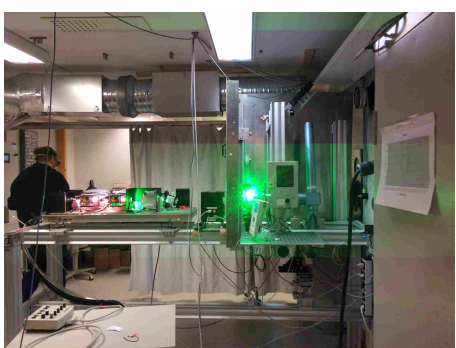


Figure 6: Lidar "Karl" while main-tanance work (Photo: Sandra Graßl)

The multi-wavelengths Raman Lidar KARL ("Koldewey Aerosol Raman Lidar") consists of a Nd:YAG laser with 10W in each of the wavelengths $\lambda = 355nm$, $532nm$ and $1064nm$. Additionally, in the first two wavelengths the polarisation in parallel and perpendicular to the emitted laser beam is recorded.

In the homosphere the fraction of nitrogen, N_2 , is constant at 78%. In this part of the atmosphere the Raman shifted lines of N_2 are also detected at $387nm$ and $607nm$ and water vapour at $407nm$ and $660nm$. The mirror has a diameter of 70cm. The overlap is complete after about 700m altitude, whereas below a qualitative estimation of the backscatter coefficient using a Vaisala CL51 ceilometer is performed. More technical details on the system are given in Hoffmann (2011). The eval-

ation is typically done with $30m$ vertical and $10min$ temporal resolution. No further smoothing of the Lidar profiles has been performed as this can easily lead to wrong results as the derivation of extinction coefficients from Lidar is an ill-posed problem.

3.1.2. Sun Photometer



Figure 7: Sun photometer during a calibration expedition in Izaña, Tenerife (Photo: Sandra Graßl).

Aerosol optical depth (AOD) is measured by a sun photometer, type SP1a by Dr. Schulz & Partner GmbH (<http://www.drschulz.com/cnt/>) in 17 wavelengths between $\lambda = 369nm$ to $1023nm$ with a field of view of $1^\circ \times 1^\circ$ and a time resolution of 1 minute. The wavelengths $\lambda = 381.5, 722.2, 946.2, 962.4, 1045.3$ and $1089.4nm$ are omitted in this thesis because measured AOD has always been too high. In winter 2012/13 a new sun photometer was installed and just 10 of 17 wavelengths remained in the same wavelength range. Only the wavelength $\lambda = 944.8nm$, which is devoted to water vapour, is omitted in this thesis for the newer photometer. To calibrate the filters for water vapour additional measurements of this highly variable atmospheric constituent are required. With the remaining 9 wavelengths optical parameters like the AOD are computed. The instrument is calibrated regularly in pristine conditions at Izaña, Tenerife, via Langley method. A cloud screening based on short scale fluctuations of the AOD is used as in Alexandrov et al. (2004). The uncertainty for the AOD is generally said to be around 0.01 (Stock, 2010; Toledano et al., 2012). However, this is the maximum error of the instrument because the fluctuations are much smaller by comparing data minute by minute under low or constant aerosol conditions. Therefore, we conclude that even 1 minute data has a sufficient quality and we are going to present some results accordingly.

The number of individual measurements differs between a few hundreds, especially in March and September, to up to 12,000 in early summer. No trend in each month can be seen comparing the amount of cloud-free measurements over the years. Only an annual cycle due to polar day and night is included in the data. To compare different types or properties of Arctic aerosols the months April, May and August were chosen as typical months for periods with, without haze and late summer, respectively. The months March and September are not chosen because the number of available measurement points is limited due to the beginning and end of polar night.

An automatic tracking system was installed to the sun photometer in 2004. Since then the number of measurements has been increasing significantly because the photometer runs flawlessly. Before that upgrade measurements were taken only during campaign activity. Due to

the instrument data is only available in clear sky conditions. In this regard the data should represent the real aerosol conditions. Only aerosols that are advected and processed within clouds or hygroscopic growth cannot be measured by this instrument.

As in this study we are interested in typical aerosol properties we have omitted few singular extreme events from the data with $AOD_{500} > 0.3$ that originates from known and exceptional strong events. Both, the agricultural flaming of May 2006 (Stohl et al., 2007) and the forest fire of July 2015 Markowicz et al. (2016) yielded AOD_{500} values around 1 which would significantly bias monthly averages. If $AOD_{500} > 0.3$ was detected after cloud screening the whole day was omitted. In total seven days during the period from 2009 to 2017 were deleted from the data.

3.1.3. Star Photometer



Figure 8: The star photometer located on the roof of the observatory in Ny-Ålesund (Photo: http://awikipev.awi-koldewey.no/doku.php?id=en:systems:photometer:star_photometer).

The measuring principle of a star photometer is the same as for the sun. It faces the star while rotating the different filters at $\lambda = 420.0, 450.3, 469.4, 500.4, 532.1, 550.3, 605.4, 639.8, 675.7, 750.9, 778.6, 862.5, 933.2, 943.0, 952.7, 1025.9$ and 1040.6nm . With an additional background measurement the influence of stray light is reduced.

There are two different possibilities to determine the AOD using a star photometer. One star measurement requires a calibration at very clear nights, just like Langley calibration for sun photometers. For the two star measurement a calibration is not needed in advance. But on the other hand the second method is much more effective by atmospheric inhomogeneities and horizontally stratified layers.

The calculations of the AOD are performed very similarly to the sun photometer, only the apparent magnitude of different stars has to be taken into account.

To minimise measuring errors bright and, as a local advantage, circumpolar stars are chosen for photometry. The three stars $\gamma\text{ Gem}$, $\beta\text{ UMa}$ and $\alpha\text{ Lyr}$ are used for both types of measurement. The star $\alpha\text{ Aql}$ has only been used for two star measurement yet. Their physical properties are shown in table 3.

star	apparent magnitude	right ascension	declination
γ Gem (Alhena)	1.93	07 ^h 34 ^m 37.584 ^s	+31° 53' 17.8160"
β UMa (Merak)	2.37	11 ^h 01 ^m 50.476 ^s	+56° 22' 56.7339"
α Lyr (Vega)	0.04	18 ^h 36 ^m 56.336 ^s	+38° 47' 01.2802"
α Aql (Altair)	0.77	19 ^h 50 ^m 46.999 ^s	+08° 52' 05.9563"

Table 3: Position and apparent magnitude of all used stars for star photometry in Ny-Ålesund.

One Star Measurement

For one star measurements a Langley calibration, which is also commonly used for sun photometers, has to be done in advance (see section 3.1.2).

Measurements for calibration taken by the star photometer in Ny-Ålesund are more scattered than measurements by the sun photometer. Thus, the error to the AOD is larger.

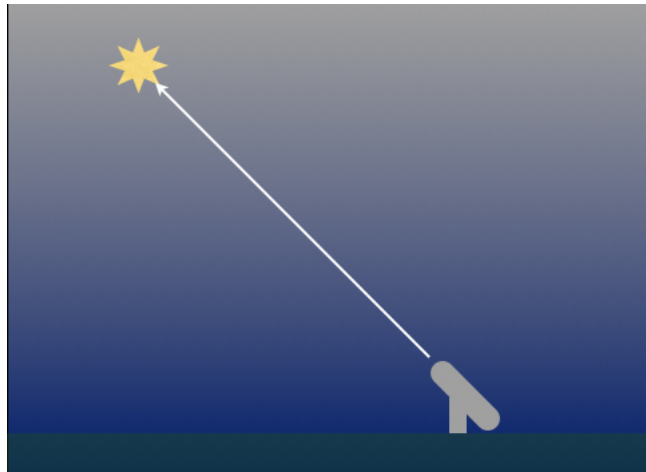


Figure 9: Measuring principle of a one star measurement

Due to the low apparent magnitude M of stars compared to the sun a photon counter is used for measurements. The electronic count number $CN = SC - HC$ with SC is the total number of detected counts and HC the number of counts coming from the background, depends on the magnitude M :

$$M = -2.5 \cdot \log_{10}(CN) \quad (3.1)$$

Using one star measurements and knowing the air mass m and as well the measured apparent stellar magnitude M as the extraterrestrial M_0 , the total atmospheric optical extinction α can be computed for each wavelength:

$$\begin{aligned} \alpha_\lambda &= \frac{M_\lambda - M_{0,\lambda}}{m_\lambda} \\ &= \alpha_{Aer} + \alpha_{Ray} + \alpha_{O_3} \end{aligned} \quad (3.2)$$

Two Star Measurement

A two star measurement consists of three standard measuring steps and requires as well a pair of stars with a high and a low star as a horizontal stratified, homogeneous atmosphere. Both stars should be as bright as possible and the following conditions towards each other:

1. Difference of the elevation angles as big as possible
2. Difference of the azimuthal angles as small as possible

Condition 1 arises from the calculation of the astronomical extinction coefficient. Only with the difference in the elevation of both stars the air mass can be calculated. Condition 2 should secure that the light of the two stars reaches the telescope under atmospheric conditions as equal as possible. For the calculation of the optical thickness of the aerosol the astronomical extraterrestrial magnitudes of both stars are needed. The steps of a two star measurement are:

1. Standard measuring of the low star (*low*₁)
2. Standard measuring of the high star (*high*)
3. Standard measuring of the low star (*low*₂)

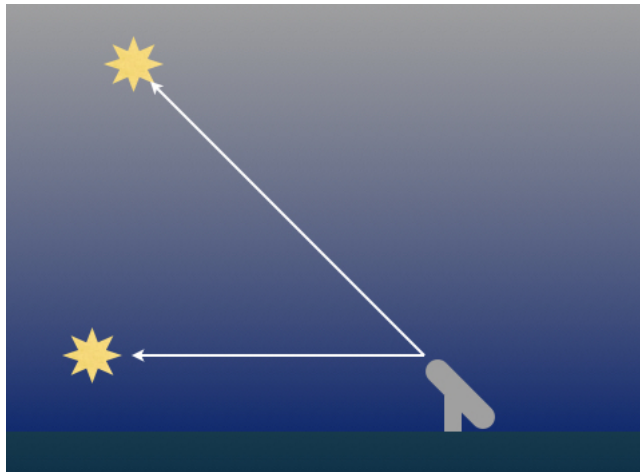


Figure 10: Measuring principle of a two star measurement

The results are two values for the aerosol optical thicknesses per wavelength for each standard measuring pair of *low*₁ to *high* and the standard measuring pair *high* to *low*₂. Out of the high-graded two star measurings the spectral extraterrestrial magnitudes $\alpha_{\lambda}^{1,2}$ for the one star measuring are calculated which are used as calibration values for the one star measurement:

$$\begin{aligned}
 a_{\lambda}^{1,2} &= \frac{(M_{\lambda}^1 - M_{0,\lambda}^1) - (M_{\lambda}^2 - M_{0,\lambda}^2)}{m_{\lambda}^1 - m_{\lambda}^2} \\
 &= a_{Aer} + a_{Ray} + a_{O_3}
 \end{aligned} \tag{3.3}$$

With the total atmospheric extinction the AOD can be determined:

$$\begin{aligned}\tau_{1,2} &= a_{1,2} \cdot \frac{\ln(10)}{2.5} \\ &= \tau_{Aer} + \tau_{Ray} + \tau_{O_3}\end{aligned}\quad (3.4)$$

Cloud screening

Cloud screening is a crucial and difficult step in the preparation of data. An algorithm which is too strict removes all the data even if there are no clouds but a thick layer of aerosols. On the other hand a too soft algorithm does not remove all of the data with thin clouds and so conclusions of atmospheric properties get wrong.

The already existing algorithm for the sun photometer can not be applied to photometers during night times. Due to the large difference of stellar and solar irradiance the star photometer needs about *6min* for one measurement whereas for the sun photometer only *1min* is sufficient.

In total only six star photometers are installed worldwide these days. Pérez-Ramírez et al. (2012) has already suggested a cloud screening algorithm in three steps for the star photometer in Granada, Spain:

- 1 Eliminate all measurement points with values lower than their uncertainties and with air masses acquired with $m < 3$.
- 2 Filtering of consecutive data points with $\Delta AOD(\lambda) > 0.03$. Then moving averages for every AOD, $\tau_{aer}(\lambda)$, is computed for time periods of 1 hour and the whole measurement period. Data points are neglected when the difference between the data point itself and the average value is larger than 3 standard deviations.
- 3 Eliminate all data of this night if more than two-third are removed. Otherwise average remaining data over a time period of *30min*.

During winter times the atmosphere is very stable without convection and the influence of the sun. Compared to aerosol arriving in Granada the background aerosol load in the polar air is much less and is less homogeneous which leads to a larger variability in the cases clouds arrive. Hence, the variability between two adjacent measurement points is small so that the steps 2 and 3 remove most of the data.

Therefore, a new idea has to be implemented using the measurements and the parameter α of equation 3.12 (chapter 3.2) directly.

These thresholds are chosen by inspection of several measurement months of the star photometer and by observations of Tomasi et al. (2007) who found characteristic values for different types of polar aerosols (table 5).

The clouds which are detected in the algorithm are still thin enough for the stellar light to pass through.

Type of measurement	Properties
Cloud	$\alpha > -0.5$ and $AOD_{500} > 0.07$
Pre-condensation	$\alpha > 0$ and $AOD_{500} > 0.07$
Mixed phase	$\alpha > -1.4$ and $\alpha > -0.5$
Aerosol	$\alpha < -1.4$ and $AOD_{500} < 0.1$

Table 4: Parameters of the cloud screening algorithm.

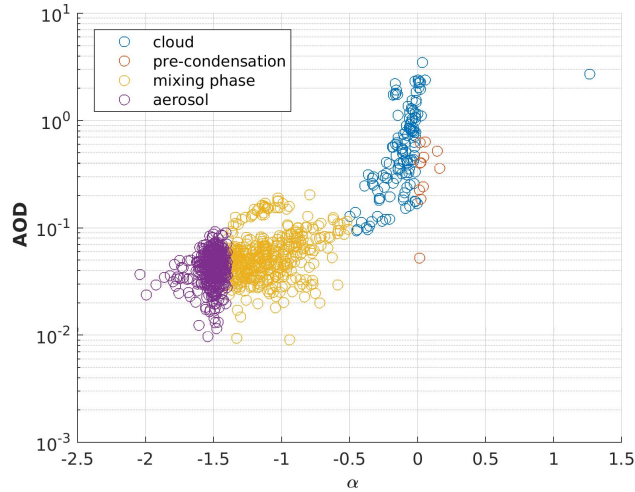


Figure 11: Example of all measured data in November 2017. The different colours correspond to the thresholds listed in table 4

Before cloud formation takes place, the aerosol accumulates water vapour on its surface and rapidly changes its size, shape, refractive index and extinction efficiency. This effect only reduces the visibility and increases the total optical depth. No cloud droplets are formed within this step but the photometer is not able to measure the AOD properly.

Manual cloud screening is very time consuming and also subjective, so an automatic script is needed. With this algorithm only data from Ny-Ålesund was analysed. To improve it, the Deutscher Wetterdienst (DWD) located in Lindenberg, Germany, is going to analyse and compare this algorithm with their own data. Even for them the cloud screening algorithm described in Pérez-Ramírez et al. (2012) is also too strict. A final evaluation will be done in future time.

In November 2017 the weather conditions were good enough to receive lots of data. The new cloud screening algorithm with the above mentioned thresholds are shown in figure 11. To improve the thresholds of the four different categories this algorithm will have to be validated in future time.

Ozone correction

A huge problem during winter times is the missing of daily ozone measurements because sun light is needed for satellite based observations of a total ozone column. Only once a week an ozone balloon is launched in Ny-Ålesund.

Due to rapid changes of weather conditions the polar vortex rapidly changes its position and shape. Hence, the observing station Ny-Ålesund can be located within or outside the vortex and the vertical column of ozone can change from 178 DU (26.3.2011) to 785 DU (25.2.2009) in Ny-Ålesund.

The optical thickness of ozone is calculated with:

$$\tau_{o_3} = \frac{K_{o_3}(\lambda)}{1000} \cdot O_3(DU) \quad (3.5)$$

Where $K_{o_3}(\lambda)$ being a wavelength dependent spectroscopic value based on the continuous Chappuis band between 400 and 650nm with the maximum at 603nm and $O_3(DU)$ being the total amount of ozone of the atmosphere in Dobson Units. The filter with the largest dependency of ozone of the star photometer has a wavelength of 605.4nm, wherefore $K_{o_3}(\lambda) = 0.1210$. For this particular filter of the star photometer the maximum error of a wrong ozone column concentration is $\Delta\tau = 0.0734$ and, therefore, not neglectable.

Influence of PSCs on AOD

When the polar stratosphere becomes cold enough ($< 195K$), water, nitric and sulphuric acid or even solid ice form spherical droplets and clouds in the stratosphere between 15-25 km height. They are called Polar Stratospheric Clouds (PSC). Over Ny-Ålesund they usually appear between December and March (Maturilli et al., 2005).

On the 23.12.2016 a PSC was observed via Lidar data with a thickness of about 0.5km over Ny-Ålesund while the star photometer was measuring simultaneously (figure 12). This day was chosen because the PSC was thickest at this day and is easily recognised in the Lidar profile.

The cloud screening algorithm detects clouds between 10 and 10:30 am and the measured AOD is flagged afterwards as "mixing phase". Due to tropospheric conditions the star photometer data was categorised into the above mentioned groups.

Knowing the thickness of the PSC ($\Delta z = 500m$), estimating the Lidar ratio ($LR = 36$) and in conjunction with the backscatter ($b^{aer} = 2 \cdot 10^{-7} m^{-1} sr^{-1}$) the maximum optical depth for $\lambda = 532nm$ of the cloud can be guessed using the equation for the definition of the Lidar Ratio:

$$LR = \frac{a^{aer}}{b^{aer}} \Rightarrow a^{aer} = LR \cdot b^{aer}$$

Taking this result and using equation 2.3:

$$\tau^{PSC} = \int_{z_1}^{z_2} a^{aer}(z) dz \simeq \Delta z \cdot LR \cdot b^{aer} = 3.6 \cdot 10^{-3}$$

While having an AOD variability between two adjacent measurements of up to 0.004, the influence of the PSC is negligibly small. Due to the small contribution of PSC to the total optical thickness this ansatz does not answer the question of a high mean AOD of this month.

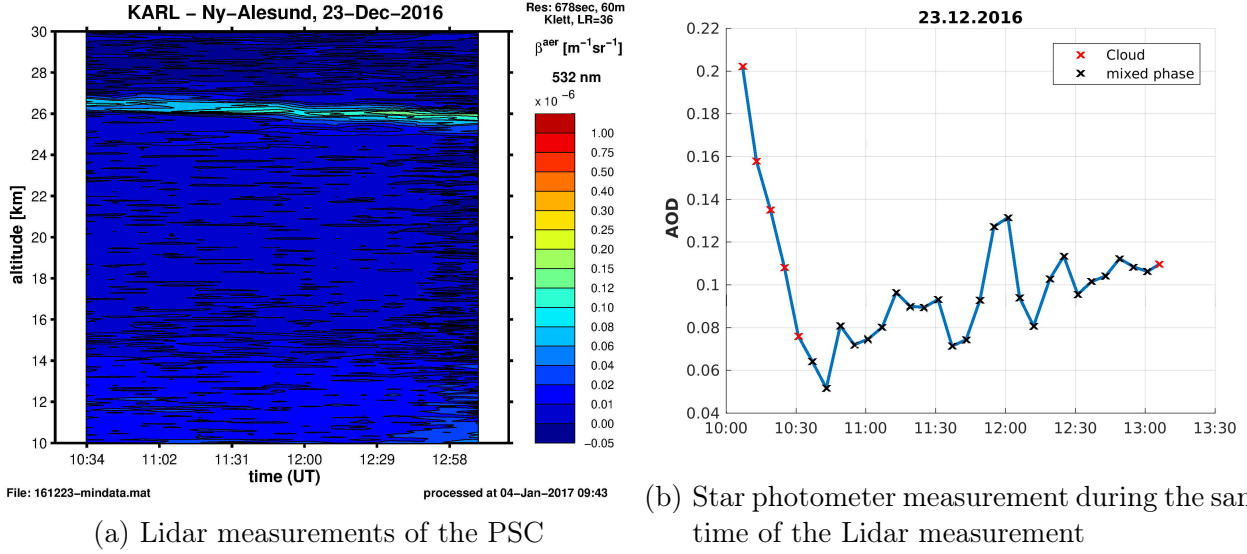


Figure 12: comparison of measured AOD during the presence of a PSC, observed by Lidar.

3.2. Data fitting and processing

The easiest way of fitting can be done with the later mentioned ansatz by Ångström. Nevertheless, modified ways were implemented and tested to gain a bit more information and more accurate fitting results from given data.

All the used sun photometer data was evaluated with programs programmed by Maria Stock and Holger Deckelmann (Stock, 2010) in advance using World Meteorological Organization (WMO) standards (Hegner et al., 1998). So a correction of ozone was done using daily ozone column concentrations measured by the Total Ozone Mapping Spectrometer on a satellite operated by NASA. In the last step clouds were removed manually.

Ångström ansatz

The most obvious way to fit measured data by a photometer to a physical law is done considering Ångström theory in which extinction A and optical thickness τ is related to a reference value of a theoretical measurement at a wavelength of $\lambda_0 = 1\mu\text{m}$ with the ansatz by Ångström (1929, 1961, 1964):

$$\begin{aligned} \tau_{\lambda_0} \cdot \lambda_0^{-A_{\lambda_0}} &= \tau_{\lambda} \cdot \lambda^{-A} \\ f(\lambda) &= C \cdot \lambda^{-A} \end{aligned} \quad (3.6)$$

Where $a = -\frac{\ln(\tau(\lambda_1)/\tau(\lambda_2))}{\ln(\lambda_1/\lambda_2)}$ and $C = -\frac{\tau_{\lambda_0}}{\lambda_0^{-A}}$ is the so-called turbidity parameter and it is connected to the refractive index, the total number of aerosol particles and its size distribution. For $A \rightarrow -0$ particles have at least the same size or are larger than the scattered light and so they are larger than $1\mu\text{m}$ (Stock, 2010) and the regime of geometrical optic can be

used. In this limes there is no wavelength dependency of scattering and both interference and refraction can be neglected. But geometrical shadows, transmission and macroscopic reflection become important. In the limes of $A \rightarrow -4$ the particles appear like point masses and they are much smaller than the scattered solar radiation. This is also called the "Rayleigh regime". In a longterm study of Arctic aerosol properties at 500nm Tomasi et al. (2007) found the Ångström exponent for Arctic background aerosol of $A = -1.4$ (table 5).

Aerosol Extinction Model	AOD_{500}	Ångström exponent A	Mode Diameter [μm]
background Arctic aerosol	0.015	-1.40	0.01
Arctic dense aerosol	0.080	-1.00	0.01 and 0.60
Arctic Haze	0.150	-1.25	0.01 and 0.60
boreal smoke	0.300	-1.20	0.01 and 0.60

Table 5: Median values of Ångström Exponent A , AOD_{500} and mode diameter modeled by Tomasi et al. (2007).

This ansatz is commonly used in atmospheric science. But in the following different ways of AOD calculation are tested to increase the fitting accuracy and the gain of information about physical properties of aerosols.

Coarse and fine mode

Trying to gain additional information about aerosol properties an assumption concerning coarse and fine particle modes were done and described in O'Neill et al. (2001a), O'Neill et al. (2001b), O'Neill et al. (2003).

Optical properties of aerosols in the ultraviolet to the near-infrared spectrum are largely influenced by a fine and coarse mode (further described in section 2.1). The most important radius size is in sub-micron range.

The ansatz for coarse and fine mode is done using equation (O'Neill et al., 2001a):

$$\begin{aligned} \tau_{aer} &= \tau_f + \tau_c \\ &= A_f C_f + A_c C_c \end{aligned} \quad (3.7)$$

where A_f and A_c are the vertically integrated number density in abundance and $C_f(\lambda)$ and $C_c(\lambda)$ are the extinction cross sections of the fine and coarse mode, respectively. The indexes f and c correlate to fine and coarse mode and the Ångström exponent A is defined as:

$$A = -\frac{d \log \tau_{aer}}{d \log \lambda}$$

with the second derivative:

$$A' = -\frac{d^2 \log \tau_{aer}}{d \log \lambda^2}$$

The total optical curvature parameters τ_{aer} , A and A' characterise most of the variability in the aerosol optical depth spectra and they are related to the coarse and fine mode components of the bimodal aerosol particle size distribution (O'Neill et al., 2001a). In O'Neill et al. (2003) all three parameters are referred to the measured spectrum to the reference values of $\lambda = 500\text{nm}$ in a second-order polynomial fit of $\ln(\tau_{aer})$ versus $\ln(\lambda)$.

This first method assumes a more flexible but necessarily more cumbersome optical description in terms of independent discrete bins of a generalized aerosol size distribution.

The second method, and the more stable one, is a description of most optical phenomena by an appropriate choice of two or at most three size distribution modes. The second choice is more robust and repeatable than the multi-bin particle size distribution inversions of optical data and may serve the needs of many users of aerosol optical data (O'Neill et al., 2001a). The bimodal approach also permits simple and pure optical techniques to get coefficients for each separate particle size mode from the general spectral behaviour of the aerosol optical depth. These coefficients can be used to extract microphysical parameters at an usually sufficient level, like effective or mean modal radius being derived from the Ångström coefficient associated with that mode.

Nevertheless, for the observations in the Arctic this algorithm was not used due to several reasons. First of all, O'Neill et al. (2001b) used a mono-cromatic ansatz to obtain a fitting ansatz for the polycromatic measurements. He argues that aerosol properties do not change from ultraviolet to near-infrared part of the electromagnetic spectrum (O'Neill et al., 2003). Additionally, O'Neill et al. (2001a) also used algorithms for calculating Mie scattering to get an estimation for particle sizes (O'Neill et al., 2003).

In other polar regions, especially in North America, natural, like geophysical or biological, or anthropogenic processes create aerosol. This means a large distribution of particle radii. Because of nearly no aerosol sources in Spitsbergen the arriving aerosols are very old and small. Large particles are more affected by sedimentation or are washed out of the atmosphere by rain. So it is necessary in Ny-Ålesund to look at changes in AOD due to scattering of small and narrow distributed particles. Hence, the hypothesis is tested in the following whether A' is independent of λ .

Long and short wavelength dependent Ångström ansatz

To prove whether a separation in wavelength is justified the original Ångström ansatz is taken but both parameters a_1 and a_2 are computed independently for two wavelength intervals ($349,7\text{nm} \leq \lambda_1 \leq 700\text{nm}$ and $700\text{nm} \leq \lambda_2 \leq 1070,5\text{nm}$). The intervals are chosen to obtain one for the visible range (VIS) of the electromagnetic spectrum and the other for the near-infrared (IR) part:

$$\tau(\lambda) = \begin{cases} a_1 \cdot \lambda^{a_2}, & \forall \lambda < 700\text{nm} \\ a_3 \cdot \lambda^{a_4}, & \forall \lambda > 700\text{nm} \end{cases} \quad (3.8)$$

The four fitting parameters are calculated as in the traditional Ångström ansatz but inde-

pendently for every λ and for several days in 2013. For computating the fitting parameters the wavelength 675.9nm was included in both regimes. In case there is no difference between Ångström ansatz and the modified one, in other words no wavelength dependency of the Ångström exponent is visible, a continuous fitting curve is expected.

However, the assumption of a power-law for the AOD is only a common approximation. A typical result for arctic aerosol (green circles) can be depicted in figure 13. For simplicity the exponential fit (colored lines) is done using formula 1. It can easily be seen that this approximation under- and overestimates the measured AOD by the instrument (figure 13). To achieve a better result for the same data set the wavelength range was divided into two regimes, for the visible ($< 700\text{nm}$) and infrared ($> 700\text{nm}$) spectrum. Now two independent Ångström exponents are computed, one for every regime. The fitting curve with the chosen ansatz 3.8 approaches in a better way. In every case there was a step in the fitting functions of both regimes and the fitting accuracy has always been improved with this ansatz. Therefore, the fitting function 3.8 does not provide a good approximation of the aerosol properties and needs to be improved, why a wavelength independent ansatz has to be improved by an extension by a wavelength dependency.

The fitting accuracy is defined as the square differences χ^2 between the observed and fitted AOD. In this thesis it is defined as:

$$\chi^2 = \frac{1}{m} \cdot \sum_{k=1}^n \left(\frac{AOD_{meas}(\lambda_k) - AOD_{fit}(\lambda_k)}{\Delta AOD(\lambda_k)} \right)^2 \quad (3.9)$$

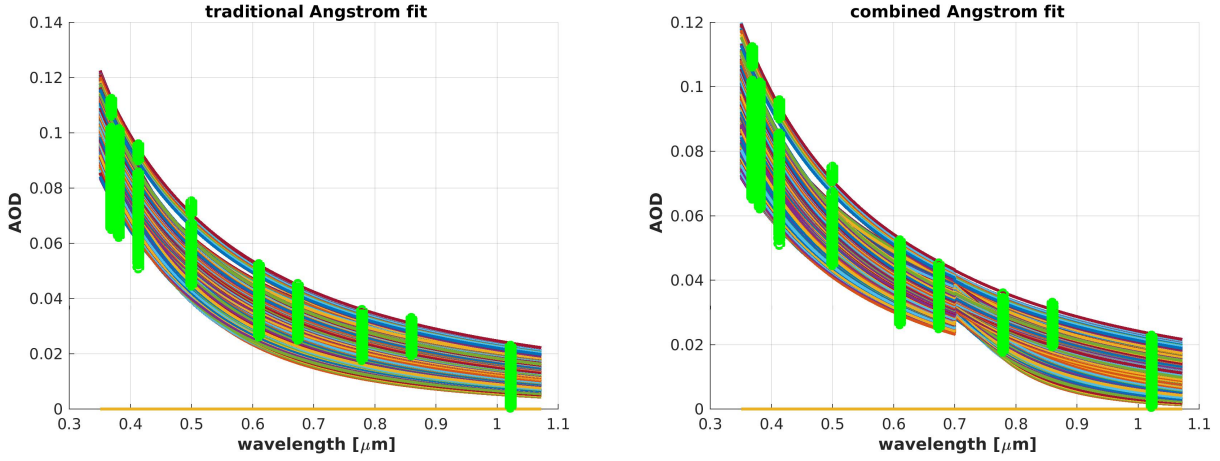
Where m is associated with the degrees of freedom, $n = 9$ the number of used wavelengths, the suffixes "meas" and "fit" refer to the measured and fitted AOD, respectively. The error of the AOD is marked as ΔAOD .

Differences in the fitting of the same data set with only two different wavelength intervals can be easily seen. Whereas the traditional ansatz (equation 3.6) can not reproduce a fit through the measured data in some cases, the new chosen ansatz of equation 3.9 can do so.

As it can be seen in the previous discussed generic days during spring and summer 2013 there is a change of fitting accuracy considering only long and short wavelengths, like in equation 3.8, compared to the general used Ångström ansatz in equation 3.6. This is an indicator that the suggested ansatz by Ångström (equation 3.6) has a wavelength dependent exponent.

Two component ansatz by Levenberg-Marquardt algorithm

Since an improvement was achieved by using equation 3.8 instead of equation 3.6, the Ångström law will be improved. This observation can be explained that the Arctic aerosol follows a bi-modal size distribution. Compared with other places worldwide the total aerosol load is much less but on the other hand there are sub-visible cirrus or ice crystals, which are very large.



(a) Data (green) with fitting curves (coloured) by Ångström law
 (b) Data (green) with fitting curves (coloured) by two independent Ångström laws

Figure 13: Green circles represent individual measurements and the coloured lines the fitted exponential law. The data was fitted (a) in the full range of the photometer and (b) only in the visible ($< 700\text{nm}$) and in the near infrared ($> 700\text{nm}$) for the same data set.

To achieve a better fitting accuracy than by the traditional Ångström ansatz an approach was chosen using two components and the Levenberg-Marquardt algorithm for computation. It is a non-linear approach to find solutions for the non-linear fitting functions f in the neighbourhood of an initially estimated parameter, in this particular case a_1, a_2, a_3 and a_4 , in which f is a functional relation mapping a parameter vector to an estimated measurement vector. Photometers only measure the integrated spectral AOD. In general it is possible that there are two independent layers of aerosols or aerosol and clouds lying over each other, which do not interact. For this case an equal looking summand is added to Ångström ansatz to gain independent information about both layers:

$$f_{LM}(\lambda) = a_1 \cdot \lambda^{a_2} + a_3 \cdot \lambda^{a_4} \quad (3.10)$$

Considering the backscatter ratio measured by a Lidar it can easily determined whether aerosols or clouds are observed at this day.

For photometers cloud layers have to be sufficiently thin so that the direct solar radiation can penetrate the clouds directly. Otherwise the measured optical thickness is too large and the corresponding data point has to be removed out of the data set (Kautzleben, 2017).

To determine the convergence of the ansatz, the code has to come to the same result as the one with artificial noiseless data. Afterwards the noise increases linearly following the equation:

$$f_{test}(\lambda) = f_{artificial}(\lambda) + n \cdot \tau_{noise}(\lambda) \quad (3.11)$$

Where $f_{artificial}(\lambda)$ is the AOD computed by Levenberg-Marquardt algorithm being in the interval $[0.0156 : 0.0859]$ for $\lambda = 1019.0\text{nm}$ and $\lambda = 368.1\text{nm}$, respectively. $r(\lambda)$ is a random

3. Data Processing and Methods

number individually set for each wavelength in the interval $[-0.0956 : 0.2304]$ and n the factor tuning the signal-to-noise ratio. With this artificial AOD the algorithm has to converge to the four fitting parameters a_1 , a_2 , a_3 and a_4 of $\tau_{\text{artificial}}(\lambda)$ depending on the noise level n . Table 6 shows whether the code still can achieve an acceptable result depending on the strength of the added noise:

n	1	10^{-1}	10^{-2}	10^{-3}	10^{-4}
convergence	no	no	no	yes	yes

Table 6: convergence of the Levenberg-Marquardt algorithm with linear weighted noise added to AOD

Besides, Levenberg-Marquardt algorithm for equation 3.10 has a better fitting accuracy than Newton method, even noise in the order of 10^{-3} relative to the measured AOD disturbs the calculation and the code does not converge anymore. The two-component ansatz in theory is better but the convergence is only ensured when $\frac{\Delta\tau}{\tau} = \mathcal{O}(10^{-3})$.

On a very clear day, like 18th April 2013, between 8 and 10 am all 120 measurements were taken to estimate the maximal error of the AOD at the reference wavelength of 500nm. Considering a perfect sun photometer all the noise is produced by the atmosphere.

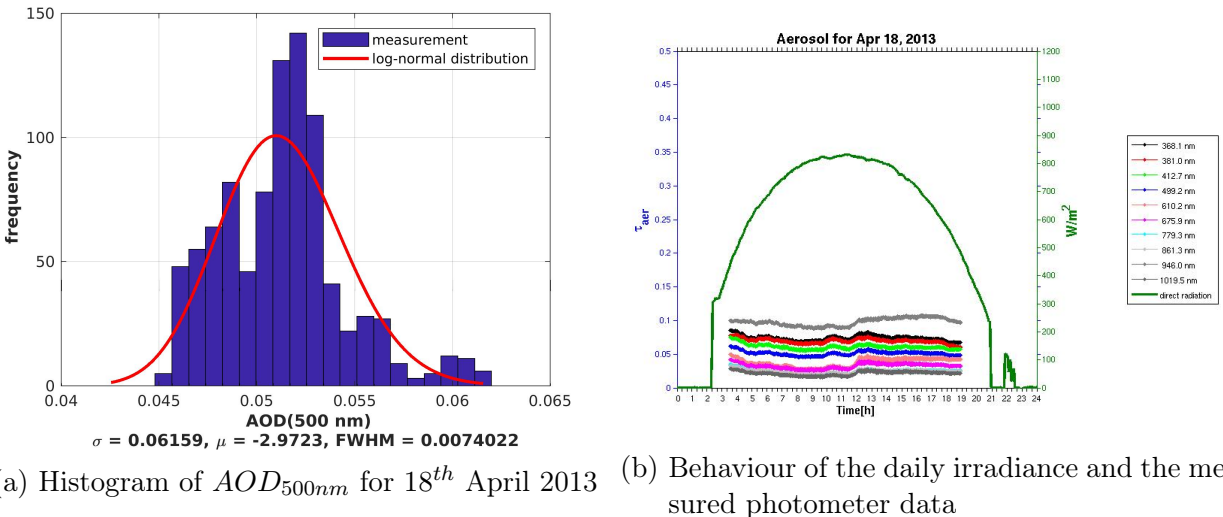


Figure 14: 18th April 2013 as an example of a very clear day with only small fluctuations in all 10 wavelengths (right) and the corresponding histogram (left)

Looking at numerous days between spring and autumn the algorithm failed due to missing convergence of the fitting parameters or unphysical results such as:

- Extremely large exponents ($a_2, a_4 \geq 100$) with small optical thicknesses (a_1, a_3)

- One of the prefactors a_1 or a_3 is negative when the corresponding exponents are very close to each other $a_2 \simeq a_4$. In the limes of small differences this algorithm becomes equal to the linear fit with only one summand.

To summarise the ansatz with two components is not an improvement to the traditional Ångström law in equation 3.6.

Figure 15 shows the fraction of the previously assumed parameters to the calculated ones as a fluctuation of the added noise to the AOD. The graphs of figure 15 in blue are the first summand and red the second one of equation 3.10.

The error for first summand with a_1 , allocated with aerosol, and a_2 , connected to clouds, in all cases is much smaller than for the second one, which also diverges first.

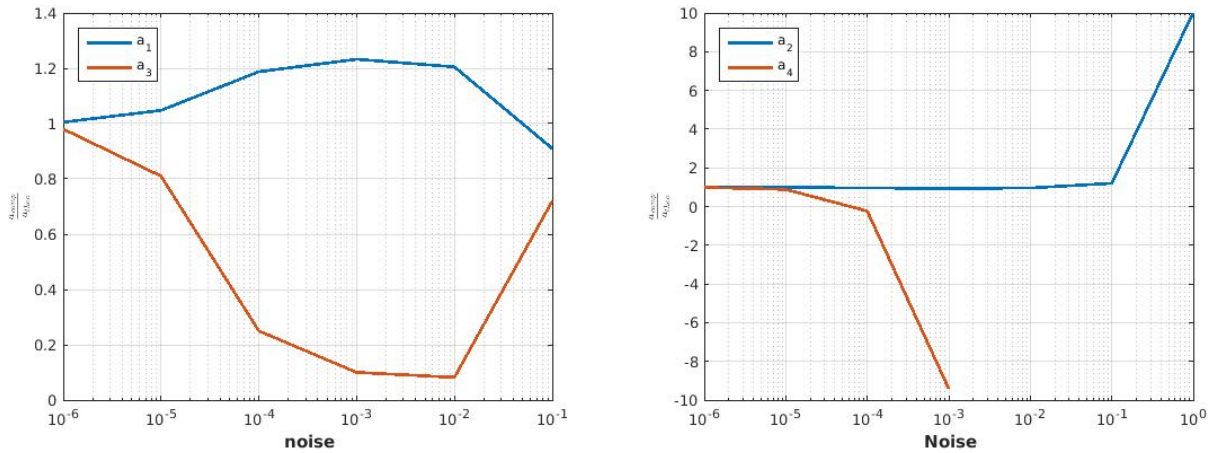


Figure 15: Quotient of computed to artificial parameters for a_1 , a_3 (left) and a_2 , a_4 (right)

The clear day was used to give the scatter of the AOD expecting 0.007 which is approximately 1% of the AOD but the code converges only at 10^{-3} . This means the chosen ansatz (equation 3.10) is nice, physically motivated but requires one order of magnitude more precise measurement data until Levenberg-Marquardt algorithm will have a chance to retrieve the correct solution from the observation data. Hence, this algorithm, as it is, is not suitable for the sun photometer standing in Ny-Ålesund.

With an improved photometer this algorithm can become useful for two constituents within the atmosphere and therefore two independent parameter sets for extinction and AOD. Improvements could be more measured wavelengths for fitting because in this case the code has more fix points and the fit curve is more accurate. Another possibility is a better resolution due to less technical noise production within the instrument. To get more information about the technical noise itself a calibration in a laboratory can also be done previously.

Wavelength dependent Ångström exponent

As a result of the clear improvement of the ansatz by Ångström (equation 3.6) with two independent components in equation 3.8, now a wavelength dependent Ångström exponent is

assumed and an ansatz with three wavelength independent fitting parameters C, α and β is chosen:

$$f_{lin}(\lambda) = C \cdot \lambda^{\alpha+\beta \cdot \lambda} \quad (3.12)$$

A Taylor expansion in the wavelength λ was done to Ångström ansatz in 3.6, leaving in zero order a constant parameter α with the same meaning as the Ångström exponent. It can also reach values in the interval $[-4 : 0]$. In the first order the correction is done by $\beta \cdot \lambda$ with β being the first derivative of α . β becomes more important the larger the wavelength dependency gets. Hence, the correction term is mostly effective to the infrared. The constant C is the same as in Ångström ansatz and does not depend on the wavelength.

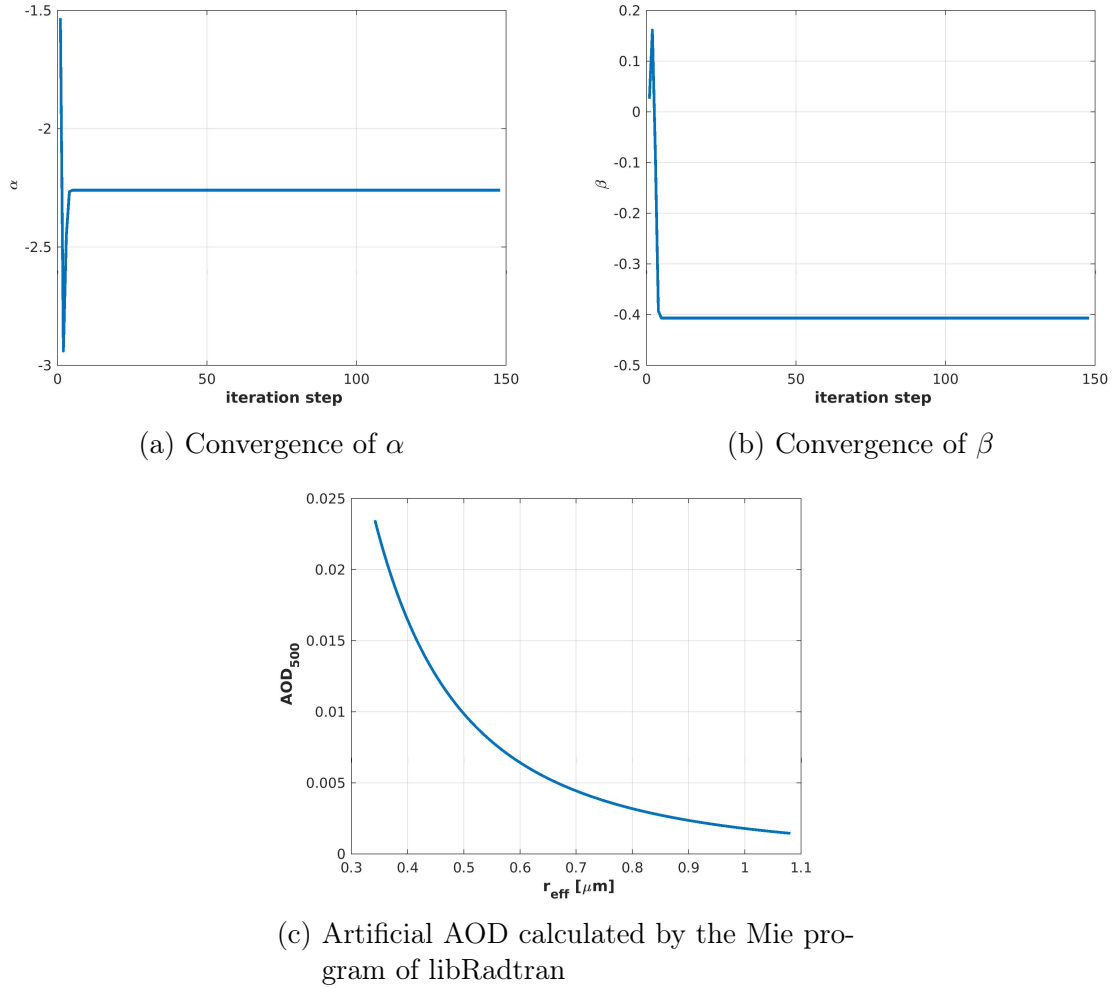


Figure 16: Convergence behaviour of the algorithm for both parameters α (a) and β (b) for the given AOD_{500} shown in (c)

For each minute during one day within up to 400 iterations or a difference of at least 10^{-11} between two computational steps the best fit for all three parameters C, α and β is numerically

computed again by Levenberg-Marquardt algorithm because only the elements of the Hesse matrix in this algorithm change. Instead of evaluating the second derivatives of the fit function $f_{artificial}(\lambda)$ in equation 3.10 due to a_1, a_2, a_3 and a_4 now the second derivatives of $f_{lin}(\lambda)$ in equation 3.12 to C, α and β are used.

To ensure the data has no noise, an artificial atmosphere was assumed calculated by the Mie program of libRadtran (see chapter 3.3). The given AOD is shown in figure 16c.

Figure 16 shows the convergence behaviour of the fitting equation 3.12 until the difference between two consecutive values does not change more than 10^{-11} anymore for all three parameters C, α and β . For this particular chosen AOD the code already reaches the final value after the third step. All of the following computations are only necessary for vernier adjustment.

After checking for artificial atmospheric conditions all real photometer data between 2009 and 2017 were computed with this wavelength dependent ansatz of the Ångström formula (equation 3.12). In 254,312 of all 255,389 cases (99.58%) a clear improvement was found like it can be seen in figure 17 for the 25th April 2015.

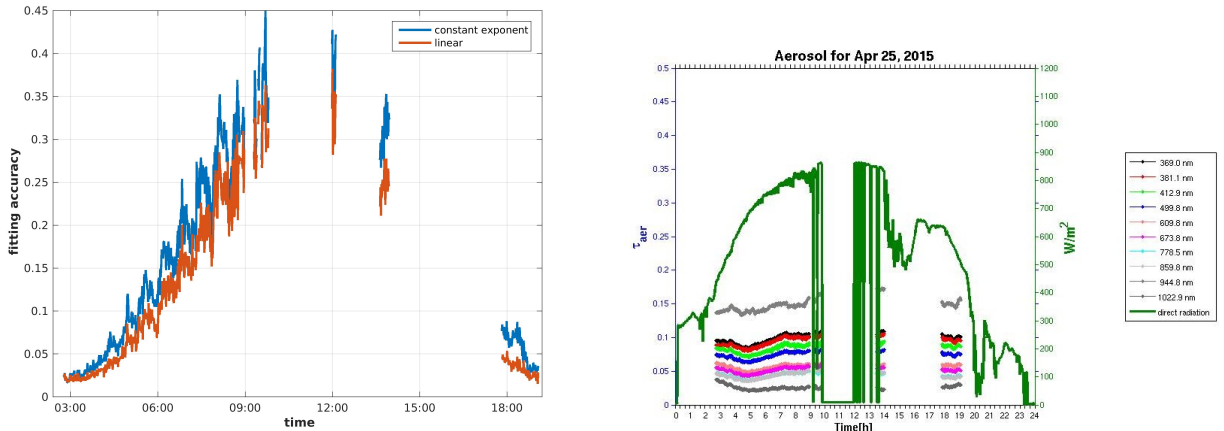


Figure 17: Example of a day with changes in atmospheric conditions and an improvement in fitting accuracy χ^2 due to wavelength dependent ansatz. Due to errors in the Langley calibration a daily pattern can be considered in the fitting accuracy of the data (Kreuter et al., 2013)

Therefore, the approach of the modified Ångström exponent and its spectral slope reveals is used for computing the AOD in this thesis because more information can be gained out of the measurement.

3.3. Mie Calculus

With libRadtran an artificial aerosol concentration was created. This distribution has effective radii between $r_{eff} = 0.01\mu m$ to $1.0\mu m$ and a refractive indexes of $n_1 = 1.44 + 10^{-5}i$ and $n_2 = 1.60 + 0.1i$ which are devoted to sulphate and soot, respectively. The wavelength interval is $[360.0 : 1030.0]nm$ with the step size of $5nm$ and has the same wavelength range as the sun photometer.

libRadtran

libRadtran is a widely used software package for radiative transfer calculations such as (polarized) radiances, irradiance and spectral fluxes in the solar and thermal part of the spectrum. Its spectrum of application lasts from remote sensing of clouds, aerosols and trace gases to radiative forcing due to different atmospheric components in planetary atmospheres. Beside of energy transport through the atmosphere also polarization, Raman scattering and molecular gas absorption or clouds are included. A complete description of libRadtran and all its input options is given in the user manual at <http://www.libradtran.org>.

For this work libRadtran was used to calculate the Mie scattering of solar shortwave radiation to test the modified ansatz by Ångström (equation 3.12) and generally to assess the information content of photometer data.

Error estimation using Mie calculus

Since the convergence of the modified Ångström exponent (eq. 3.12) has been shown recently, an improvement of the new ansatz compared to the traditional approach (eq. 3.6) has to be verified using noiseless data with known distribution parameters.

The AOD is always calculated monochromatically, often used the wavelength $\lambda = 500nm$. With libRadtran an artificial AOD τ_{lib} was created using the included Mie program. Additionally, a random number z following a Gaussian distribution centred around 0, a radius $r = 0.2\mu m$ of a Dirac-Delta distribution and a refractive index of $n = 1.60 + 0.01i$ and a noisy AOD profile τ_{noise} with the weight $m \in [0 : 0.02]$ is created so that the maximum noise level is $\Delta\tau = 0.02$:

$$\tau_{noise} = \tau_{lib} + m \cdot z \quad (3.13)$$

An example for the AOD with noise is plotted in blue with the fitting curve by the modified Ångström exponent in figure 18c. Even for a small noise level the traditional Ångström ansatz does not reproduce the initial AOD (see figure 18a). The errors of both approaches rise with increasing noise weight following the functions:

$$\begin{aligned}\chi_A^2(m) &= 2.0561 \cdot 10^{-7}m^2 - 3.0979 \cdot 10^{-5}m + 0.1141 \\ \chi_{tradA}^2(m) &= 9.5721 \cdot 10^{-8}m^2 + 2.1295 \cdot 10^{-6}m + 0.0180\end{aligned}$$

Additionally, the difference between both approaches, $\Delta\chi^2 = \chi_{mod.A}^2 - \chi_A^2$, rise with increasing noise weight as well (see figure 18b). It is worth to emphasise the noiseless case for $n = 0$.

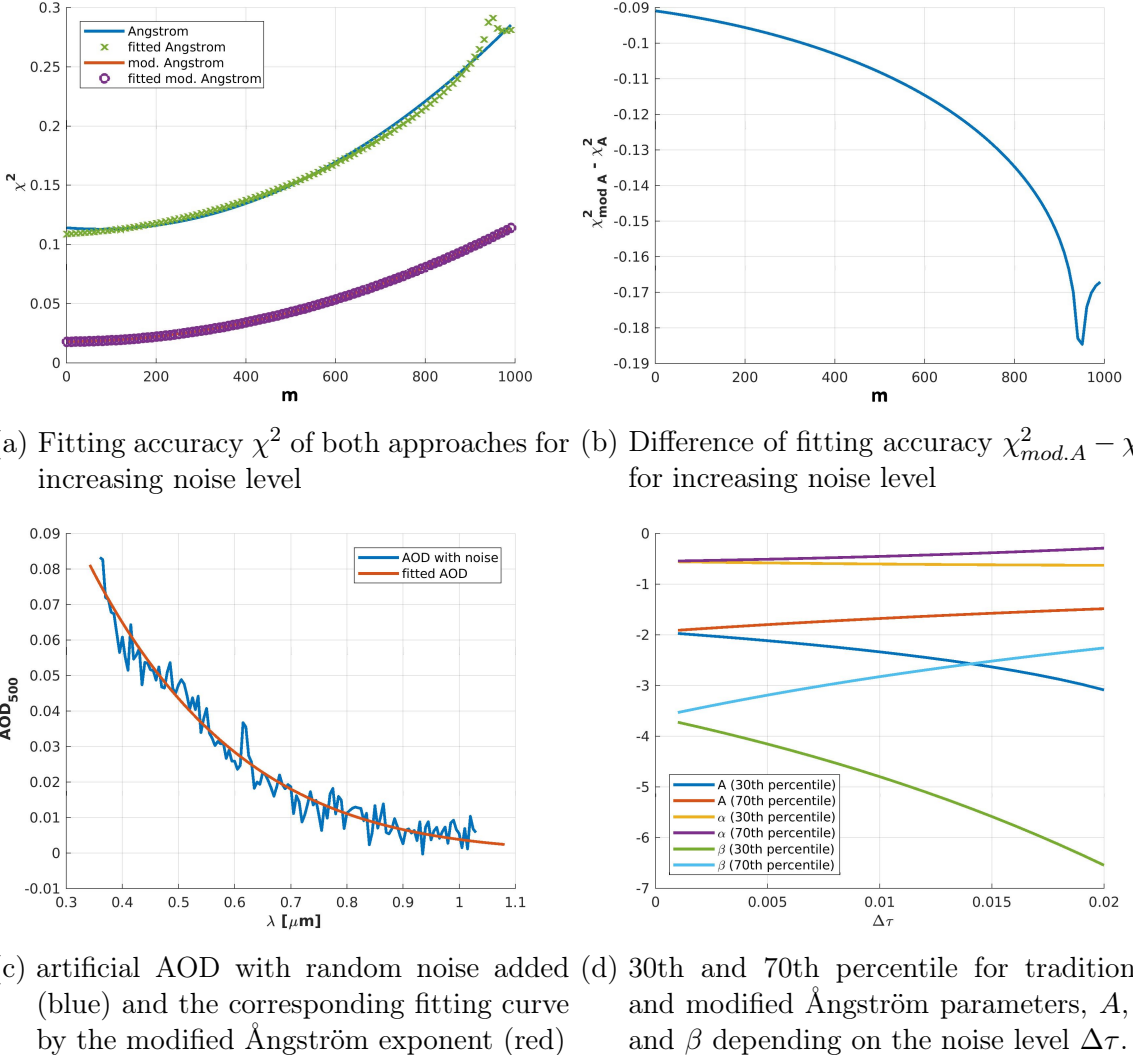


Figure 18: Fitting accuracies χ^2 for the traditional and the modified Ångström ansatz.

Here χ_A^2 is larger than χ_{linA}^2 by factor 10.

For 100 times the parameters A , α and β of the traditional and modified Ångström exponent are fitted to the same noise level with a maximum error of $\Delta\tau = 0.01$, created by a Gaussian distributed random number z , which is at the same time the maximum error of a sun photometer. The sensitivities of the algorithms are then estimated by the difference between the 30th and 70th percentile and shown in figure 18d. The intrinsically noiseless AOD is then combined with the random noise:

$$\tau_{noise} = \tau_{lib} + z \cdot \Delta\tau \quad (3.14)$$

A normalisation is such selected that the maximum $\Delta\tau = 0.01$, which is by the same time the maximum error of a photometer measurement.

Compared to the traditional Ångström exponent A with a derivation of $\Delta A_{\Delta\tau=0.01} = 0.32935$,

α of the modified one is much less affected by an increasing noise level ($\Delta\alpha_{\Delta\tau=0.01} = \pm 0.0752$). The most sensitive parameter is β with $\Delta\beta_{\Delta\tau=0.01} = \pm 0.98665$.

Although the error in β is very large, α and A give a rough estimation about the particle size using the theoretical limits of scattering theories. Because α and A carry the same amount of information this estimation of the particle sizes can be improved due to a smaller error.

Weighted variability

The main goal for using Mie calculus in this thesis is to prove if the modified Ångström exponent has a better fitting accuracy and more physical information can be obtained by using this ansatz.

It is known by scattering theory that scattering efficiency strongly depends on the particle size. The smaller a particle is the less efficient the scattering of light takes place. On the other hand the particle density for smaller particle sizes can be increased to compensate the lower scattering efficiency. It was chosen that there should be only 1 particle per ccm for the largest radius, $r_{eff} = 1\mu m$ while there are 100 particles per ccm for the smallest effective radius, $r_{eff} = 0.1\mu m$ and a linear interpolation between these points. A log-normal distribution was chosen up to a maximum radius of $r = 10\mu m$ and a refractive index of $n = 1.60 + 0.01i$. This leads to the function for the particle concentration:

$$f(r_{max}) = -110 \cdot r_{eff} + 111$$

This is added to the noisy AOD calculated by libRadtran in equation 3.13:

$$\tau_{noise} = \tau_{lib} \cdot f + m \cdot z$$

As it can be seen in figure 19 the deviations for A and α do not vary as much as β , especially for larger particle radii r_{eff} . Generally the error rises for increasing r_{eff} due to convergence to grey approximation.

For the smallest and largest particles the uncertainties of all parameters increase. For this very reason one can not draw a conclusion about the particle distribution only by having the calculated parameters.

Taking the plots of figure 19 the parameters for accumulation mode particles can be determined by maximum $A = \pm 0.001$, $\alpha = \pm 0.001$ and $\beta = \pm 0.005$.

Comparison between traditional and modified Ångström approaches

Contrary to observational data artificial data of AOD does not have noise and the parameters of the aerosol distribution are already known.

Again for this calculations a log-normal distribution with a maximum radius of $10\mu m$, standard deviations of $\sigma_1 = 1.3$, $\sigma_2 = 1.5$ and $\sigma_3 = 1.7$ and two different refractive indexes of exemplary $n_1 = 1.44 + 10^{-5}i$ (sulphate) and $n_2 = 1.60 + 0.01i$ (soot) were chosen.

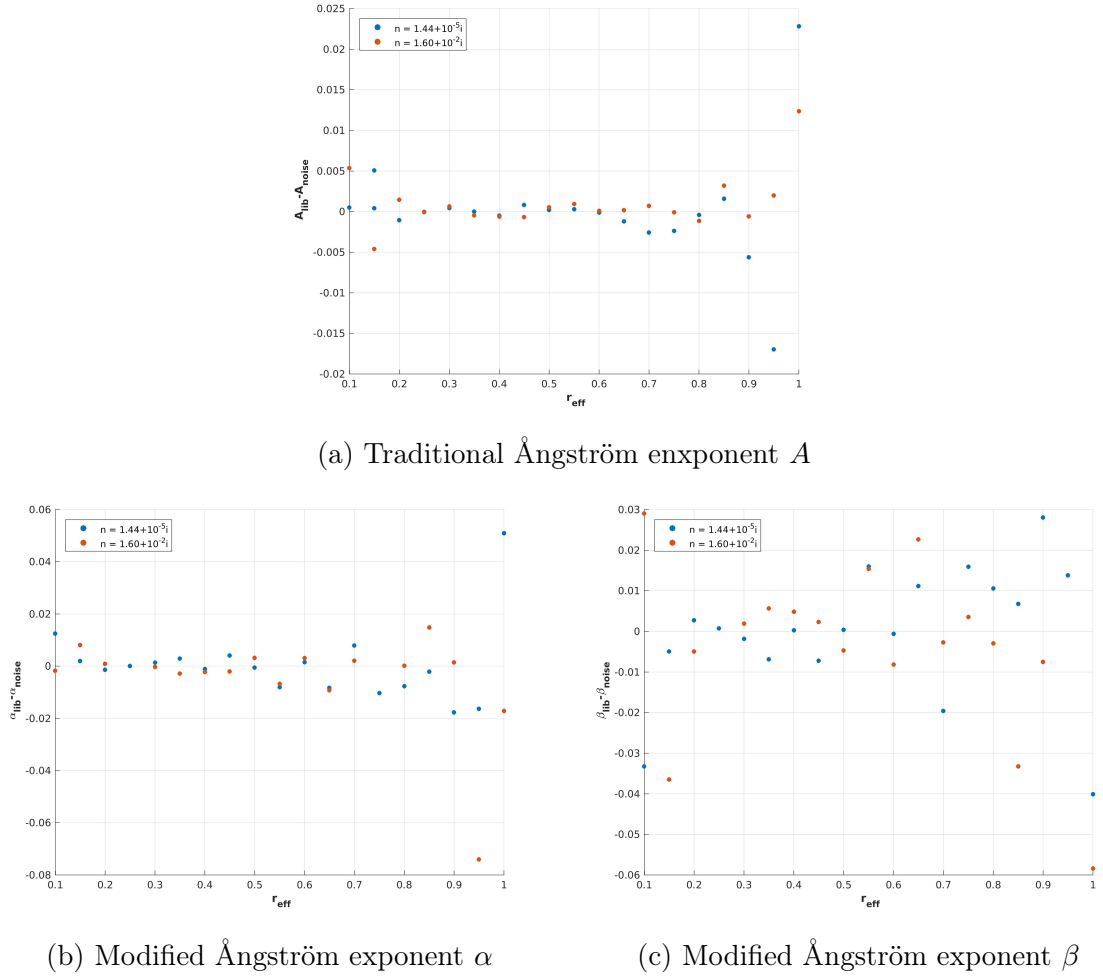
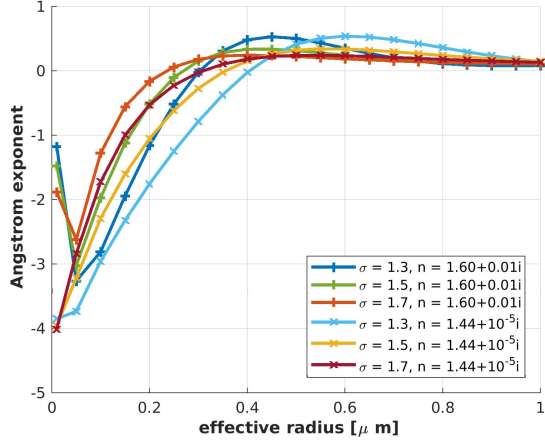


Figure 19: Weighted deviations between the parameters calculated without noise, indicated by index lib and the parameters calculated with noise, indicated by index $noise$.

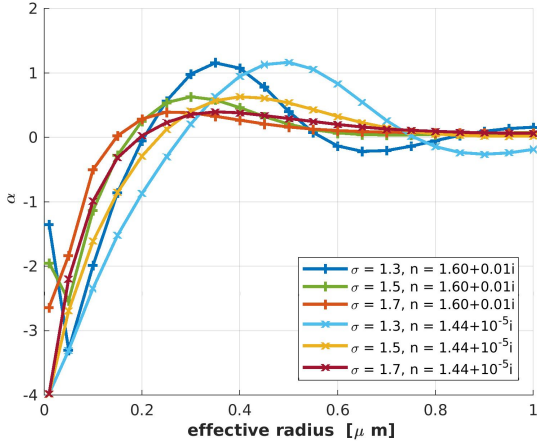
The traditional Ångström exponent A does not show large differences for various standard deviations σ of the aerosol particle size distribution. Therefore, for a given A it is difficult to determine the effective radius r_{eff} as well as the standard deviation σ for both different refractive indexes (figure 20a). For distributions with an effective radius $r_{eff} > 0.4\mu m$ all curves are very similar and due to the above discussed error accuracy no distinction between these cases is possible anymore.

For a given σ the pattern of the curves are shifted to larger r_{eff} and larger values of α and β , indicating the dependency of the traditional Ångström exponent to the refractive index n and to the effective radius r_{eff} : $A = A(n, r_{eff}) \sim n \cdot r_{eff}$.

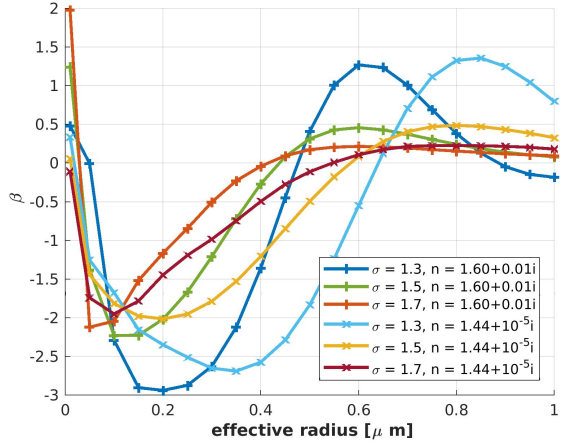
Consequently, with this ansatz and a given value for the traditional Ångström exponent it is not possible to obtain any information about the size distribution, when the particles are already in coarse mode.



(a) Traditional Ångström exponent A and both refractive indexes.



(b) Modified Ångström exponent α and both refractive indexes.



(c) Modified Ångström exponent β and both refractive indexes.

Figure 20: Radius dependency of traditional and modified Ångström exponent A , α and β for different refractive indexes and standard derivation σ .

Contrary to the traditional Ångström exponent A , the modified one α shows a larger difference between the minimum and maximum value for a given n and changing σ as well as the other way around. Also including errors in the calculation, the different curves can be distinguished better than with the traditional ansatz. The point of intersection of α is shifted to smaller r_{eff} for larger σ .

For larger σ the size distribution becomes broader, because more and larger particles contribute to the scattering of the aerosol cloud with a higher scattering efficiency and dominate the behaviour of the distribution.

Compared to the just discussed parameters β shows the largest dependency on r_{eff} , σ and n . The smaller n gets the larger r_{eff} is at the point of intersection. Additionally the difference

3. Data Processing and Methods

between the maximum and the minimum depends on σ and follows an indirect dependency. As it can be seen in figure 20, the size distributions with $r_{eff} > 0.4\mu m$ are distinguishable and all discussed parameters can be read out of the figure. Additionally, the function does not show a simple pattern and even for given values of the parameters more pairs of solutions are possible. Now, with a slight change in the fitting equation to the modified Ångström law this problem should be solved in best case.

The modified Ångström exponent has two parameters carrying information, which are fitted to the same AOD. After the algorithm has calculated both parameters for every measurement data set the effective radii and the refractive indexes can be estimated with the aim of figure 20. A possible solution can only be found if α and β have the same r_{eff} within their error margin. Finding the right one also gives either the standard deviation of the size distribution or the refractive index. Using other instruments, like Lidar or in-situ instruments, the refractive index can be measured.

Udisti et al. (2016) found sulphate with aerosol in-situ measurements at the ground in Ny-Ålesund as the most dominant aerosol type. According to Tunved et al. (2013) they are tiny. But in observation data displayed in figures 27 and 34 for April and August show an accumulation for values around $\alpha \simeq -1$. For that reason large particles must be in the atmosphere dominate scattering processes of solar and stellar radiation on particles with a much higher refractive index.

refractive index $n_1 = 1.60 + 0.01i$			
σ	A	α	β
1.3	$r_{eff,1} = 0.01\mu m$	$r_{eff} = 0.13\mu m$	$r_{eff,1} = 0.11\mu m$
	$r_{eff,2} = 0.18\mu m$		$r_{eff,2} = 0.34\mu m$
1.5	$r_{eff} = 0.14\mu m$	$r_{eff} = 0.09\mu m$	$r_{eff,1} = 0.09\mu m$
			$r_{eff,2} = 0.20\mu m$
1.7	$r_{eff} = 0.10\mu m$	$r_{eff} = 0.07\mu m$	$r_{eff,1} = 0.11\mu m$
			$r_{eff,2} = 0.34\mu m$
refractive index $n_2 = 1.44 + 10^{-5}i$			
σ	A	α	β
1.3	$r_{eff} = 0.16\mu m$	$r_{eff} = 0.10\mu m$	$r_{eff,1} = 0.09\mu m$
			$r_{eff,2} = 0.16\mu m$
1.5	$r_{eff} = 0.21\mu m$	$r_{eff} = 0.14\mu m$	$r_{eff,1} = 0.06\mu m$
			$r_{eff,2} = 0.35\mu m$
1.7	$r_{eff} = 0.28\mu m$	$r_{eff} = 0.19\mu m$	$r_{eff,1} = 0.05\mu m$
			$r_{eff,2} = 0.16\mu m$

Table 7: Different possibilities for an effective radius, r_{eff} , depending on the standard deviation σ of the distribution and refractive indexes n_1 and n_2 for given parameters $\alpha = -1$, $\beta = -1.5$ and $A = -1$. The best matching combination of α and β is highlighted.

Assuming a result of $\alpha = -1$, $\beta = -1.5$ and $A = -1$ for both above mentioned refractive indexes n_1 and n_2 . With figure 20 one can try to estimate the effective radius, the refractive index and the standard derivation of the artificial aerosol size distribution.

Using the plots for A , α and β in figure 20 the corresponding effective radii can be read. A matching of the effective radius can be obtained by comparing the possible solutions for both parameters α and β . This example yields either to an effective radius $r_{eff,1} = 0.09\mu m$ at a standard deviation $\sigma = 1.5$ for n_1 or to $r_{eff,2} = 0.10\mu m$ for n_2 and $\sigma = 1.3$.

Even though there are two possibilities using the modified Ångström ansatz for the refractive index and the standard deviation, the effective radius of the underlying distribution can be determined. On the other hand there are in total seven possible combinations using the traditional Ångström ansatz for fitting, spanning an interval over more than one magnitude for the effective radius, but only two using the modified Ångström law.

To conclude, using the traditional ansatz, one can not gain any information about the distribution. On the other hand, the modified ansatz already provides information about the effective radius.

3.4. Case study

For several days with only short appearing clouds the three parameters A , α and β were compared. In the photometer data (figure 21b) on the 6th April 2014 the cloud can be recognized easily between 2:30 and 4:30 p.m. by the sudden increase of all three parameters. With the Lidar KARL, aerosol layers and clouds can be detected by measuring the backscattered laser beam.

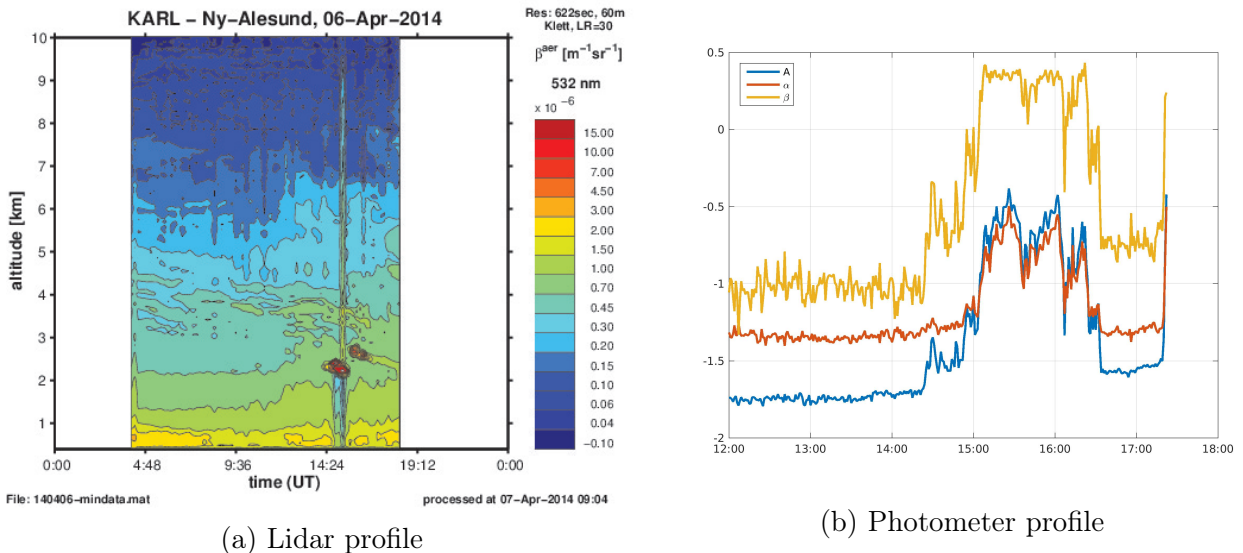


Figure 21: Example of a clear day with a small cloud appearing at 2:30 p.m. with changes in the computed Ångström parameters afterwards

In comparison of both instruments several aspects can be found:

Generally the aerosol in the Arctic is quite small as indicated by the small Ångström exponent. This is in agreement to earlier photometric studies (Stock, 2010; Tomasi et al., 2015) as well as to in-situ measured size distributions by Tunved et al. (2013). A slightly higher modified Ångström exponent α was found for aerosol but its variation between aerosol and clouds is slightly smaller because the spectral dependency β is independent from α . The second parameter of the modified Ångström ansatz, β , is generally negative for aerosol which is obviously smaller than $0.4\mu m$. Because of the wavelengths dependency of the whole exponent, $\alpha + \lambda \cdot \beta$, the UV part of the spectrum is much less affected by this modification than the IR part compared to the normal Ångström ansatz. Such a behaviour is reasonable as the UV light perceives the existing particles as larger than the IR light. In clouds β may change its sign. Hence, clouds can have a spectral slope opposed to aerosol with an exponent close to zero for IR with slightly negative values for the UV. Therefore, the grey approximation seems to be less valid for UV in the clouds.

The detection of the cloud in both instruments, Lidar and sun photometer, has a tiny shift in time. First the photometer saw the change of AOD due to the cloud, then the cloud also passed by the Lidar. This difference can be explained by the different lines of sight. Whereas the Lidar measures perpendicular to the ground, the photometer has to follow its light source. In general the sun has only a small elevation, even in summer times when there is polar day. This fact is not trivial when comparing photometer and Lidar.

For clouds the modified and the constant Ångström exponent nicely follows each other whereas there is a large difference at clear sky conditions. After the cloud has passed by, the Ångström exponent, A , increases slightly. On the other hand α remains constant, only β changes. This indicates a modification in the particle size distribution however all other aerosol properties remain constant.

At 13 a.m. in the photometer profile of figure 21b the values for the three fitting parameters can be read out of it with $\alpha = -1.3$ and $\beta = -1.75$. Taking figure 20 into account a particle size distribution with the parameters $\sigma = 1.5$ and $r_{eff} = 0.1\mu m$ at a refractive index of $n = 1, 44 + 10^{-5}i$ can be found.

With the Lidar ratio, LR , the extinction can also be calculated. This is used as an indicator of the comparability of both instruments.

Using figure 21a the parameters for cloud thickness $\Delta z = 500m$, the Lidar ratio $LR = 30$ and the backscattered ratio $b = 15 \cdot 10^{-6} m^{-1} sr^{-1}$ can be estimated:

$$\begin{aligned} LR &= \frac{a^{aer}}{b^{aer}} \Rightarrow a^{aer} = LR \cdot b^{aer} \\ \Rightarrow \tau &= \int_{z_0}^{z_1} a^{aer}(z) dz \\ &= LR \cdot \int_{z_0}^{z_1} b^{aer}(z) dz \\ &\simeq \Delta z \cdot LR \cdot b^{aer} = 0.225 \end{aligned}$$

The photometer measures an $AOD_{500} = 0.25$. The major difference of both measuring instruments can be caused by the different lines of sight or the temporal evolution of the cloud itself.

To conclude, both devices can be compared if the atmosphere is well mixed on larger scales because both instruments always have a differs line of sight. But they can measure different aerosol optical depths due to temporal and spatial evolution of the cloud or aerosol layer. To get more information out of one instrument the other can be taken into account.

3.5. Error Estimation

To evaluate the measurements an error estimation is obligatory. In general there are three different types of errors that all have to be taken into account:

1. Systematic error of the instrument

The error of the instrument is determined by the uncertainty of the filters that measure the FWHM of signal $U = U_0 \cdot r^{-2} \cdot e^{-\tau \cdot m}$, where U_0 is the extraterrestrial voltage and computed by Langley calibration, τ the AOD and m the air mass. The manufacturer Dr.Schulz & Partner GmbH states an uncertainty of the wavelength with $\Delta\lambda = \pm 2nm$ and for voltage $\Delta U_0 = \pm 0.1mV$, whereas the signal is amplified up to 4V. Errors in the calibration and in the assumption of ozone concentration are typically the largest sources of uncertainty in determining the AOD. This error manifests itself in a diurnal variation, symmetrically around local solar noon because the measured signal reaches its maximum and on the other hand differs most with the calibrated atmosphere. During sunset and sunrise the difference between measured and calibrated signal is almost the same and the error is minimal (Kreuter et al., 2013).

2. Errors appearing due to determination of the Ångström coefficients

The Ångström exponent is calculated by a wavelength dependent modification of the Ångström exponent via Levenberg-Marquardt algorithm. Because second derivatives are calculated, the fitting parameters are much more stable to noise than only using linear regression. An estimated error of the Ångström exponent is given by the FWHM of a very clear day.

3. Computation of the AOD

The maximal error of the AOD is calculated by the arithmetical error propagation law:

$$\Delta\tau = \left| \frac{\partial\tau}{\partial x_1} \right| \cdot \Delta x_1 + \left| \frac{\partial\tau}{\partial x_2} \right| \cdot \Delta x_2 + \dots \quad (3.15)$$

Because the calculation of the AOD is very complex every relative error is estimated one by one and concatenated. The detailed computation is done in Stock (2010).

In summary one get maximal errors for each parameter which is needed to compute the AOD:

Parameter		Error
wavelength	λ	$\pm 2\text{nm}$
measured voltage	ΔU	0.1mV
extraterrestrial voltage	U_0	$< \pm 0.5\%$
ozone optical thickness	$\Delta\tau_{O_3}$	$\pm 3\%$
AOD	τ_A	$\lambda > 400\text{nm} : \pm 0.01$
	τ_A	$\lambda < 400\text{nm} : \pm 0.02$

Table 8: Estimated errors of measured parameters

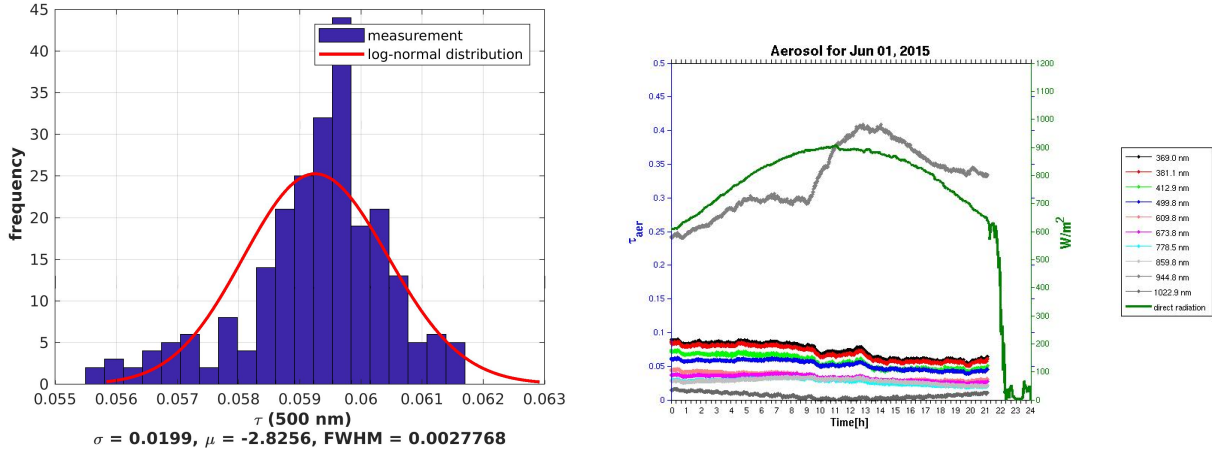


Figure 22: Photometer measurement of a day with constant atmospheric conditions (between 5 and 9 a.m.)

To get a reasonable estimation for the error of the AOD, a very stable day, like 1st June 2015 (figure 22) is chosen.

The FWHM of the AOD is a good estimation for the maximal uncertainty of the measured data. Taking this approach, the variability of the AOD becomes $\Delta\tau = 0.0027768$ which is only about $1/40$ of the maximal error computed in table 8. Compared to the maximal error of $\Delta\tau = 0.01$ in Stock (2010) the given error is much smaller. Hence, errors by calibration or ozone correction may dominate the errors in AOD but not the noise in the signal.

In comparison with all of the previous mentioned data processing methods the modified Ångström ansatz with a wavelength dependent Ångström exponent is chosen as a balance between best gain of information and numerical stability.

3.6. Back-trajectory analysis

To understand the origin of the aerosol it is a common method to employ backward air trajectories (Rozwadowska et al., 2010) or a large scale circulation pattern (Eckhardt et al., 2003), even in remote sites as in the Arctic, where the meteorological data is probably worse than in

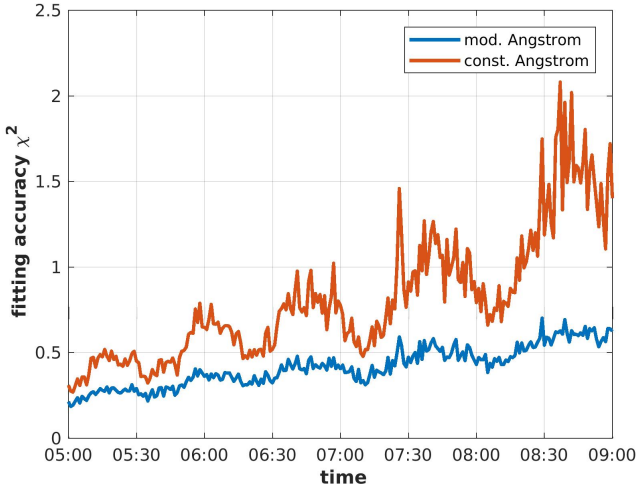


Figure 23: Minute-by-minute error for the ansatz with an Ångström exponent linearly depending on wavelength (blue) and a constant Ångström exponent (red)

the mid-latitudes. In this work 5-days back-trajectories using the kinematic trajectory model FLEXTRA (FLEXible TRAjectory model) based on ERA-Interim reanalysis data from the European Centre for Medium-Range Weather Forecast (ECMWF) were used and are directly calculated on the ECMWF eta levels. Turbulences or loss processes are not included. The model produces the path of air parcel, its coordinates and provides also some meteorological information.

By default the arriving height of the air masses are set to 500m, 1000m and 1500m above Zeppelin Station, Ny-Ålesund, at 11 am. Therefore, only sun photometer data with $\pm 1h$ around the arriving time are considered to ensure that all back-trajectories are computed for the same air masses the photometer detected. The resolution of the model is $0.75^\circ \times 0.75^\circ$.

Longer back-trajectories are not recommended as the insecurity due to the sparse meteorological data in this region will become too large (Stock et al., 2014). The spatial error is roughly 20% of the already passed trajectory (Stohl and Seibert, 1997). The multi-modal AOD distributions were considered only to show back-trajectories with low or high AOD, respectively.

For the sea ice concentration a monthly mean of daily maps was made also using ERA-Interim data. Sea ice is a very good insulator between the warm ocean and the cold atmosphere. Even small sea ice leads ($> 5\%$) drastically effect the boundary layer and create a strong latent heat flux from the ocean to the air inducing convection and destroying the stable stratified boundary layer (Lüpkes et al., 2008). Therefore, every grid cell with a sea ice concentration less than 95% is automatically counted as "ocean".

A problem of the used sea ice concentration map is that there is no information about the snow cover on continents. Hence, one can not determine which kind of aerosol is emitted there only using this map. To improve the prediction of the aerosol origin maps of anthropogenic or biomass burning aerosol emission of the northern parts of Russia, North America and Europe

3. Data Processing and Methods

would be useful. While the air parcel remains in the boundary layer the probability rises for a higher aerosol load and therefore higher AOD. With the improvement of these maps the prediction of the time the air parcel remained in the boundary layer over land is improved and a clearer source of the aerosol region can be determined.

Tropospheric aerosol is affected by relative humidity as well as by the ground which operates like sinks and sources depending on the local properties. The origin and deposition of aerosols following into the Arctic is investigated looking to the fraction of time the air was in the boundary layer, here parametrised with a height above the 900hPa level.

Due to larger errors in the calculation of relative humidity in the ERA-Interim model and only a small data set, the focus on the analysis is put only on the "dry" cases. An additional advantage of this choice is also the absence of a wet aerosol deposition. So only the ground can act as a sink.

4. Results

4.1. Trends in the AOD

A few studies with the sun and star photometer have already been carried out starting in 1991 (Herber et al., 2002; Stock, 2010; Tomasi et al., 2015). The longer the data series is lasting the better trends can be seen. In the following the years are divided into polar night and day because of the use of the instruments with only a small overlap in spring and autumn.

4.1.1. Polar day

Within the 13 years between 2004 and 2017 in general the AOD changed in every chosen season. The Arctic Haze arises in the months of March and April over the Arctic and Svalbard and is summarised as "spring". The month of May is ignored because it is the transition month between spring and summer (June to August). Autumn is only represented by September. In Ny-Ålesund the elevation of the sun after the 8th October is already too small, so that it can not shine over the mountains in the South of the village and sun photometer measurements are not possible anymore.

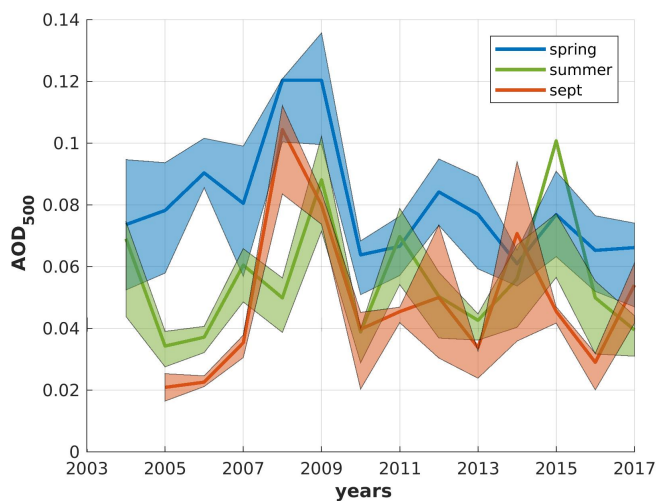


Figure 24: Seasonal means of the aerosol optical depth with "spring" being the mean of the March and April, "summer" being July and August and September as a representative for the only autumn month with sun photometer measurements of the years 2004-2017. The shaded areas represent the 30 and 70 percentiles, respectively.

As it is shown in figure 24 the variability of each season decreases over the years with a slight trend of decreasing AOD in spring and increasing AOD in September. This indicates a change of the physical or chemical properties of aerosol or its load in the atmosphere over Ny-Ålesund. The 30 and 70 percentiles give an estimation of the statistical dispersion of the monthly AOD_{500} because 30% of the monthly means lie below or above the mean AOD_{500} . Especially during

4. Results

spring the shaded area decreased from 2004 to 2007, while the variability for summer months was increasing in the same period. Hence, the aerosol had to be changed and now more homogeneously distributed air arrives in Ny-Ålesund in spring. On the other hand it is more dispersed for summer months. This result leads also to the suggestion that there have to be changes in the annual cycle of the aerosol.

Now the question appears whether the changes of AOD variability are caused by more or less days with high AOD, as it were if clear days become even clearer or polluted days getting clean.

In figure 25 the number of days with $AOD_{500} < 0.1$ (dashed lines) and with $AOD_{500} > 0.1$ (solid lines) is plotted for the same periods as shown in figure 24 for the years 2004-2017.

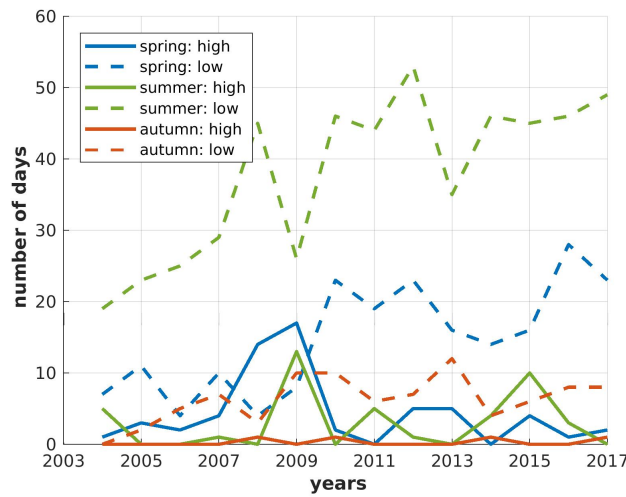


Figure 25: Numbers of days with $AOD_{500} < 0.1$ (dashed lines) and with $AOD_{500} > 0.1$ (solid lines) for the same periods as in figure 24.

Obviously, the days with low AOD increase in spring with less days of Arctic Haze. Therefore, the mean AOD decreases. On the other hand the number of low AOD increases as well, while the number of polluted days remains constant. At the same time the mean AOD of the season is constant. This observation can only be explained by an increase of the total AOD load on these few polluted days.

A clear change of the number of highly polluted days except for 2009 and 2015 can be seen in which at least two seasons show an increase. On the other hand a trend can be seen in the number of clear days. After 2010 the number of clean days increased rapidly by factor 2 for spring months and still remains at a high level.

Between 2004 and 2017 a clear trend of days in summer is shown, where the number of days increased by factor about 2.8.

4. Results

With Pearson's empirical correlation coefficient it can be shown whether two parameters are correlated statistically. It is defined in the following way, where $Cov(X, Y)$ is the covariance of X and Y , n the number of data points and σ_x , σ_y the standard deviation of X, Y , respectively. For $|\rho| < 0.3$, the parameters are non-correlated, for $|\rho| > 0.7$ they are strong correlated:

$$\rho_{X,Y} = \frac{Cov(X, Y)}{\sigma_X \cdot \sigma_Y} = \frac{\left(\frac{1}{n} \sum_{i=1}^n X_i Y_i\right) - \left(\frac{1}{n} \sum_{i=1}^n X_i\right) \left(\frac{1}{n} \sum_{i=1}^n Y_i\right)}{\sqrt{\left(\frac{1}{n} \sum_{i=1}^n (X_i - \bar{X})^2\right) \left(\frac{1}{n} \sum_{i=1}^n (Y_i - \bar{Y})^2\right)}} \in [-1, 1] \quad (4.1)$$

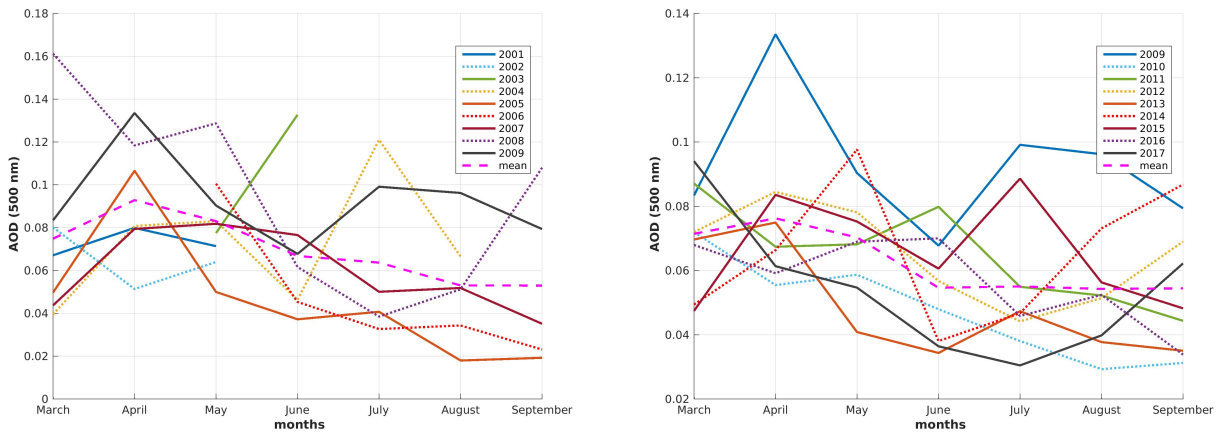
In the following discussion Pearson's empirical correlation coefficient is applied to the monthly mean AOD trends of the time periods 2001-2009 as X in equation 4.1 and for 2009-2017 as Y . Applying Pearson's empirical correlation coefficient ρ to the number of measurement days an answer concerning the influence between clear and polluted days can be given.

For spring the correlation is $\rho_{spring} = -0.4408$, which indicates a slight anti-correlation. As the numbers of polluted days decrease one can see an increase in clear days.

For the other seasons, summer and autumn, the correlation coefficients are $\rho_{summer} = -0.1423$ and $\rho_{autumn} = -0.0071$. Because in both cases the correlation coefficient ρ is close to 0, there is no dependency of days with high and less pollution.

Before showing the multi-annual monthly mean AOD of the wavelength $\lambda = 500nm$ and its change over time the different annual cycles of the AOD for Ny-Ålesund are presented first in figures 26a and 26b. A high year-on-year variability of the monthly mean AOD is evident. Whereas, the year 2009 does not represent an extreme polluted year in the earlier time period, its monthly mean is much higher than in all of the other following years. So the year 2009 was the last one with high AOD, both during the Arctic Haze season in spring and during the biomass burning season in summer. By comparison of figure 26a and 26b it is evident that the monthly mean AOD decreases over time and since 2009 no month with $AOD_{500} > 0.1$ has been recorded anymore. This is even more remarkable because the data coverage between 2001 and 2004 was poor due to the manual tracking system which did not permit to calculate monthly means for all months. However, no apparent transition between "polluted earlier years" and "clearer later years" is evident as the inter-annual fluctuations are high. For comparison the year 2009 is plotted in both figures. Nevertheless, the AOD decreases stronger in spring and early summer and remains almost constant at $AOD_{500} = 0.055$ in August and September. This makes the annual run of the AOD flatter and reduces the importance of the Haze season. With a micropulse Lidar (MPL) Shibata et al. (2018) found a similar trend of the annual cycle of aerosol load with decreasing importance of the Arctic Haze season in Ny-Ålesund.

The empirical correlation coefficients ρ for monthly mean AOD for $500nm$ ρ_{AOD} and the theoretical Ångström exponent ρ_A for the two time series 1995-2008 (Stock et al., 2014) is compared to the newer set 2009-2017. A strong linear dependency can be found for AOD with $\rho_{AOD} = 0.7483$ due to the same pattern from March to May and an offset but continues differently later on. From that point of view there is only a small change in spring months, the same pattern but lower mean AOD, but the atmosphere changed in summer and September between the chosen time intervals. In later times the monthly mean AOD_{500} remains constant and on a lower level than the original one between June and September. Because of the strong



(a) Monthly means in AOD for the years 2001-2009 (b) Monthly means in AOD for the years 2009-2017

Figure 26: The dashed magenta line is the mean of the time interval. Note that the year 2009 is plotted in (a) as well as in (b) for comparison.

deviation for later months and Pearson's empirical correlation coefficient close to the border between intermediate and strong dependent regime, the dependency here is only intermediate. On the other hand, there is a negative linear dependency of the Ångström exponent indicated by a negative correlation coefficient $\rho_A = -0.3085$. This factor is very close to the threshold of no (anti-correlated) dependency.

Considering not only the changes in the monthly means in AOD but also in the Ångström exponent there have to be significant changes in physical properties of the aerosols arriving over Ny-Ålesund within the years 2001-2017.

Summarising the mean AOD in spring decreases because the numbers of polluted days decrease as well. Contrary, in summer the AOD remains constant while the Ångström exponent A slightly is increasing. To prove that the atmosphere is changing since 2001 Pearson's empirical correlation coefficient was calculated and it indicates that the changes must have a physical and not a statistical reason.

4.1.2. Polar night

Between 1993 and 2014 a significant warming up to 3 Kelvin of the free troposphere per decade was measured by radiosondes launched from Ny-Ålesund in winter but almost no trend in summer was found (Maturilli and Kayser, 2017). This fact shows that the atmospheric parameters in terms of temperature and relative humidity differ from summer to winter times. That's why an all-year round measurement is crucial for understanding the atmosphere. Hence, the same effect can occur for aerosol load and their properties. Additionally, other mechanisms can take place in attendance or absence of the sun.

When polar night starts in Ny-Ålesund at the beginning of October, sun photometry is not possible anymore. Every year a more or less decreasing trend in AOD can be seen in sun

4. Results

photometer data. During the dark season the AOD must increase to obtain the high AOD which is measured when the sun returns. In winter times aerosol is still transported into the Arctic, reacts there and contributes to the optical thickness and the behaviour of the local polar atmosphere. For this reason the existing sun photometer data set is extended by measurements of stellar irradiances.

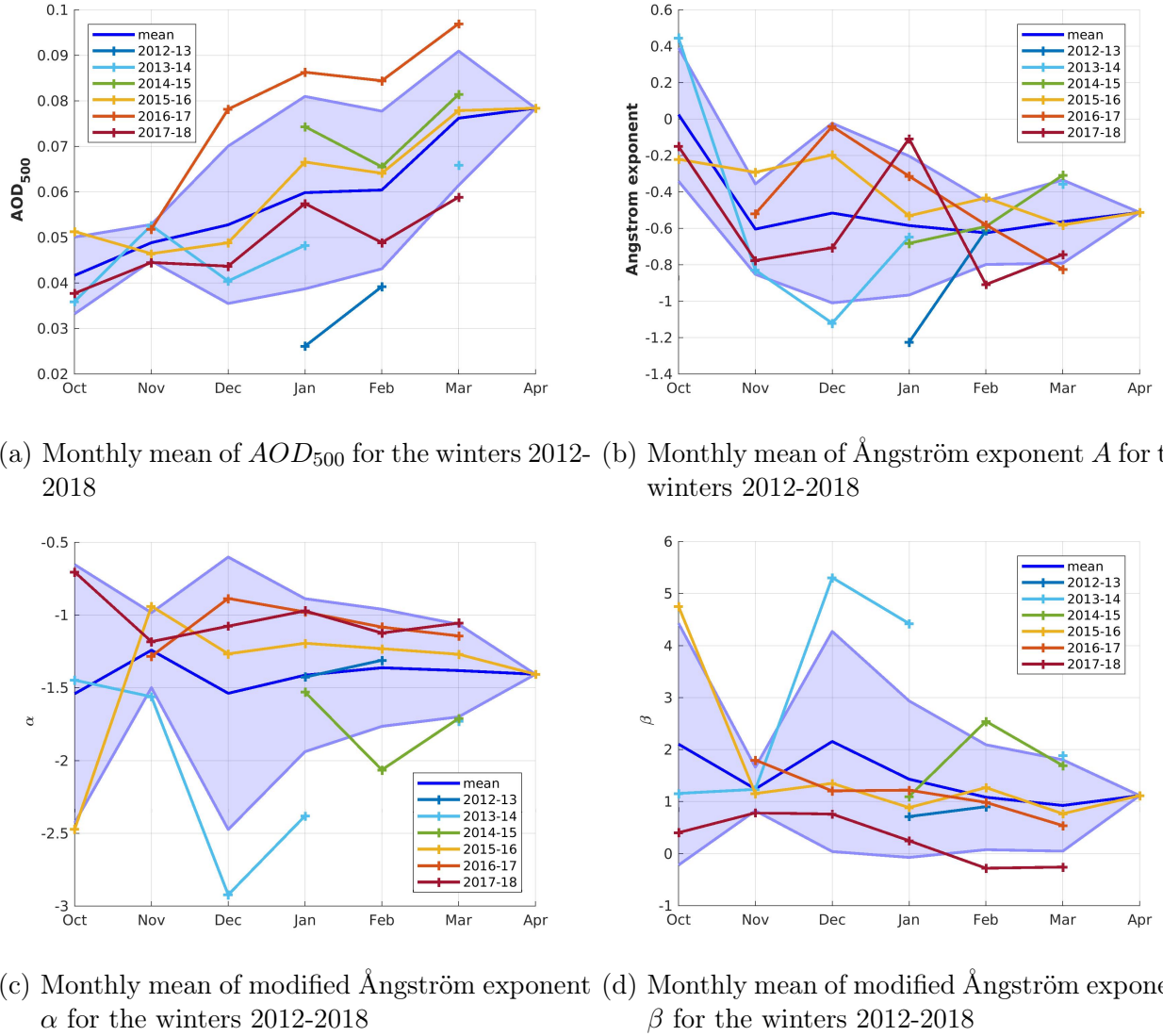


Figure 27: Monthly mean AOD of each month during polar night (2013-2017). The dark blue line is the mean of the time interval with the standard deviation as shaded area.

In figure 27 the monthly mean AOD for the dark months (October to March) 2012-2018 is plotted. The dark blue line indicates the mean pattern of the AOD trend. The AOD_{500} increases continuously (figure 27a). Each winter displays more or less the same pattern but the absolute values are shifted to higher or lower AOD.

The two parameters of the modified Ångström ansatz (equation 3.12), α and β , support this hypothesis more. Both parameters do not show a great month to month variability from November to April. In addition to that the monthly means become more and more similar, whereas the AOD rises in average over the winter while having smaller variability.

Contrary to the large variability of α and β the monthly mean of the traditional Ångström exponent does not vary very much over the years and months.

The aerosol optical depth is effected by the particle size, their scattering, extinction and absorption properties, as well as the total amount of particles in the atmosphere. The optical parameters are calculated by the Mie theory and the Ångström exponent. Additionally, the parameter β does not show significant variations from November to April. Hence, the particle size is also constant. The only possibility for a continuous increasing AOD_{500} is an increasing aerosol concentration.

A combined plot of the monthly mean AOD measured by sun and star photometer can be found in appendix 4.3.

4.2. Comparison of sun and star photometer

Changing the instrument can cause problems because every instrument has its own electronical noise, manufactured slightly differently and is calibrated with different gauge files.

In the Arctic only in months with sunrise and sunset a comparison of both instruments is possible. But the time of overlap is very limited to a few weeks in March and September. In this case study every instrument had a total different line of sight. While the Lidar observes the atmosphere in zenith the star photometer looks into the northeastern direction towards Vega, in the opposite direction where the sun set.

The sun photometer is calibrated once a year in Izaña, Tenerife. On the other hand the star photometer has not been used during the past years and therefore it has not been calibrated every year.

For the star photometer measurement the star αLyr (Vega) was selected with an elevation angle of $29^{\circ}23'46''$ and an azimuth angle of $29^{\circ}12'31''$ on the 26th March 2014 at 8:45 p.m.

Nevertheless, a rough quality check for the star photometer can be done using simultaneously Lidar and sun photometer during the short time period of the year when the sun rises and sets. The only suitable day fulfilling all of these requirements was the 26th April 2014.

For the comparison with the sun photometer, a clear day with a stable atmosphere is selected. The assumption was made that during sunrise and sunset the atmospheric conditions does not change and both instruments observe the same conditions.

The sun photometer had measured $AOD_{500} = 0.0318$ and $AOD_{1014} = 0.0083$, which is much less which KARL or the star photometer gauged a couple of hours later. As it can be seen in figure 28a the sun photometer did not see fluctuations during the measuring time. This difference might probably be caused by the various lines of sight, because in March the direct sunlight is still strongly influenced by the presence of summits of the surrounding mountains.

4. Results

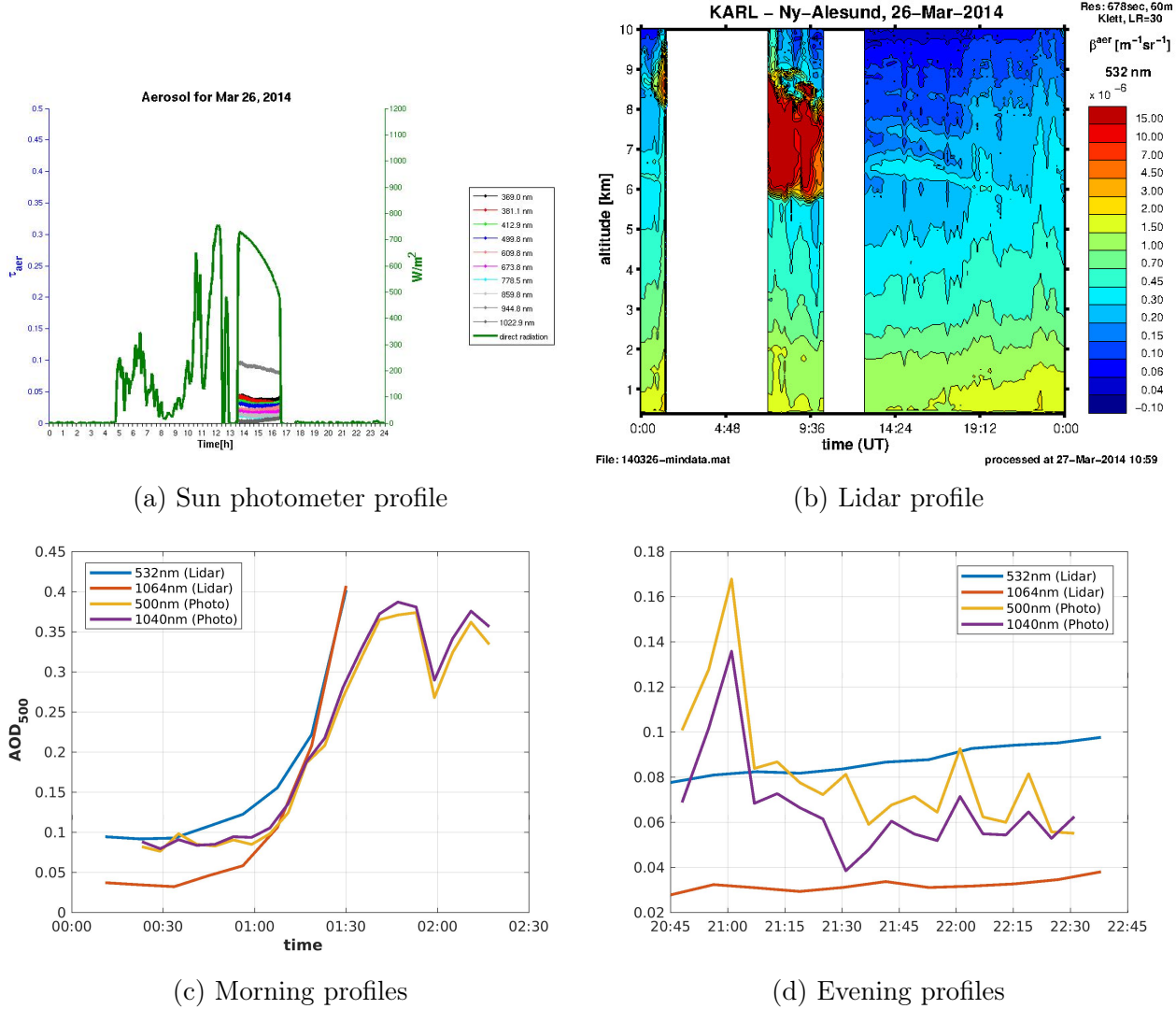


Figure 28: Comparison between most similar wavelengths of Lidar and star photometer for the morning and evening of the 26th April 2014.

For the early morning hours of the day and for a longer period in the evening Lidar and star photometer have been operated simultaneously. In both time periods the Lidar profile showed a larger difference between the wavelengths 532nm and 1064 compared to the closest comparable filters of the star photometer at 500nm and 1040nm.

To conclude, all three instruments measure slightly different air masses, which explains the different trends between the star photometer and the Lidar. Nevertheless, both instruments have seen the appearing cloud at the same time, indicated by a sudden rise of the AOD in all wavelengths. But the absolute values are not the same. Hence, a calibration of the star photometer and a reprocessing of old data with corresponding gauge files are needed.

4.3. Trend of AOD over the whole year

With the star photometer only the data starting in January 2013 until March 2018 is analysed. For this reason the sun photometer data is also confined to this time period although more data of both instruments is available. For star photometer data only data flagged as "aerosol" is taken into account.

Figure 29 shows the combination of the AOD measured by both photometers. The standard deviation of the monthly means is indicated by the bluish area with the mean indicated as a solid dark blue line. The annual cycle discussed in chapters 4.1.1 and 4.1.2 can easily be recognised here.

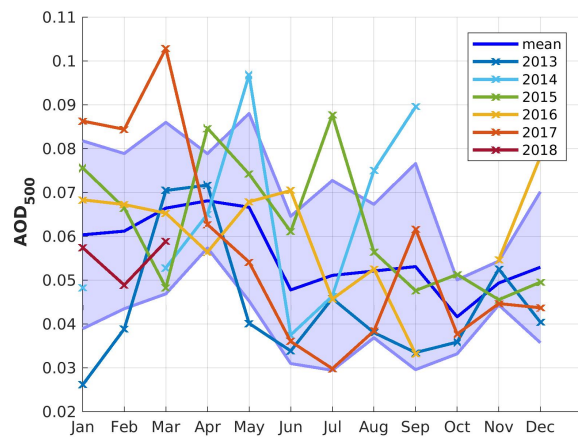


Figure 29: The annual cycle of AOD is shown by the combination of sun and star photometer

4.4. Comparison with previous measurements

In the years between 1991 and 1999 Herber et al. (2002) continuously monitored the atmosphere by lunar, sun and star photometer in Ny-Ålesund.

	1991-1999	2013-2018
Winter	0.053 ± 0.030	0.0629 ± 0.0129
Dec + Jan	0.042 ± 0.021	0.0610 ± 0.0161
Feb	0.062 ± 0.034	0.0650 ± 0.0149

Table 9: Mean AOD_{500} for the years 1991-1999 (Herber et al., 2002) and 2013-2018 measured by the same star photometer in Ny-Ålesund.

Since the 1990s the mean AOD_{500} of the whole winter has increased by 18.7%, especially during December and January (45.2%) but simultaneously the variability has decreased by factor 2.

Looking at this mean values the aerosol concentration must have been changed within the observed time periods. The less the variability is the more homogeneously the aerosol is distributed. But a higher AOD also indicates either a higher aerosol load or larger particles. As in summer times there is a change of aerosol properties and load in the Arctic troposphere. Hence, having a continuous measurement series is a very important beginning of the investigation of the polar atmosphere and their changes.

4.5. Aerosol load during polar night

Compared with the sun photometer the star photometer has a more uniform distribution in the AOD_{500} for all measurement events as well as for monthly means (figure 30).

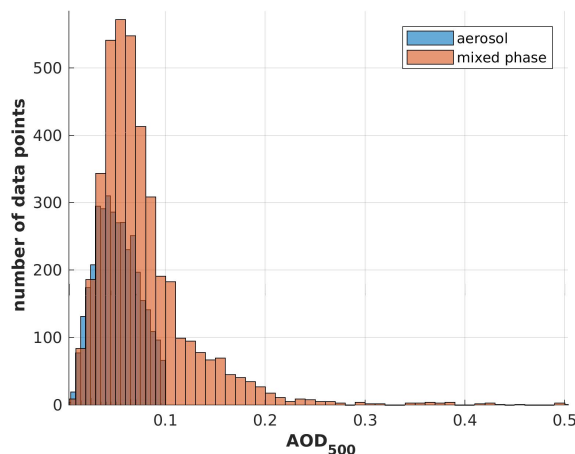


Figure 30: Histogram of the total AOD_{500}^{aer} (blue) and AOD_{500}^{mixed} (red) measured by the star photometer.

Both the measurement points flagged with "aerosol" (blue) and the data points flagged with "mixed phase" do not show a bi- or multi-modal distribution as it can be observed in sun photometer data. This result combined with those of chapter 4.1.2 lead to the conclusion that the aerosol in winter times has different physical and chemical properties from the one arriving in summer times.

4.6. Changes of heat transfer from mid latitudes

With ERA-Interim re-analysis data an average between 1000 and 800hPa from March to May of the years 1979 to 2015 for the parameters temperature (figure 31a), meridional wind component (figure 31b) and specific humidity (figure 31c) was calculated. Deviations in positive or negative direction of this mean are indicated by red and blue, respectively. As a reference value the AOD_{500} anomaly for Ny-Ålesund was also plotted using sun photometer data detected during the years 2001 to 2017.

4. Results

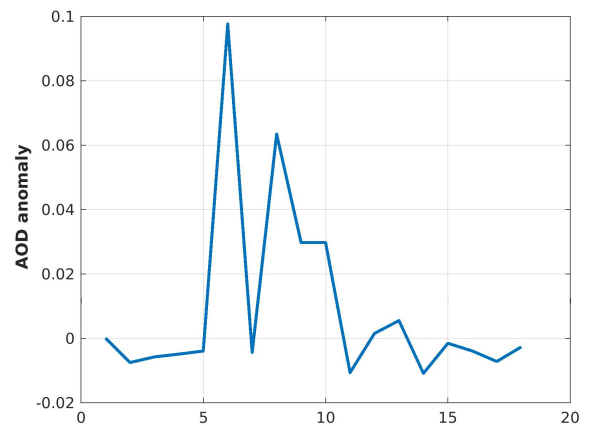
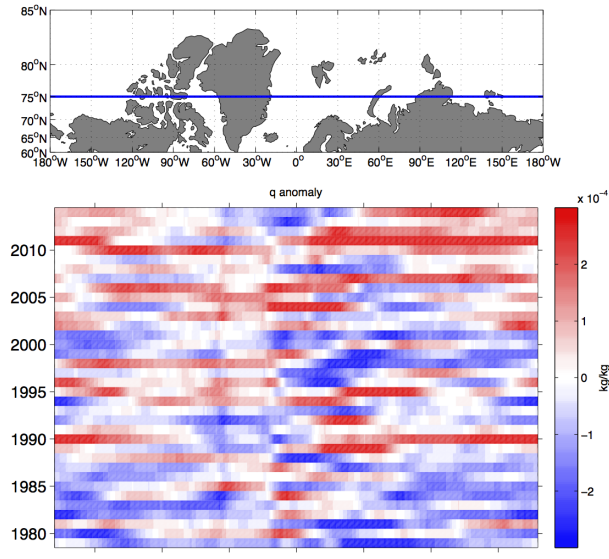
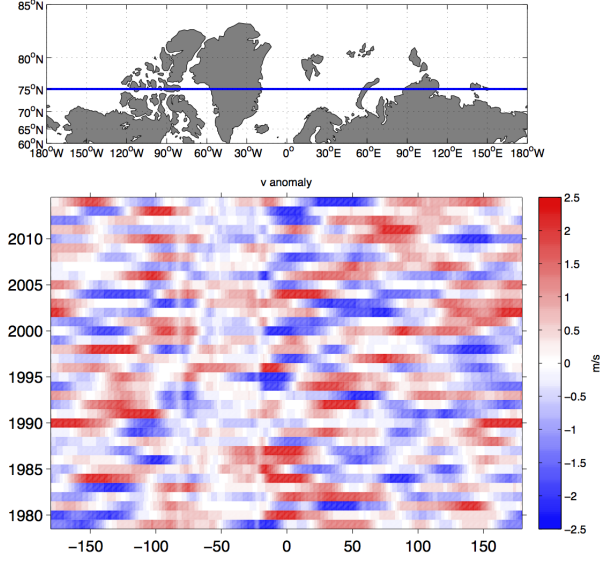
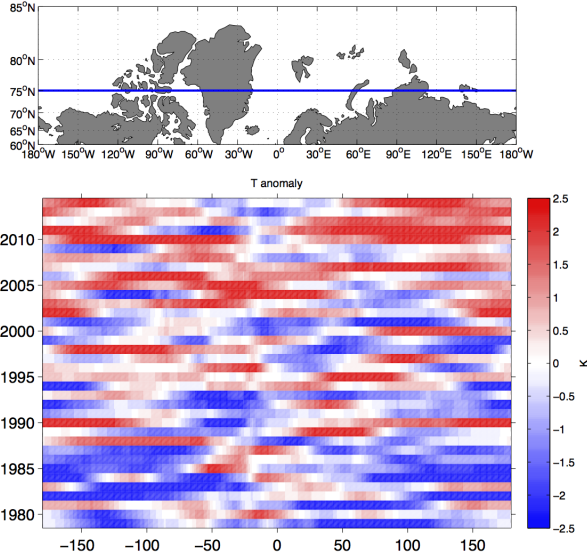


Figure 31: T, v and q anomalies at 75°N (blue line), indicating the changes of transported heat and specific humidity into higher latitudes. The AOD anomaly is done with the sun photometer in Ny-Ålesund for the years 2001-2017.

4. Results

To be able to compare these ERA-Interim re-analysis data with photometer measurements a mean of the same months of March to May of the Ångström exponent and AOD was taken for the years 2001 to 2014.

No correlation was found between T, q or v anomalies at 75°N and the measured AOD or Ångström exponent. To conclude, the atmosphere over the north European ocean does not explain the observations taken by photometers in Ny-Ålesund. Hence, either photometer aerosol measurements are too few and having a clear sky bias or the resolution of the model is too bad to resolve small- to large-scale motion of aerosols. Another reason for the poor result is the short life time of the particles so that they are not affected by the global circulation.

4.7. Aerosol load and properties

In the previous section monthly mean values of the AOD_{500} were shown to present the strong month to month variability and the small but distinct decrease of springtime AOD.

In this section one minute data is taken to look into more detail for some selected periods.

Figure 32 shows the histograms of AOD for April 2013 (figure 32a) and April 2017 (figure 32b). April 2013 is typical, as it shows a three-modal distribution: the AOD values may either be low, medium or high. This is typical for the Haze season and means that simple monthly averages, as e.g. published by Stock et al. (2014) are inappropriate. April 2017 is plotted as well because it is the only month of April between 2013 and 2017 when both the AOD and the modified Ångström exponent α are nicely log-normal distributed. Also given in figure 32a is the discrimination concerning the modified Ångström exponent α into values larger and smaller than $\alpha < -1.5$, indicating larger or smaller aerosol. In the segmentation in α , the origin of the multi-modal distribution of AOD is obvious as a superposition of small and large aerosol particles having a more or less negative Ångström exponent, respectively.

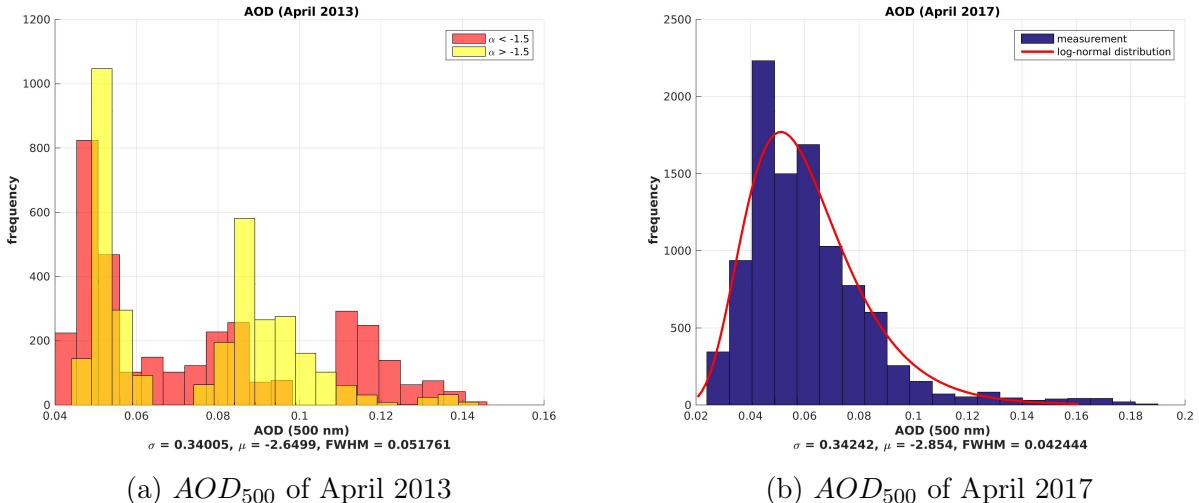
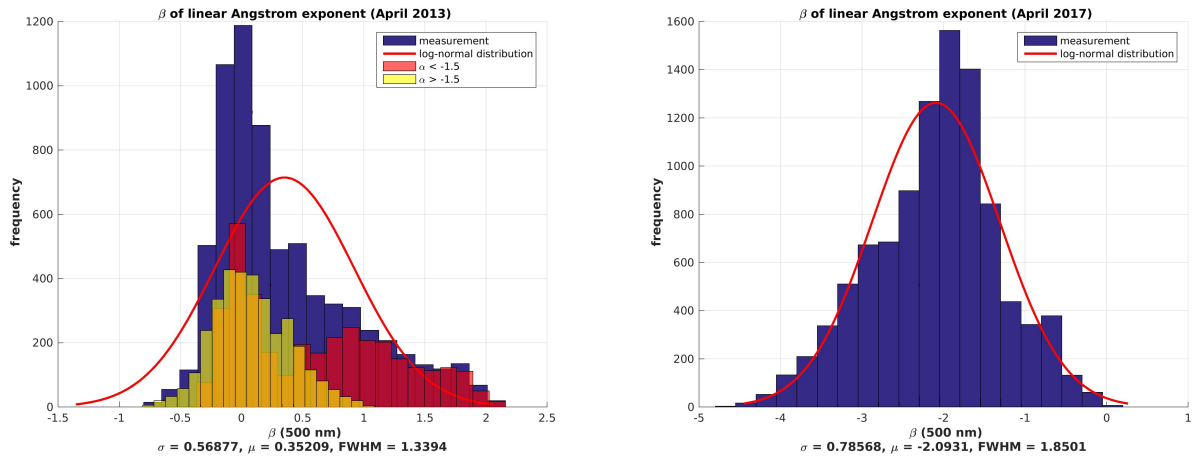


Figure 32: Distribution of 1-minute sun photometer data of AOD_{500} .

Interestingly, the value of the modified Ångström exponent α is in general closely related to its spectral slope β . This is shown in figures 33 and 34: The separation of all photometer data into α larger and smaller than -1.5 also distinguishes between almost negligible ($\beta \simeq 0$) and significant ($\beta > 1$) spectral slope. Due to the definition in equation 3.12. $\alpha < -0$ and $\alpha > 0$ means that in the UV a smaller, more negative effective Ångström exponent is retrieved than for the IR and particles scatter in this case more efficiently in IR than in UV.

The back-scatter cross-section strongly depends on the aerosol size. Hence, it is expected to find larger particles, $\alpha > -1.5$, with a high AOD and also smaller ones with a higher concentration. Due to the log-normal distributed AOD_{500} in April 2017 (figure 32b) also the spectral slope is distributed following a log-normal distribution (figure 33b).



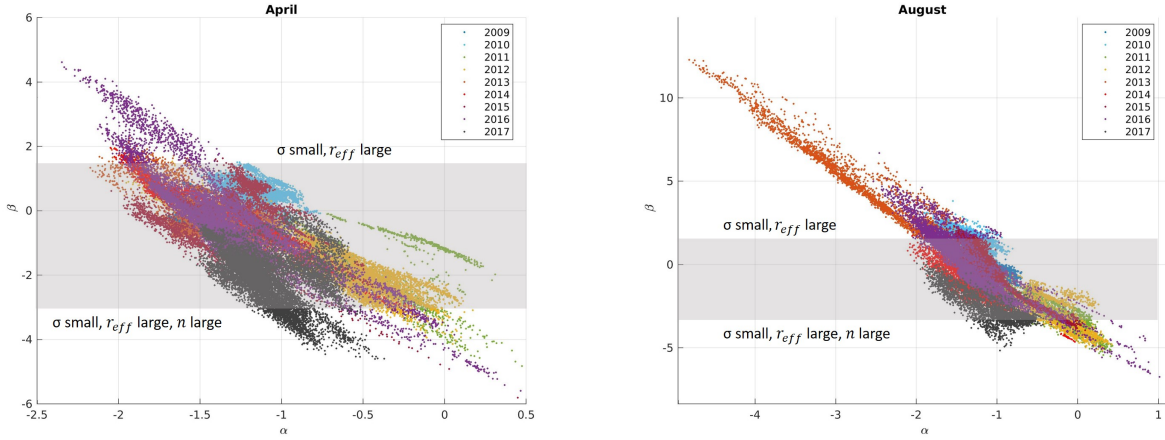
(a) Distribution of β depending on α of April 2013 (b) Distribution of β depending on α of April 2017

Figure 33: Histograms of the spectral slope α for (a) April 2013 and (b) April 2017. The yellow and red bars represent only the fraction of $\alpha > -1.5$ and $\alpha < -1.5$. The blue bars are the sum of both cases and, hence, the total number of measurements.

The generally nice correlation between the modified Ångström exponent α and its spectral slope β is also plotted in figure 34. The densest part of figure 34 remains at the same values for β , but slightly increases in β . However only a small range of α ($-2.5 < \alpha < 0.5$ and $-6 < \beta < 5$) is covered in April, the aerosol becomes less uniform in summer times ($-5 < \alpha < 2$ and $-6 < \beta < 13$). For April, inspection of figure 34 reveals that typical combinations of Arctic Haze are $\alpha \approx -1.5$ and $\beta \approx 0.75$ or $\alpha \approx -1$ and $\beta \approx -0.5$ or $\alpha \approx -0.5$ and $\beta \approx -2$.

According to figure 20 these values match better to the higher refractive index of $n = 1.60 + 10^{-2}i$, arbitrary distribution width, σ and effective radii around $r_{eff} = 0.1\mu m$, which is overall in fair agreement to the in-situ data at the site (Tunved et al., 2013) and hence supports the idea, that the measured aerosol on the ground are representative for the whole column. Contrary, for August the aerosol is more heterogeneously distributed. The large values for β can not be explained with only Mie theory and a monomodal log-normal distributions.

4. Results



(a) Correlation between the parameters α and β of the modified Ångström ansatz for all Aprils of the years 2009-2017.

(b) Correlation between the parameter α and β of the modified Ångström ansatz for all Augests of the years 2009-2017.

Figure 34: Correlation between the modified Ångström exponent α and its spectral slope β for the Arctic Haze season (April) and for summer conditions (August). The gray shaded area represents the values given by the two examples of the Mie calculus in section 3.3.

As it is expected in figures 24 and 26 the aerosol is more heterogeneously distributed in August than in April of the same years (figure 34). On the other hand the 30th and 70th percentile are narrower in August.

Therefore, the measured AOD over the years has about the same absolute value, but the composition changes from year to year. The aerosol arriving in Svalbard in April has approximately the same age and is chemically internal mixed. This stands in complete contrast to August when the aerosol has a lower age, is faster advected into the Arctic and chemical reactions are still ongoing in the particle and in total they are less homogeneous. Sources for this kind of aerosol can be biomass burning or marine bionic sulphur emission. In Lidar profiles such events are shown as individual layers. Whereas, the Arctic Haze in spring time appears as a constantly higher AOD over the whole part of the lower troposphere.

4.8. FLEXTTRA back-trajectories

With the aim of 5-days FLEXTTRA back-trajectories the origin and the path of air is analysed to answer the questions where the aerosol was released into the atmosphere and under which atmospheric conditions the air reached Ny-Ålesund five days later in 500, 1000 and 1500m height. There are some possibilities how to define trajectories. First, there are at least two groups depending on the value of the AOD when the air arrived in Ny-Ålesund. The threshold between "high" and "low" AOD is determined by sun photometer measurements. These two groups are separated afterwards into two parameters, "dry" and "moist" (see chapter 3.6).

The ocean, land and sea ice interact totally differently with aerosols, their origin and even with their sinks and are investigated using the fraction how much time the air stayed over which kind of ground. Because the aerosol is mainly produced on the ground or in the boundary layer the third way of obtaining information out of the model is by focusing on the time the air stayed in the boundary layer.

4.8.1. Aerosol origin due to arriving air pollution

In figure 35 all 14 trajectories are shown for April 2013 which end in 1500m altitude above Zeppelin station, Ny-Ålesund. The multi-modal AOD distributions were considered only showing back-trajectories with low or high AOD. The threshold is set for each month individually (see table 10).

Year	April	May	August
2013	0.07	0.04	0.035
2014	0.07	0.056	0.08
2015	0.085	0.09	0.07
2016	0.08	0.05	0.1
2017	-	0.08	0.035

Table 10: AOD threshold to distinguish back-trajectories arriving at Zeppelin station with high and low AOD

For both groups, high and low AOD, the air may come either from the Canadian or Russian Arctic. Overall the trajectory groups look quite similar. Both groups contain air masses, which had been in low altitudes above the ground of either the American or Eurasian continent. Moreover, precipitation (thick grey dots in figure 35) does not occur frequently in the ERA-Interim data set. Hence, one cannot simply assess one single pollution transport or favour one special source region where the Arctic Haze originates from. Note that in this sample there is no direct transport from Europe. In general the photometers can only measure during clear weather conditions and even thin clouds disturb the sensitive measurement. Due to the prevalent west-wind drift lots of moist air is transported from Europe, especially from Iceland, to Svalbard. Therefore, in photometer data there is always a bias in the data and northern Europe is under represented as the origin of precipitation bringing areas. Hence, aerosol from Europe may enter the Arctic mainly in interstitial form. Although the origin of inert trace gases arriving in Ny-Ålesund has already been proven (Eckhardt et al., 2003), it is still not possible for aerosols yet. When they enter clouds, they change their physical and chemical properties. Additionally, they are much more physically inert and do not follow the streamlines of wind fields precisely. For this reason they do not have exactly the same pollution pathways into the Arctic than trace gases and determine their origin with models becomes much more difficult. By now the resolution of these pathways is insufficiently resolved in the current meteorological fields of weather models.

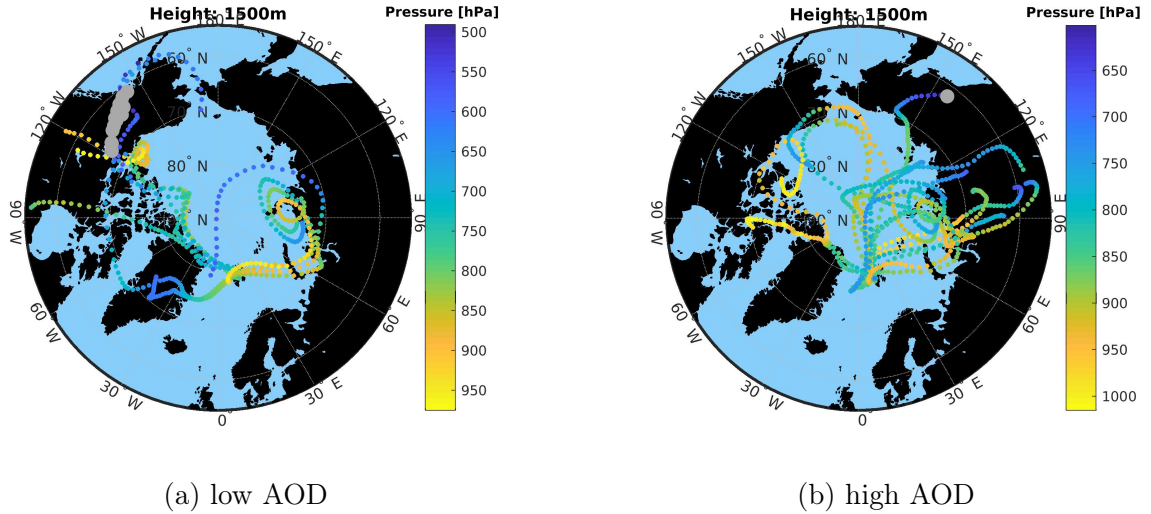


Figure 35: 5-days back-trajectories arriving in 1500m altitude over Ny-Ålesund for days with low AOD and high AOD in April 2013, respectively. Thick grey dots mark areas with a relative humidity $> 90\%$ as an indication for hygroscopic growth of the aerosol.

The plotted trajectories in figure 35 show only one example of high and low AOD a typical month and year. The other plots for April 2013-2016 and August 2013-2017 are presented in appendix A. Because no bimodal distribution in AOD_{500} was found in April 2017, no distinction in high and low AOD can be done. This year is omitted for trajectory analysis.

Similar to figure 35 trajectories for many more months inside and outside the Arctic Haze season have been calculated. In April 2013 the air came from Siberia as well as from North America and Greenland being dry and moist and reaching heights of up to 500hPa.

One can say that the origin of air with low AOD comes slightly more frequently from North America whereas air with high AOD has a higher probability to originate in Siberia. But in both cases there are also lots of trajectories coming from the other continent before reaching Svalbard. Hence, any clear source region of the aerosol was not found.

Also the pattern of each chosen height looks similar. Hence, the dependency of the chosen height is not the most important point of interpretation of back-trajectories. Maybe the biggest problem is the resolution of the wind fields, especially in high latitudes.

Contrary to the approach and data set Christensen et al. (1997) and Udisti et al. (2016) employed a chemical analysis of aerosol in-situ measurements from Ny-Ålesund to perform a source apportionment for the important sulphate component of Arctic Haze. They found a clear anthropogenic origin for data from April and more marine aerosol during summer. Clearly, looking for markers in in-situ samples is the best way to prove the origin of Arctic aerosol. However, its pollution pathway and life-time in the atmosphere remains as an open question.

4.8.2. Aerosol sources and sinks

As the back-trajectory analysis do not show any convincing source region of Arctic Haze the following hypothesis is tested: Does the time, the air parcel spends over sea ice, free ocean or land, have an impact on low and accordingly high AOD in Ny-Ålesund? Does the measured AOD depend more on the effective sinks instead of the sources?

The albedo of sea ice and snow covered land is very high and heating of the ground by the sun is very inefficient. Hence, the atmosphere is thermodynamically stably stratified and the boundary layer is thin. So it is expected having less vertical mixing, a dry boundary layer and therefore a longer aerosol life-time compared to air masses being advected over the open ocean. Due to this initial condition aerosol sinks are turned off over ice and the aerosol can only be transported not removed. This idea is checked by the fraction of time the air parcel stayed over land, sea ice or open ocean and it was plotted in the month of April 2013 to exemplify it (see figure 35). Also the cases "dry" and "moist" air were distinguished using relative humidity $> 90\%$ for at least 6h as a limit and divided between arrival altitudes at 500m, 1000m and 1500m over Zeppelin station, Ny-Ålesund. As it is known from Lidar observations, the Arctic Haze phenomenon usually occurs in the lower troposphere (Tomasi et al., 2015; Ritter et al., 2016). The number of measurements for the so-called "moist" case is much less than for "dry" either because the aerosol advection intrinsically occurs in dry air or because of the clear air bias in the instrument.

Hence, as an interim result the impact of possible aerosol sinks of classical air back-trajectory analysis has not been considered carefully and so in agreement to Christensen et al. (1997) and Tunved et al. (2013) aerosol of marine origin can be neglected for optical measurements in the Haze season. Cases of moist air below 1000m altitude drastically reduce the number of available photometer measurements. This is in agreement to Maturilli and Ebelt (2018), who derived from ceilometer observations that the cloud bottom at Ny-Ålesund is generally below 1000m altitude and from this follows that aerosol above 1000m altitude may survive cloud formation and is not being washed out.

Due to the annual changes of sea ice extend the fraction of sea ice in August is always smaller than in April and May, vice versa for the fraction of the ocean (figure 36).

The fraction of sea ice is much higher (up to 42%) for the "low" cases. On the other hand "ocean" has only a fraction of 22% for the case "high, dry", which is the smallest of all categories (figure 36a). This indicates that the sinks are important. Whereas the boundary layer is stably stratified over the sea ice and the efficiency of sinks is reduced, the probability of cloud formation is much more likely over a convective boundary layer over the ocean with moist conditions.

Due to the stronger solar irradiance in later months local, sun driven processes become more important than large-scale atmospheric patterns (Lüpkes et al., 2008; Pozzoli et al., 2017). As in summer the polar vortex is much weaker than during polar night, much more diverse aerosol can be advected from mid-latitudes into the Arctic. In addition to that aerosols pro-

4. Results

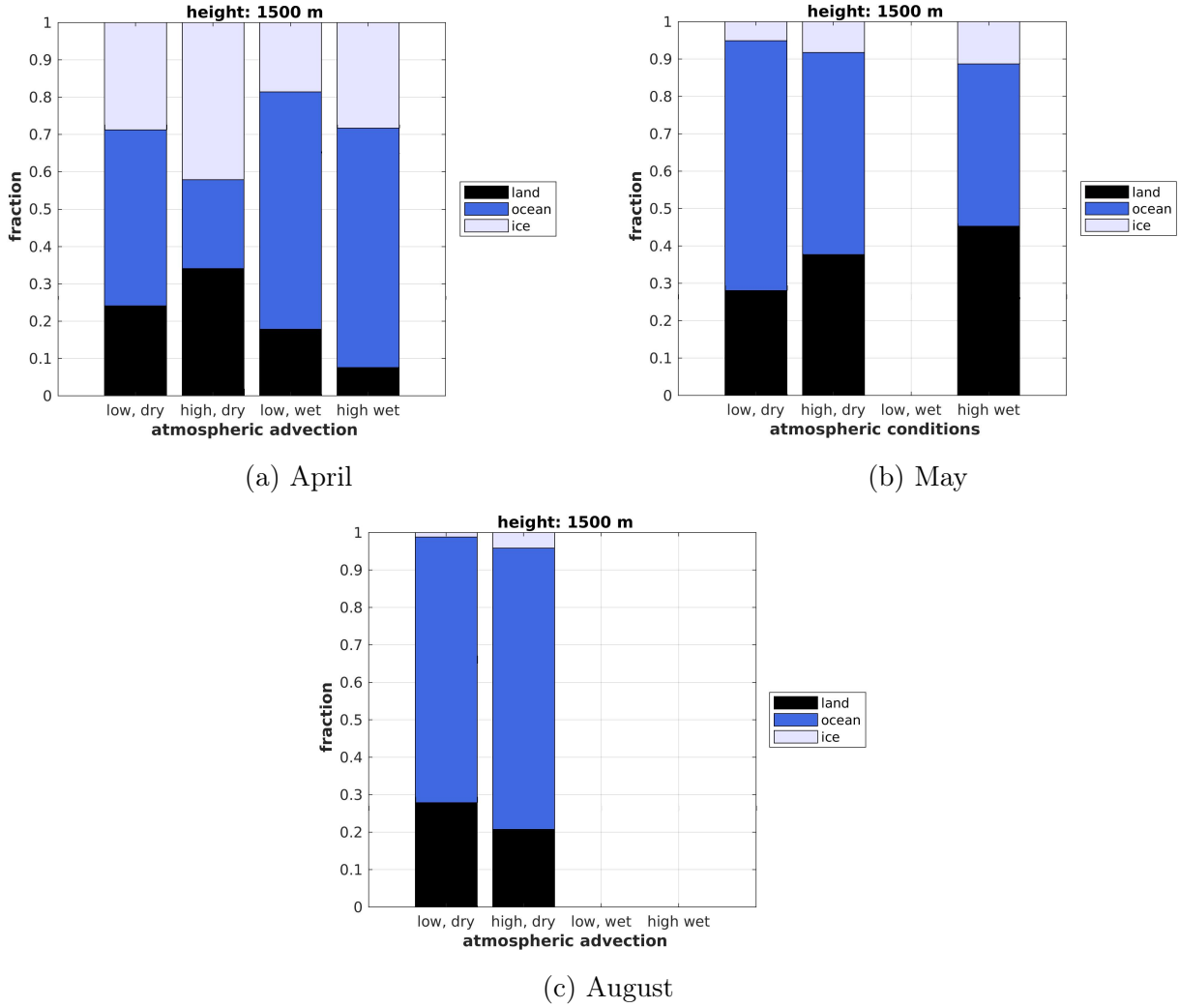


Figure 36: Fraction how long the air parcel was over land, ocean or ice for the months April, May and August and arrived in a height of 1500m over Ny-Ålesund for the years 2013-2017.

duced by plants arise more numerously during polar day. This means the aerosol is much more diverse in August than in spring, which can be seen in the thresholds between the regimes of high and low AOD (see table 10) and the larger range in α and β in figure 34. This inter-annual change of variability can also be found in the modified Ångström exponents α and β .

Due to a higher probability of wet deposition in summer than in winter the mean life-time of aerosol is much shorter. Therefore, the results of the model should be more reliable in summer than in winter times.

A tendency of the fraction can be seen: the longer the air has been over ice and land, the higher the AOD is. The sea ice reduces the efficiency of sinks whereas most of the aerosol is released over land in the presence of plants, humans and soil.

4.8.3. Remarks on the advection altitude

A clear difference can be seen in figure 37 for each height and type of ground (land, open ocean or sea ice). Zeppelin Station is located close to Kongsfjord and has a direct access to the ocean. The left plots of figures 37 and 38 represent all data independent of the height the air was on the way to Zeppelin Station whereas the plot on the right only shows the property of the ground when the air was below the 900hPa pressure level and is called "boundary layer" in the following discussion.

Air parcels arriving in 500m above the station are easily influenced by the local boundary layer, or even being still part of it. Whereas the sea ice content of the Arctic is close to its maximum in April the air itself has a good chance to flow ground-near over it. Due to friction the wind speed in the boundary layer is smaller than in the free troposphere above, which means, the air can not flow such long distances within the five days of the calculated back-trajectories. Therefore, the differences between low and high AOD for the "dry" case are quite small. Hence, the presence of cloud condensation and its formation is very crucial because aerosol can be washed out. This means, the air itself spends the most time in the lowermost 100hPa level. For the "wet" case the pattern looks very different given that the number of calculated points is too small to make a profound conclusion about physical properties of the trajectory. In general the air arriving in the lowermost layer of the atmosphere has, compared to the other heights, the largest probability to get more aerosol when flowing over land whereas, especially in winter, the sinks are reduced due to snow and ice cover of ocean and land.

Air parcels being close to the ground and over continents have to travel a long distance in only five days to reach Spitsbergen. Therefore, the air has to ascent and reach the free troposphere with higher wind speeds. This air mostly remains in higher altitude and arrives in the height of in 1500m over Zeppelin Station. With the influence of the orography of the surrounding continents the air reaches the needed height. But these possibilities are not available over sea ice, why this fraction is the smallest. In long-term ceilometer data over Ny-Ålesund a mean cloud height of about 1km was found (Maturilli and Ebelt, 2018). Therefore clouds usually lie below the arrival height of the trajectories. Hence, there is a lack of aerosol sink in this height. Because the continents are far away from Spitsbergen, the air has to rise into the free troposphere, where the wind speed is much higher than closer to the ground, in order to reach the archipelago. For these trajectories the sources are more important than the sinks, especially when the air was in the boundary layer and rose afterwards to the arrival height of 1500m .

Trajectories arriving in 1000m height are the connection between long-range transport and boundary layer influences. While the fraction of "land" is increasing a bit, the fraction of "sea ice" is still very dominant. Because of having only one point the case "low, wet" is ignored in the following discussion.

4. Results

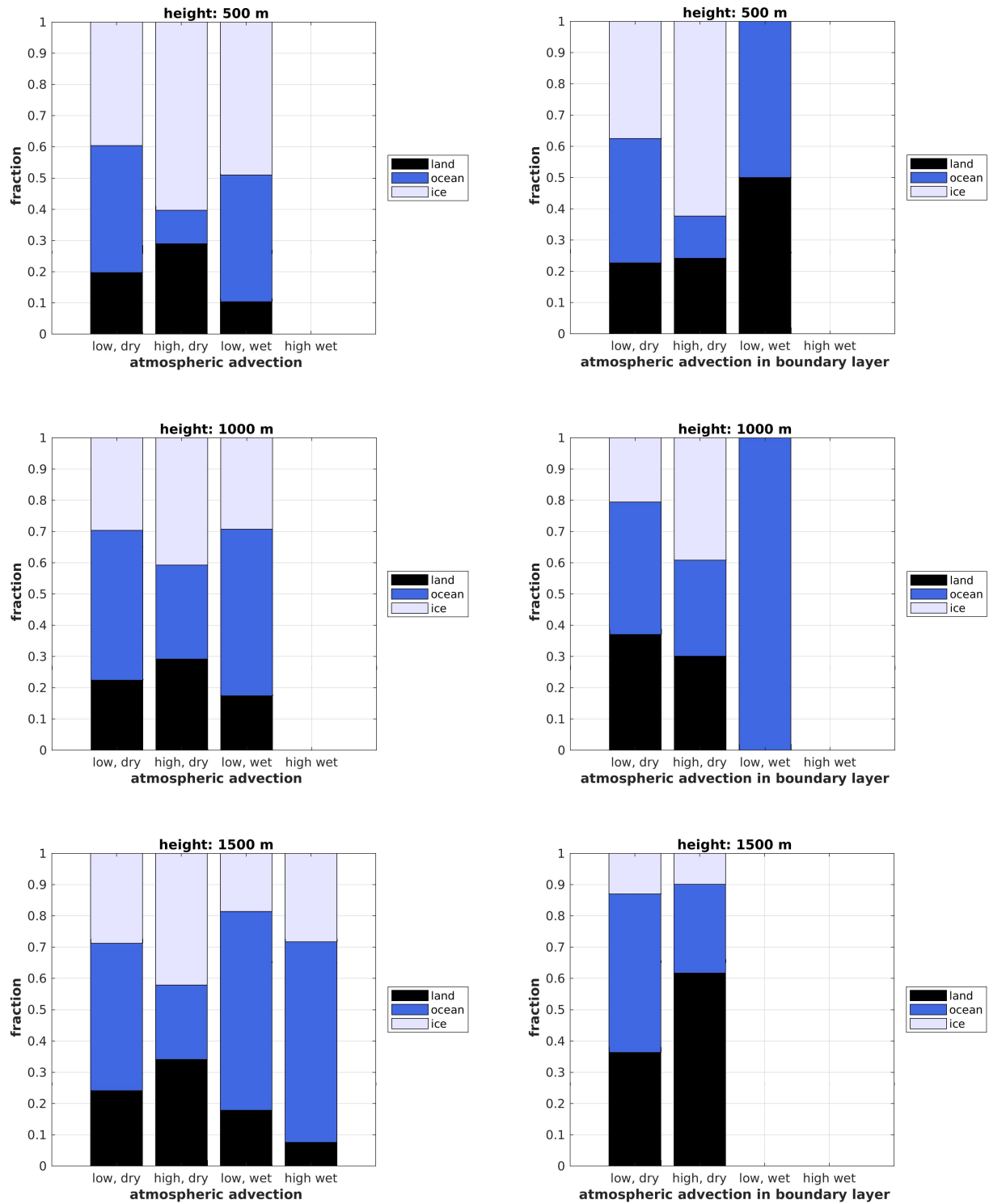


Figure 37: Fraction how long the air parcel was over land, ocean or ice.

Left: All data points are plotted, independent of the height of the air parcel.

Right: Only the cases are plotted where the air parcel was within the boundary layer defined by the pressure level of 900hPa. This plot only shows the data for the arriving heights 500, 1000 and 1500m above Zeppelin Station for all Aprils 2013-2016.

4. Results

In August (figure 38) the situation looks quite the same as in April with the major difference that due to the annual minimum the sea ice concentration is very low and even a concentration of 95% is reached for only a few cases.

As for the cases in April the fraction of land arises with the arriving altitude of the air parcel while the fraction of the ocean is decreasing at the same time.

The threshold for the cases "high AOD" and "low AOD" changes dramatically over the years in August. In the statistical mean this variability reduces simultaneously the variability in the fractions and the interpretation of these diagrams does not represent the actual atmospheric situation anymore.

Some of the trajectories fulfill both criteria of low and high AOD because during the 2h of photometer measurement the AOD changed. Therefore, it is necessary for a clear estimation of the aerosol origin and the reason for such a fast AOD change to have at least the trajectories for each 1h.

To get a better estimation of the error, back- and forward-trajectories have to be considered. Whereas back-trajectories have one exact starting point, forward-trajectories should be set into a grid around the position where the back-trajectories end. In case the model has a sufficient resolution the forward-trajectories will end at approximately the same area as the ones which were back computed.

Another reason for the insufficient result of the model can be the aerosol life time. During winter times most of the ground in high latitudes is covered by snow and ice. The snow prevents a dry deposition and the aerosols can stay up to 15-days in the atmosphere before they are sedimented. But for this long time the uncertainties of the model are way too large to gain information out of this approach.

4. Results

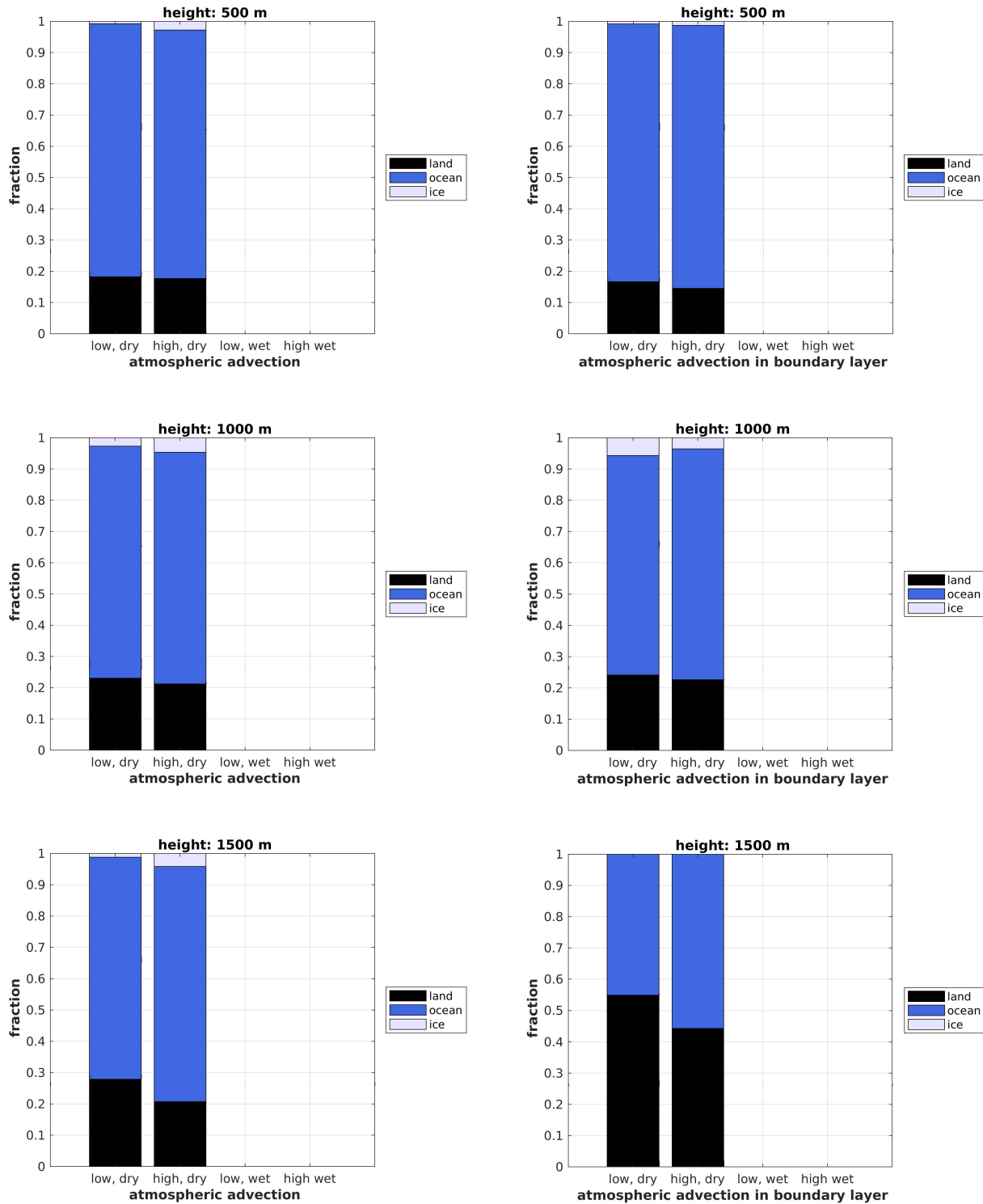


Figure 38: Fraction how long the air parcel was over land, ocean or ice.

Left: All data points are plotted, independent of the height of the air parcel.

Right: Only the cases are plotted where the air parcel was within the boundary layer defined by the pressure level of 900hPa. This plot only shows the data for the arriving heights 500, 1000 and 1500m above Zeppelin Station for all Augests 2013-2017.

5. Conclusion

In this thesis an improvement of the fitting ansatz is presented taking the first order correction term of the Taylor extension of the Ångström exponent. The new ansatz now is wavelength dependent. Additionally, the modified Ångström exponents α and β and their value for observing the Arctic aerosol are also discussed. Furthermore, an error analysis with the Mie code of libRadtran was performed to analyse the information content of this new approach.

It is found that α and β are anti-correlated which means larger particles have a smaller spectral slope.

Within the measurement data starting from 2001 to 2017 a declining trend in AOD of the Arctic Haze during the spring months of March and April was found with a simultaneously strong year-on-year variability. For every month the minute-by-minute data normally show a bi- or even multi-modal distribution of the AOD.

Whereas the AOD is slightly declining in spring months it also increases in autumn in the same time which makes the annual cycle of AOD more and more flat.

The star photometer closes the gap of the sun photometer during polar night. Contrary to the polar day the AOD is log-normal distributed. Through the whole winter the AOD increases continuously while the modified Ångström exponent α is remaining constant. Hence, the extinction properties of the aerosol does not change significantly by the month. Particularly, it seems that aerosol becomes more uniform during winter.

No evident origin was found for high or low polluted air arriving in Ny-Ålesund using FLEX-TRA 5-days back-trajectories. Because of the prevalent west-wind drift in the Arctic most of the precipitating advecting air masses have not been recorded by the photometers. Besides the aerosol pathway through the atmosphere is an open question but needs to be solved for optimising weather models. Even the life time of aerosols is not understood completely.

An indication was found that sea ice, which acts as the reduction of aerosol sinks, controls the AOD in the European Arctic during spring. The decline of Arctic Haze can probably be related to more aerosol sinks, for example caused by the shrinking ice cover.

When using back-trajectories sinks and sources are equally important to consider. So in case the arriving air carries a high amount of pollution and is not washed out by precipitation the air can be either advected over sea ice or arrives in an altitude above 1000m, which is over the average height of polar clouds.

6. Outlook

Despite of the results of this thesis there are still many unanswered questions concerning the annual changes of Arctic aerosol in Svalbard. Especially during the season of the Arctic Haze in spring the small-scale variations are yet unknown. In future times a sun photometer can be installed on a snow mobile and then driven along the shore of the Kongsfjord on very stably stratified days. With the assumption that the aerosol does not change in time one can get the local variabilities. This can be done with this method because the photometer has quite a fast temporal resolution and the instrument itself is portable. This can only be realised when the sun is already shining and there is still enough snow to drive on.

Another possibility to observe the changes in properties of the aerosol would be a comparison with Station Nord, a military base in northern Greenland. Especially the west coast of Svalbard is highly affected by the Gulf stream bringing warm water into the high Arctic. Station Nord would be on the cold side of the Fram street, the sea between Svalbard and Greenland.

In long-term observations a significant increase of precipitation and cloud formation was found (Førland and Hanssen-Bauer, 2000). To include the water vapor related wavelengths of the photometers a calibration and comparison of the measurement of relative humidity by radiosondes could be done. As a consequence, the problem of wet aerosol and already early cloud formation can get smaller and the cloud screening can be improved.

Due to an increase of solid and liquid precipitation, wet aerosol deposition takes place more often. Another open question is if there is a correlation between the decreasing mean AOD, especially in spring and an increasing amount of precipitation. To answer this question the fact of a big bias of clear weather conditions of the instrument has to be taken into account.

In this thesis the star photometer was only used to fill the gap in polar night. For this purpose a new cloud screening algorithm was introduced. Already at first appearance the winter atmosphere has total different physical properties. Further investigation of the winter atmosphere has to be done in future times. But additionally a calibration of the instrument is needed. For already recorded data the measurement values shall be re-calculated with new gauge files of the corresponding year. This data can also be compared with aerosol in-situ instruments operating on tethered balloons.

Assuming the errors of calibrating a sun photometer are lower than for the star photometer, the sun photometer can be used for reducing the calibration errors of the star photometer. When during spring and autumn star and sun photometer measurements are possible at the same time and the days are clear, both instruments should detect the same AOD. With the reduction of the off-set the instruments are comparable. The Lidar KARL can be used to monitor the conditions between sun and star photometer.

Also the cloud screening algorithm of the star photometer can be used at other sites and might be compared with the algorithm other ones use. One major problem is the absence of pictures by all-sky cameras to have a manual check. But even with this additional help early cloud formation can not be identified by investigators.

Depending on the actual position of the polar vortex Ny-Ålesund can be inside or outside of the ozone hole. Therefore, having a correct value for the total ozone content of an atmospheric column is very crucial. To improve the ozone optical depth measurements within the Huggins and Hardley band should be done.

The recently presented ansatz with the modified Ångström exponent should be applied to other Arctic and sub-Arctic stations. Because only a few sites with a limited number of instruments in the Arctic perform atmospheric measurements it is very important to get as much information as possible out of the few data sets.

In libRadtran the software package OPAC (Optical Properties of Aerosol and Clouds) is included. It is based on a dataset of microphysical and optical properties, for example the extinction, scattering and absorption coefficients, the single scattering albedo, the asymmetry parameter, and the phase function of six water clouds, three ice clouds and ten aerosol components. With these different types the software package provides the interaction of solar and terrestrial radiation with these 19 different atmospheric constituents.

With the so defined known atmospheric different layers a parameter set of α and β with various refractive indices and size distribution parameters can be presented as a handbook for rough estimations of observation data.

Additionally, libRadtran can be used for bi-modal aerosol distributions using coarse and fine mode aerosol for different shapes of size distributions and refractive indices.

For a better understanding of the pollution pathways better longer back-trajectories of minimum seven days should be used which should be improved by special campaigns like the international Arctic drift expedition MOSAiC (Mulitdisciplinary drifting Observatory for the Study of Arctic Climate) beginning in September 2019 or matching campaigns, for example ARCROSE (Arctic Research Collaboration for Radiosonde Observing System Experiment) or YOPP (Year Of Polar Prediction).

In this thesis it was shown that 5-day back-trajectories do not present an area where most of the polluted air comes from. This result can be caused by the fact of the absence of a specific polluting area or way too large errors due to grid size. Furthermore, the missing of observation data especially in polar regions for re-analysis data can be a reason as well.

Svalbard itself has a very variable orography with lots of fjords and mountains in which the micrometeorology dominates the large-scale weather patterns. Starting back-trajectories on Svalbard the error after only a few computational steps is already very large. So the model provides a completely wrong final point where the air parcel was situated five days ago. To solve this problem a much better high resolved global model is required also having aerosols included.

References

- B. A. Albrecht. Aerosols, cloud microphysics, and fractional cloudiness. *Science*, 245(4923):1227–1230, 1989.
- M. D. Alexandrov, A. Marshak, B. Cairns, A. A. Lacis, and B. E. Carlson. Automated cloud screening algorithm for mfrsr data. *Geophysical research letters*, 31(4), 2004.
- A. Ångström. On the atmospheric transmission of sun radiation and on dust in the air. *Geografiska Annaler*, 11(2):156–166, 1929.
- A. Ångström. Techniques of determinig the turbidity of the atmosphere. *Tellus*, 13(2):214–223, 1961.
- A. Ångström. The parameters of atmospheric turbidity. *Tellus*, 16(1):64–75, 1964.
- P. Buseck and S. Schwartz. Tropospheric aerosols. *Treatise on geochemistry*, 4:347, 2003.
- J. Christensen, M. Goodsite, N. Heidam, H. Skov, and P. Wåhlin. Chapter 1. *Atmospheric Environment*. In: Riget, F., J. Christensen and P. Johansen (Editors). *AMAP Greenland and the Faroe Islands*, 2001:11–46, 1997.
- J. A. Curry, J. L. Schramm, W. B. Rossow, and D. Randall. Overview of arctic cloud and radiation characteristics. *Journal of Climate*, 9(8):1731–1764, 1996.
- S. Eckhardt, A. Stohl, S. Beirle, N. Spichtinger, P. James, C. Forster, C. Junker, T. Wagner, U. Platt, and S. Jennings. The north atlantic oscillation controls air pollution transport to the arctic. *Atmospheric Chemistry and Physics*, 3(5):1769–1778, 2003.
- A.-C. Engvall, R. Krejci, J. Ström, R. Treffeisen, R. Scheele, O. Hermansen, and J. Paatero. Changes in aerosol properties during spring-summer period in the arctic troposphere. *Atmospheric chemistry and physics*, 8(3):445–462, 2008.
- E. J. Førland and I. Hanssen-Bauer. Increased precipitation in the norwegian arctic: true or false? *Climatic Change*, 46(4):485–509, 2000.
- J. Haywood and O. Boucher. Estimates of the direct and indirect radiative forcing due to tropospheric aerosols: A review. *Reviews of geophysics*, 38(4):513–543, 2000.
- H. Hegner, G. Müller, V. Nespor, A. Ohmura, R. Steigard, and H. Gilgen. World climate research program wcrp (wmo/icsu/ioc)-baseline surface radiation network (bsrn)-update of the technical plan for bsrn data management-world radiation monitoring center (wrmc)-technical report 2, version 1.0. 1998.
- A. Herber, L. W. Thomason, H. Gernandt, U. Leiterer, D. Nagel, K.-H. Schulz, J. Kaptur, T. Albrecht, and J. Notholt. Continuous day and night aerosol optical depth observations in the arctic between 1991 and 1999. *Journal of Geophysical Research: Atmospheres*, 107(D10), 2002.

- A. Hoffmann. *Comparative aerosol studies based on multi-wavelength Raman LIDAR at Ny-Ålesund, Spitsbergen*. PhD thesis, Universität Potsdam, 2011.
- C. E. Junge. Air chemistry and radioactivity. In *International Geophysics Series*, volume 4. academic press, 1963.
- F. Kasten. A new table and approximation formula for the relative optial air mass. *Archiv für Meteorologie, Geophysik und Bioklimatologie, Serie B*, 14(2):206–223, 1965.
- F. Kasten and A. T. Young. Revised optical air mass tables and approximation formula. *Applied optics*, 28(22):4735–4738, 1989.
- A. Kautzleben. *Optically thin clouds over Ny-Ålesund: Dependence on meteorological parameters and effect on the surface radiation budget*. PhD thesis, Universität Potsdam, 2017.
- A. Kreuter, S. Wuttke, and M. Blumthaler. Improving langley calibrations by reducing diurnal variations of aerosol ångström parameters. *Atmospheric Measurement Techniques*, 6(1):99–103, 2013.
- C. Lüpkes, T. Vihma, G. Birnbaum, and U. Wacker. Influence of leads in sea ice on the temperature of the atmospheric boundary layer during polar night. *Geophysical Research Letters*, 35(3), 2008.
- K. M. Markowicz, P. Pakszys, C. Ritter, T. Zielinski, R. Udisti, D. Cappelletti, M. Mazzola, M. Shiobara, P. Xian, O. Zawadzka, et al. Impact of north american intense fires on aerosol optical properties measured over the european arctic in july 2015. *Journal of Geophysical Research: Atmospheres*, 121(24), 2016.
- M. Maturilli and K. Eboll. Twenty-five years of cloud base height measurements by ceilometer in ny-ålesund, svalbard. *Earth System Science Data*, 10(3):1451–1456, 2018.
- M. Maturilli and M. Kayser. Arctic warming, moisture increase and circulation changes observed in the ny-ålesund homogenized radiosonde record. *Theoretical and Applied Climatology*, 130(1-2):1–17, 2017.
- M. Maturilli, R. Neuber, P. Massoli, F. Cairo, A. Adriani, M. Moriconi, and G. D. Donfrancesco. Differences in arctic and antarctic psc occurrence as observed by lidar in ny-ålesund (79 n, 12 e) and mcmurdo (78 s, 167 e). *Atmospheric chemistry and physics*, 5(8):2081–2090, 2005.
- G. Mie. Beiträge zur optik trüber medien, speziell kolloidaler metallösungen. *Annalen der physik*, 330(3):377–445, 1908.
- N. O'Neill, T. Eck, B. Holben, A. Smirnov, O. Dubovik, and A. Royer. Bimodal size distribution influences on the variation of angstrom derivatives in spectral and optical depth space. *Journal of Geophysical Research: Atmospheres*, 106(D9):9787–9806, 2001a.
- N. O'Neill, T. Eck, A. Smirnov, B. Holben, and S. Thulasiraman. Spectral discrimination of coarse and fine mode optical depth. *Journal of Geophysical Research: Atmospheres*, 108 (D17), 2003.

- N. T. O'Neill, O. Dubovik, and T. F. Eck. Modified ångström exponent for the characterization of submicrometer aerosols. *Applied Optics*, 40(15):2368–2375, 2001b.
- K.-T. Park, S. Jang, K. Lee, Y. J. Yoon, M.-S. Kim, K. Park, H.-J. Cho, J.-H. Kang, R. Udisti, B.-Y. Lee, et al. Observational evidence for the formation of dms-derived aerosols during arctic phytoplankton blooms. *Atmospheric Chemistry and Physics*, 17(15):9665–9675, 2017.
- D. Pérez-Ramírez, H. Lyamani, F. Olmo, D. Whiteman, F. Navas-Guzmán, and L. Alados-Arboledas. Cloud screening and quality control algorithm for star photometer data: assessment with lidar measurements and with all-sky images. *Atmospheric Measurement Techniques*, 5(7):1585–1599, 2012.
- R. Pincus and M. B. Baker. Effect of precipitation on the albedo susceptibility of clouds in the marine boundary layer. *Nature*, 372(6503):250, 1994.
- F. Pithan and T. Mauritsen. Arctic amplification dominated by temperature feedbacks in contemporary climate models. *Nature Geoscience*, 7(3):181, 2014.
- L. Pozzoli, S. Dobricic, S. Russo, and E. Vignati. Impacts of large-scale atmospheric circulation changes in winter on black carbon transport and deposition to the arctic. *Atmospheric Chemistry and Physics*, 17(19):11803, 2017.
- P. Quinn, G. Shaw, E. Andrews, E. Dutton, T. Ruoho-Airola, and S. Gong. Arctic haze: current trends and knowledge gaps. *Tellus B: Chemical and Physical Meteorology*, 59(1):99–114, 2007.
- C. Ritter, R. Neuber, A. Schulz, K. Markowicz, I. Stachlewska, J. Lisok, P. Makuch, P. Pakszys, P. Markuszewski, A. Rozwadowska, T. Petelski, T. Zielinski, S. Becagli, R. Traversi, R. Udisti, and M. Gausa. 2014 iarea campaign on aerosol in spitsbergen ? part 2: Optical properties from raman-lidar and in-situ observations at ny-ålesund. *Atmospheric Environment*, 141: 1–19, 2016. doi: 10.1016/j.atmosenv.2016.05.053. URL <http://dx.doi.org/10.1016/j.atmosenv.2016.05.053>.
- A. Rozwadowska, T. Zieliński, T. Petelski, and P. Sobolewski. Cluster analysis of the impact of air back-trajectories on aerosol optical properties at hornsund, spitsbergen. *Atmospheric Chemistry and Physics*, 10(3):877–893, 2010.
- M. Sand, B. H. Samset, Y. Balkanski, S. Bauer, N. Bellouin, T. K. Berntsen, H. Bian, M. Chin, T. Diehl, R. Easter, S. J. Ghan, T. Iversen, A. Kirkevåg, J.-F. Lamarque, G. Lin, X. Liu, G. Luo, G. Myhre, T. V. Noije, J. E. Penner, M. Schulz, Ø. Seland, R. B. Skeie, P. Stier, T. Takemura, K. Tsigaridis, F. Yu, K. Zhang, and H. Zhang. Aerosols at the poles: an aerocom phase ii multi-model evaluation. *Atmospheric Chemistry and Physics*, 17(19):12197–12218, 2017. doi: 10.5194/acp-17-12197-2017. URL <https://www.atmos-chem-phys.net/17/12197/2017/>.
- G. E. Shaw. The arctic haze phenomenon. *Bulletin of the American Meteorological Society*, 76(12):2403–2414, 1995.

- T. Shibata, K. Shiraishi, M. Shiobara, S. Iwasaki, and T. Takano. Seasonal variations in high arctic free tropospheric aerosols over ny-ålesund, svalbard, observed by ground-based lidar. *Journal of Geophysical Research: Atmospheres*, 123(21):12–353, 2018.
- K. P. Shine and P. M. de F Forster. The effect of human activity on radiative forcing of climate change: a review of recent developments. *Global and Planetary Change*, 20(4):205–225, 1999.
- M. Stock. *Charakterisierung der troposphärischen Aerosolvariabilität in der europäischen Arktis [Characterization of tropospheric aerosol variability in the European Arctic]*. PhD thesis, PhD thesis, University of Potsdam and Alfred Wegener Institute, Helmholtz ?, 2010.
- M. Stock, C. Ritter, V. Aaltonen, W. Aas, D. Handorf, A. Herber, R. Treffeisen, and K. Dethloff. Where does the optically detectable aerosol in the european arctic come from? *Tellus B: Chemical and Physical Meteorology*, 66(1):21450, 2014.
- A. Stohl and P. Seibert. On the accuracy of different types of trajectories. *WIT Transactions on Ecology and the Environment*, 21, 1997.
- A. Stohl, T. Berg, J. Burkhart, A. Fj?raa, C. Forster, A. Herber, Ø. Hov, C. Lunder, W. McMillan, S. Oltmans, et al. Arctic smoke—record high air pollution levels in the european arctic due to agricultural fires in eastern europe in spring 2006. *Atmospheric Chemistry and Physics*, 7 (2):511–534, 2007.
- I. Tang, H. Munkelwitz, and J. Davis. Aerosol growth studies?iv. phase transformation of mixed salt aerosols in a moist atmosphere. *Journal of Aerosol Science*, 9(6):505–511, 1978.
- C. Toledano, V. Cachorro, M. Gausa, K. Stebel, V. Aaltonen, A. Berjón, J. O. de Galisteo, A. De Frutos, Y. Bennouna, S. Blindheim, et al. Overview of sun photometer measurements of aerosol properties in scandinavia and svalbard. *Atmospheric environment*, 52:18–28, 2012.
- C. Tomasi, V. Vitale, A. Lupi, C. Di Carmine, M. Campanelli, A. Herber, R. Treffeisen, R. Stone, E. Andrews, S. Sharma, et al. Aerosols in polar regions: A historical overview based on optical depth and in situ observations. *Journal of Geophysical Research: Atmospheres*, 112(D16), 2007.
- C. Tomasi, A. A. Kokhanovsky, A. Lupi, C. Ritter, A. Smirnov, N. T. O'Neill, R. S. Stone, B. N. Holben, S. Nyeki, C. Wehrli, et al. Aerosol remote sensing in polar regions. *Earth-Science Reviews*, 140:108–157, 2015.
- P. Tunved, J. Ström, and R. Krejci. Arctic aerosol life cycle: linking aerosol size distributions observed between 2000 and 2010 with air mass transport and precipitation at zeppelin station, ny-ålesund, svalbard. *Atmospheric Chemistry and Physics*, 13(7):3643–3660, 2013.
- S. Twomey. Pollution and the planetary albedo. *Atmospheric Environment (1967)*, 8(12): 1251–1256, 1974.
- R. Udisti, A. Bazzano, S. Becagli, E. Bolzacchini, L. Caiazzo, D. Cappelletti, L. Ferrero, D. Frosini, F. Giardi, M. Grotti, et al. Sulfate source apportionment in the ny-ålesund (svalbard islands) arctic aerosol. *Rendiconti Lincei*, 27(1):85–94, 2016.

WMO. Gaw report no. 183, operations handbook - ozone observations with a dobson spectrophotometer, 2008. URL <https://www.wmo.int/pages/prog/arep/gaw/documents/GAW183-Dobson-WEB.pdf>.

7. Danksagung

An erster Stelle möchte ich meinen Betreuern Christoph Ritter und Prof. Bernhard Mayer danken, die mir immer mit Rat und Hilfe bei Seite standen, neue Anregungen gegeben haben oder auch den einen oder anderen kritischen Blick auf die Ergebnisse geworfen haben, aber auch geholfen haben, relevante Fragen für den weiteren Verlauf der Arbeit zu stellen.

Ebenfalls möchte ich den drei Überwinterern der deutsch-französischen Station AWIPEV in Ny-Ålesund Marine Ilg, Rudolf Denkmann und Basile Le Maut danken, die mir Svalbard, die Messgeräte und das Leben in Dunkelheit, Eis und Schnee näher gebracht haben. Durch euch habe ich erfahren, warum Polarforschung so wichtig ist und welche Herausforderungen es vor Ort zu bewältigen gibt. Ihr habt mir einen guten Überblick über die Vermessung von Eis, Schnee, Permafrost, Ozean und der Atmosphäre mit zahlreichen, verschiedenen Instrumenten verschafft.

Mein großer Dank geht auch an Christoph Ritter und Marion Maturilli, die mir überhaupt einen insgesamt zweimonatigen Aufenthalt in der Arktis ermöglicht haben.

für die zahlreichen Fragen zur Bedienung von Sonnen- und Sternphotometers möchte ich ganz besonders Siegrid Debatin danken. Du warst immer und überall für mich erreichbar und standest mir mit Rat und Tat zur Seite.

für den operativen Betrieb und die anschließende Auswertung des Sternphotometers möchte ich mich besonders bei Lionel Doppler vom Deutschen Wetterdienst in Lindenberg bedanken. Eine Hilfe bei der Technik und Kleinigkeiten bei der Software hat mir der ehemalige Entwickler des Sternphotometers, Karl-Heinz Schulz, gerne zukommen lassen.

Außerdem möchte ich Ralf Jaiser und Sandro Dahlke für die Unterstützung mit ERA-Interim Daten danken. Durch euch wurde erst die Trajektorienanalyse und der Einfluss der gemäßigten Breiten auf die europäische Arktis möglich.

Natürlich möchte ich mich bei der gesamten Sektion Physik der Atmosphäre für angeregte Diskussionen, nette Abende, zahlreichen Kaffee- und Kuchenrunden bedanken. Ihr habt alle dazu beigetragen, dass ich mich in Potsdam wohl gefühlt habe.

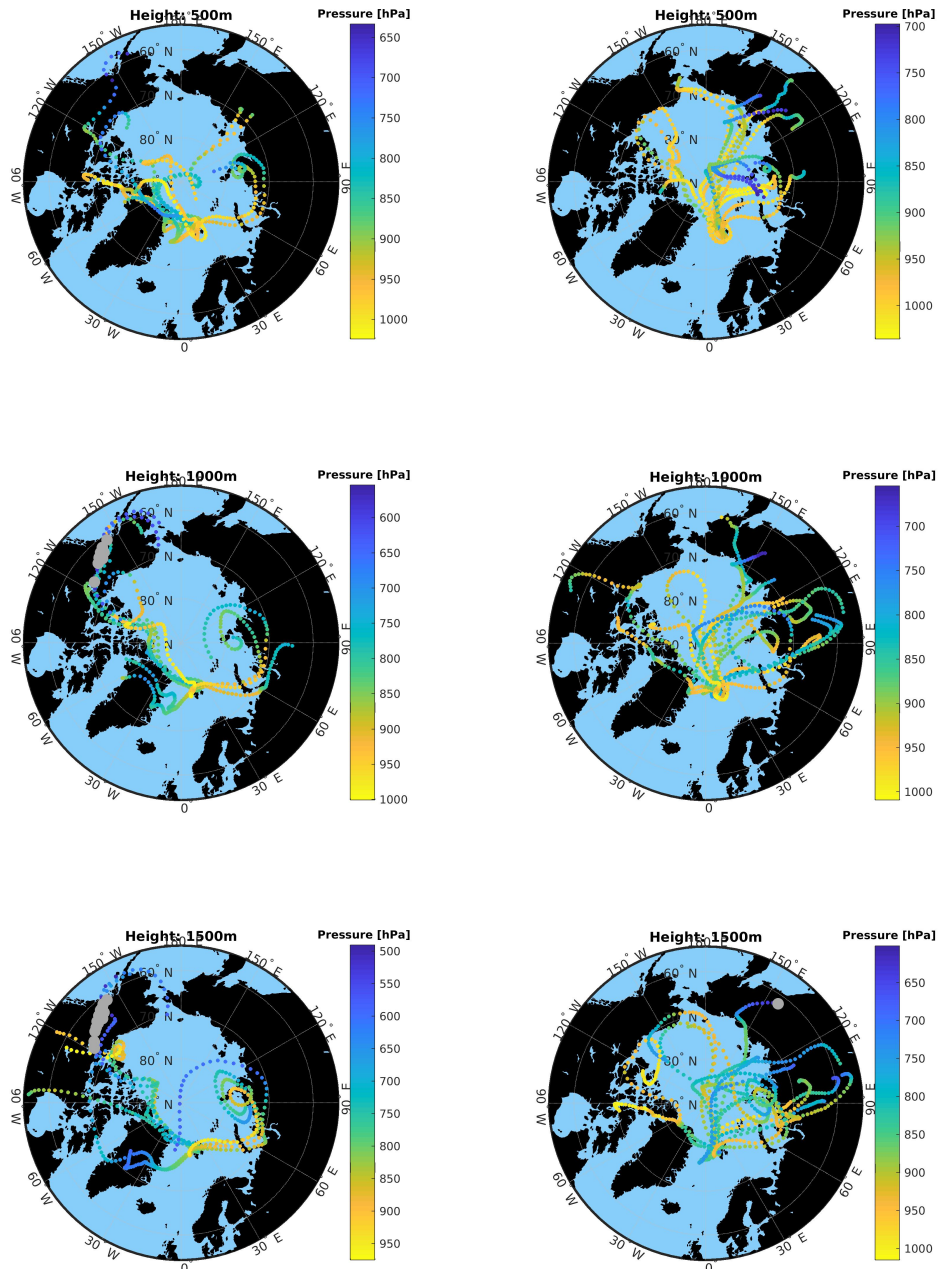
Zu guter Letzt möchte ich mich bei Heidemarie Seibert, Christoph und Zully Ritter, Gundrun Weichbrodt und Hans-Joachim Wersin-Sielaff bedanken. Ohne eure Unterstützung und Spontaneität hat der doch ziemlich holprige Start in Potsdam eine äußerst schöne Wendung genommen.

Selbstverständlich waren meine Eltern und meine Familie unter anderem ausschlaggebend für den Erfolg der Arbeit. Ohne sie wäre der Aufenthalt in Potsdam nicht möglich gewesen. für die sprachliche Unterstützung möchte ich mich zu guter Letzt noch herzlich bei meiner Schwester bedanken.

A. Appendix

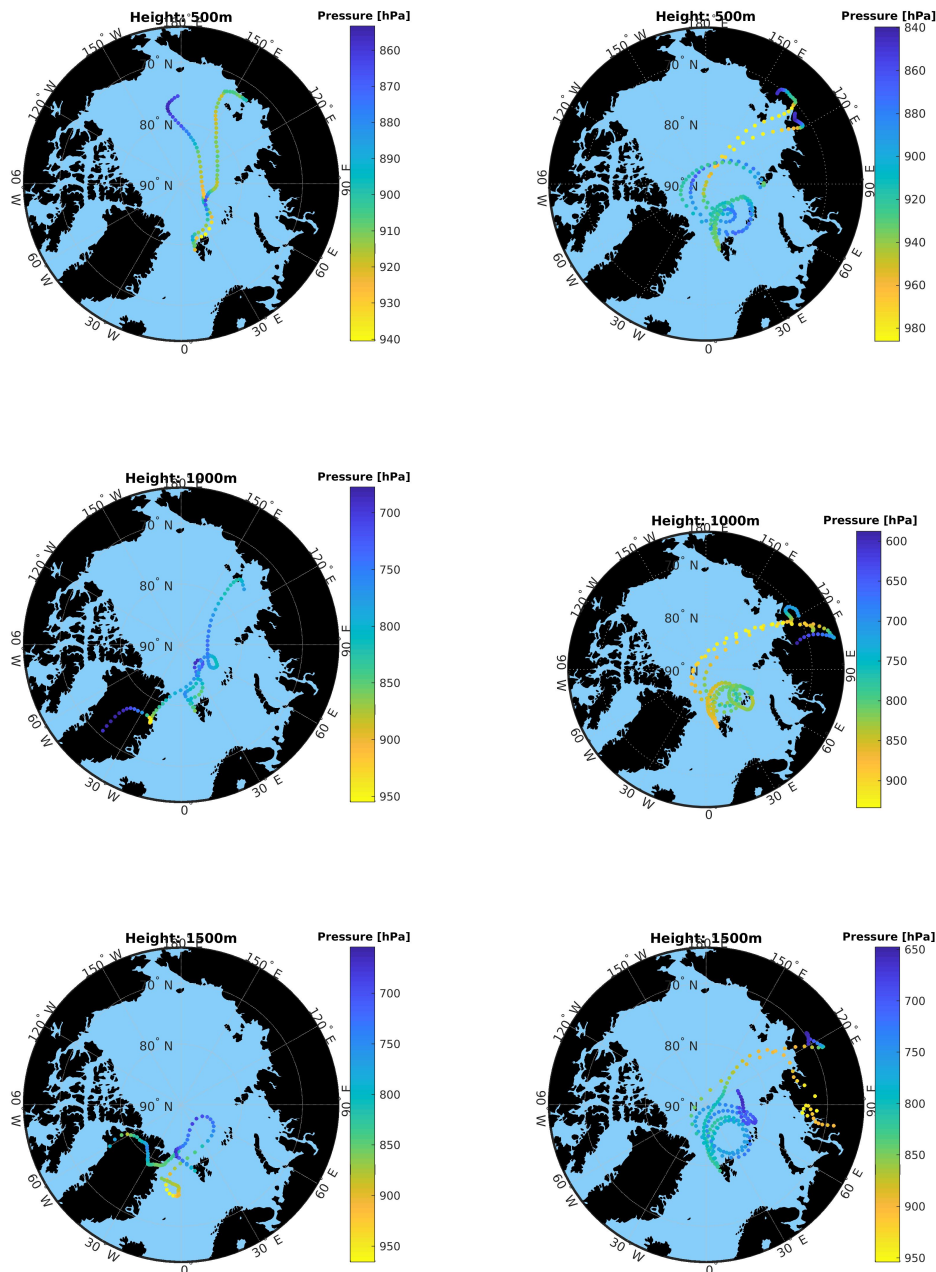
In the following 5-day FLEXTRA back-trajectories are plotted for every height (500, 1000 and 1500m). They are also distinguished by the AOD when arriving in Ny-Ålesund. The left side is always associated with low AOD, the right side with high AOD.

April 2013:



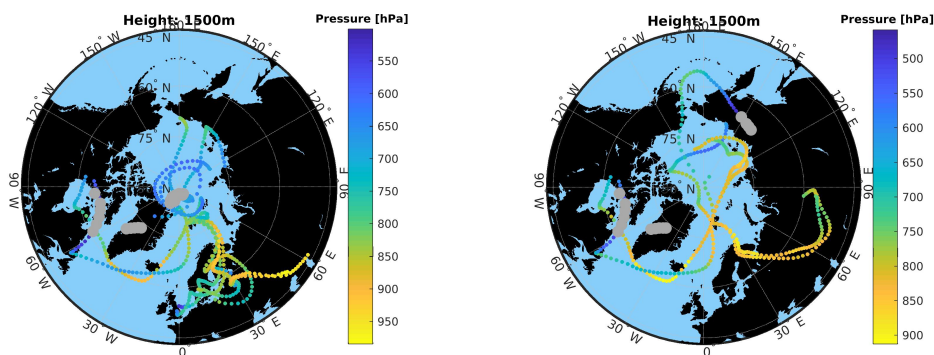
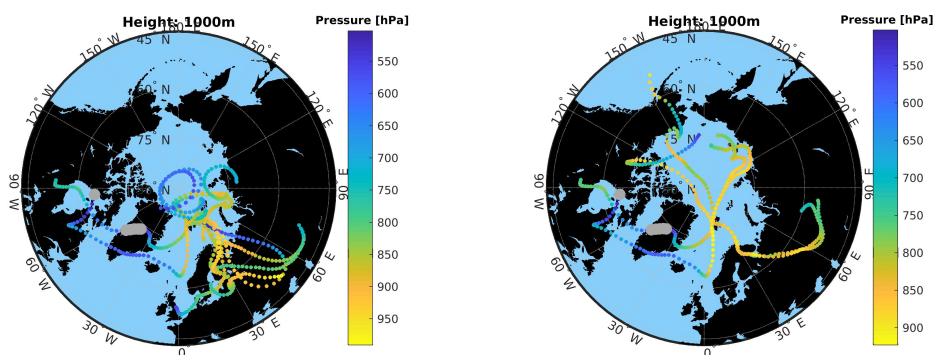
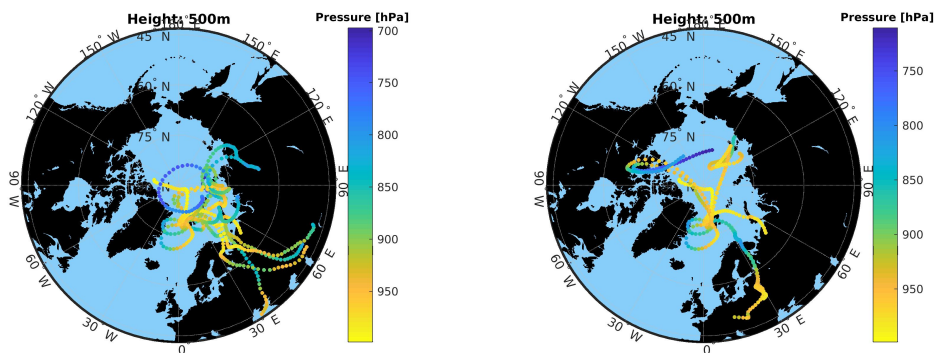
A. Appendix

April 2014:



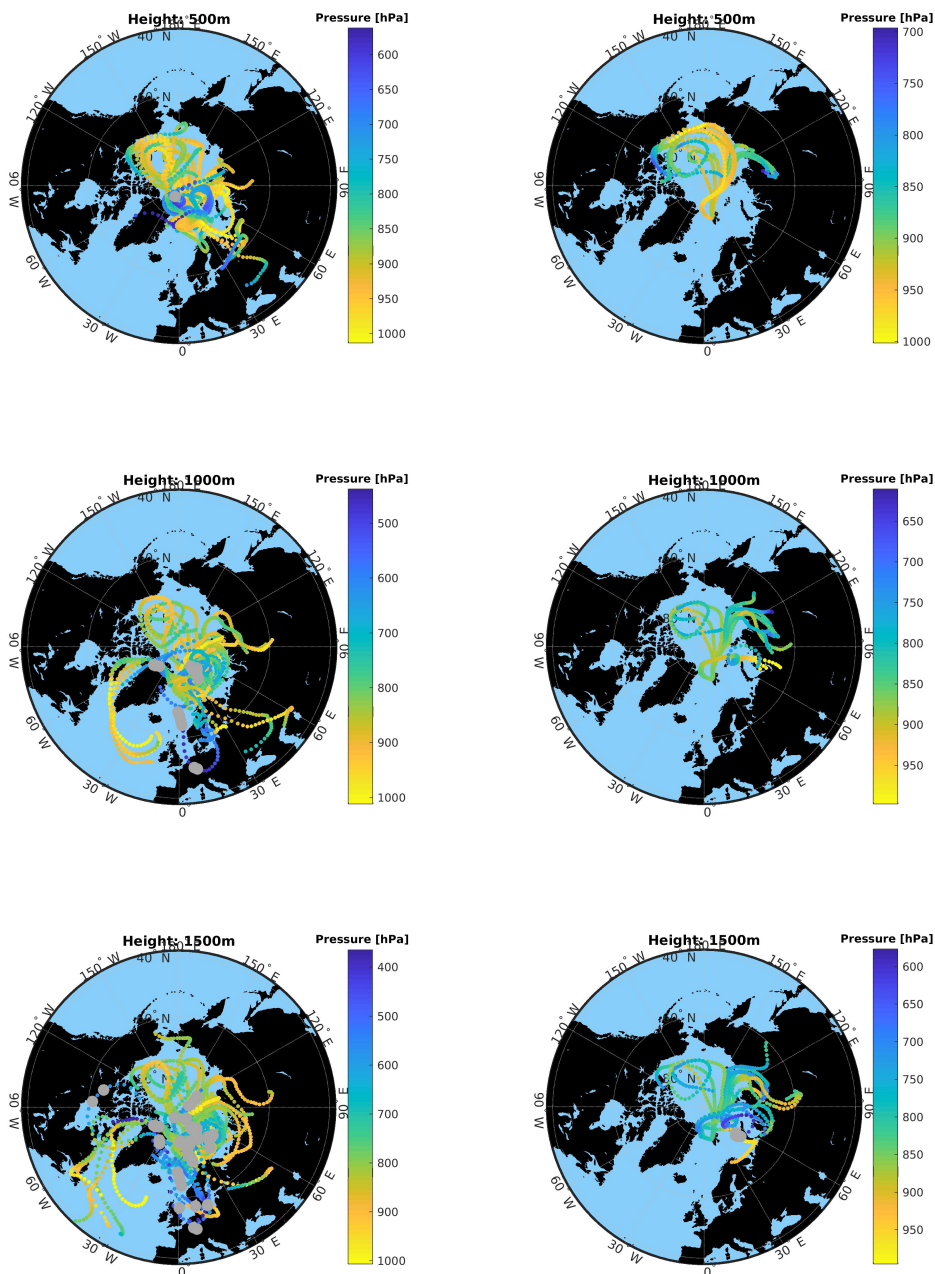
A. Appendix

April 2015:



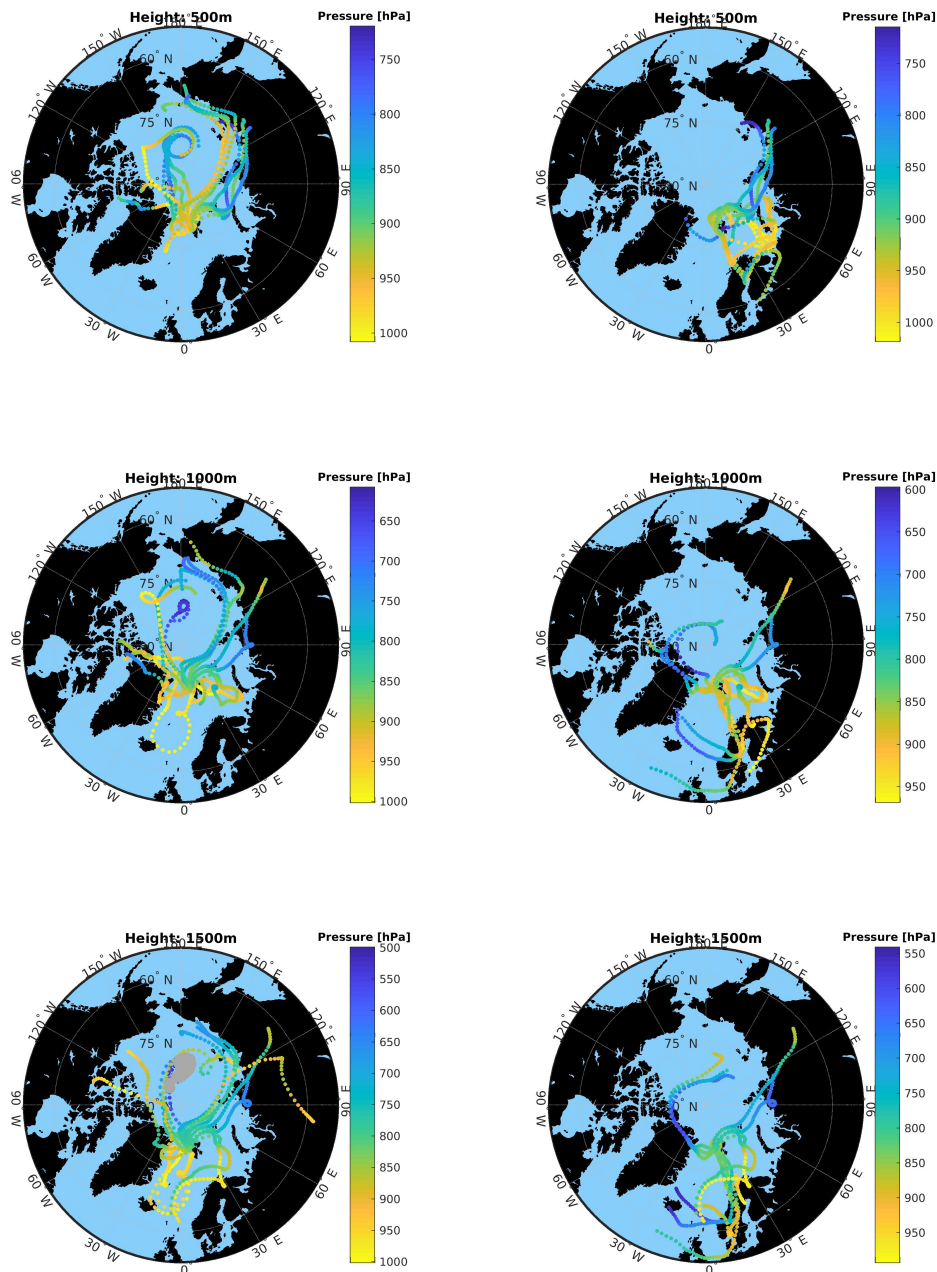
A. Appendix

April 2016:



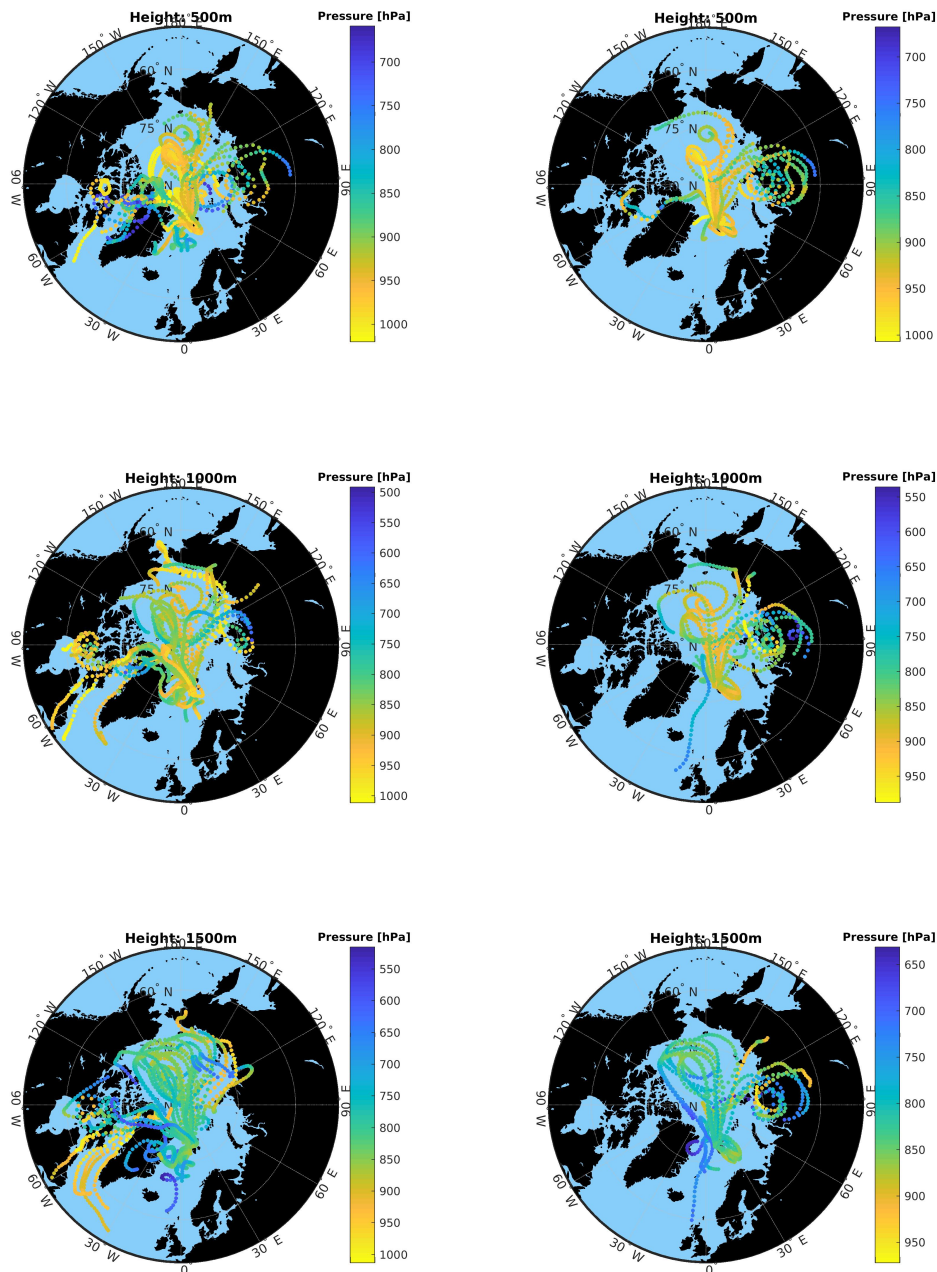
A. Appendix

August 2013:



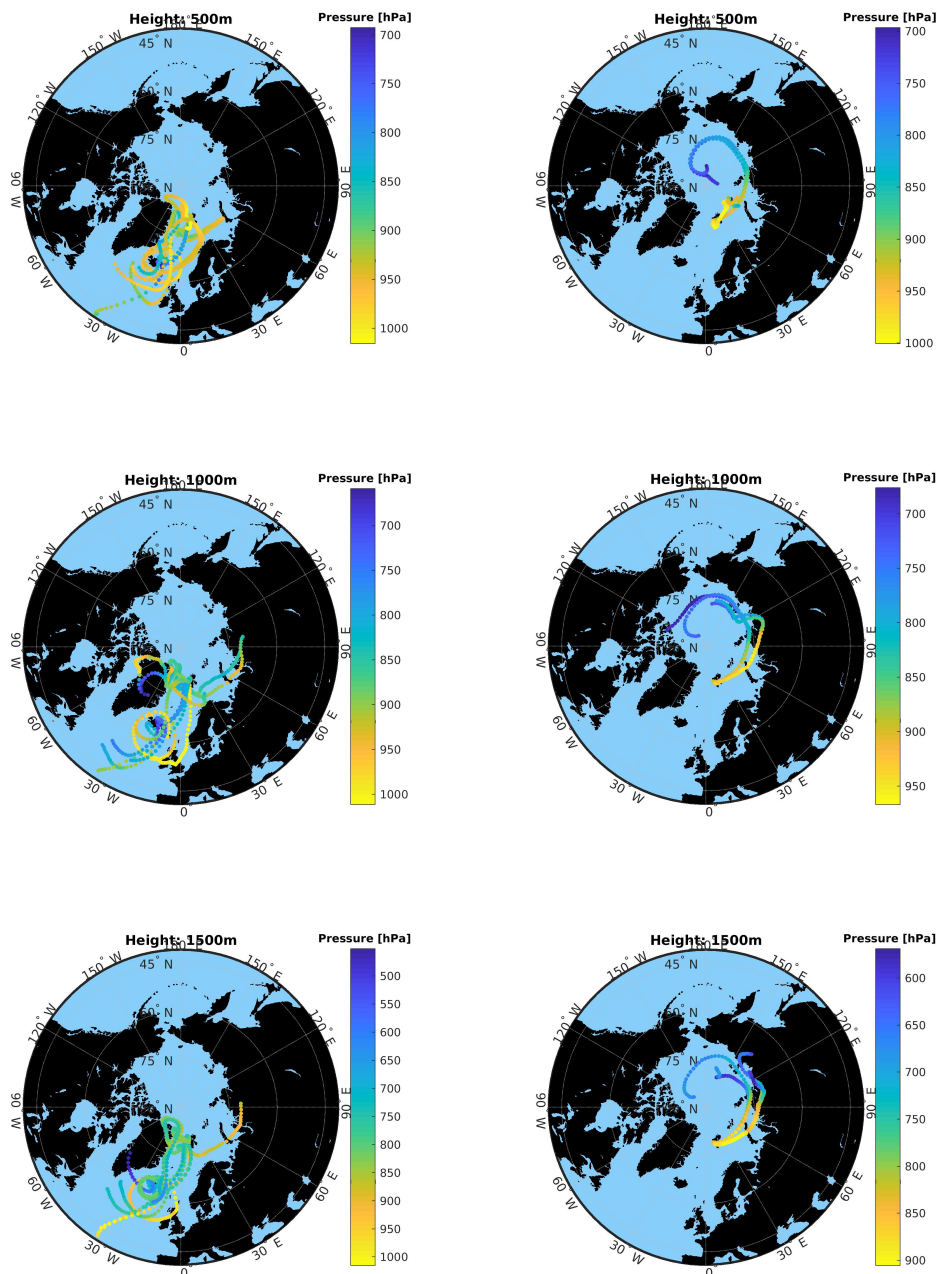
A. Appendix

August 2014:



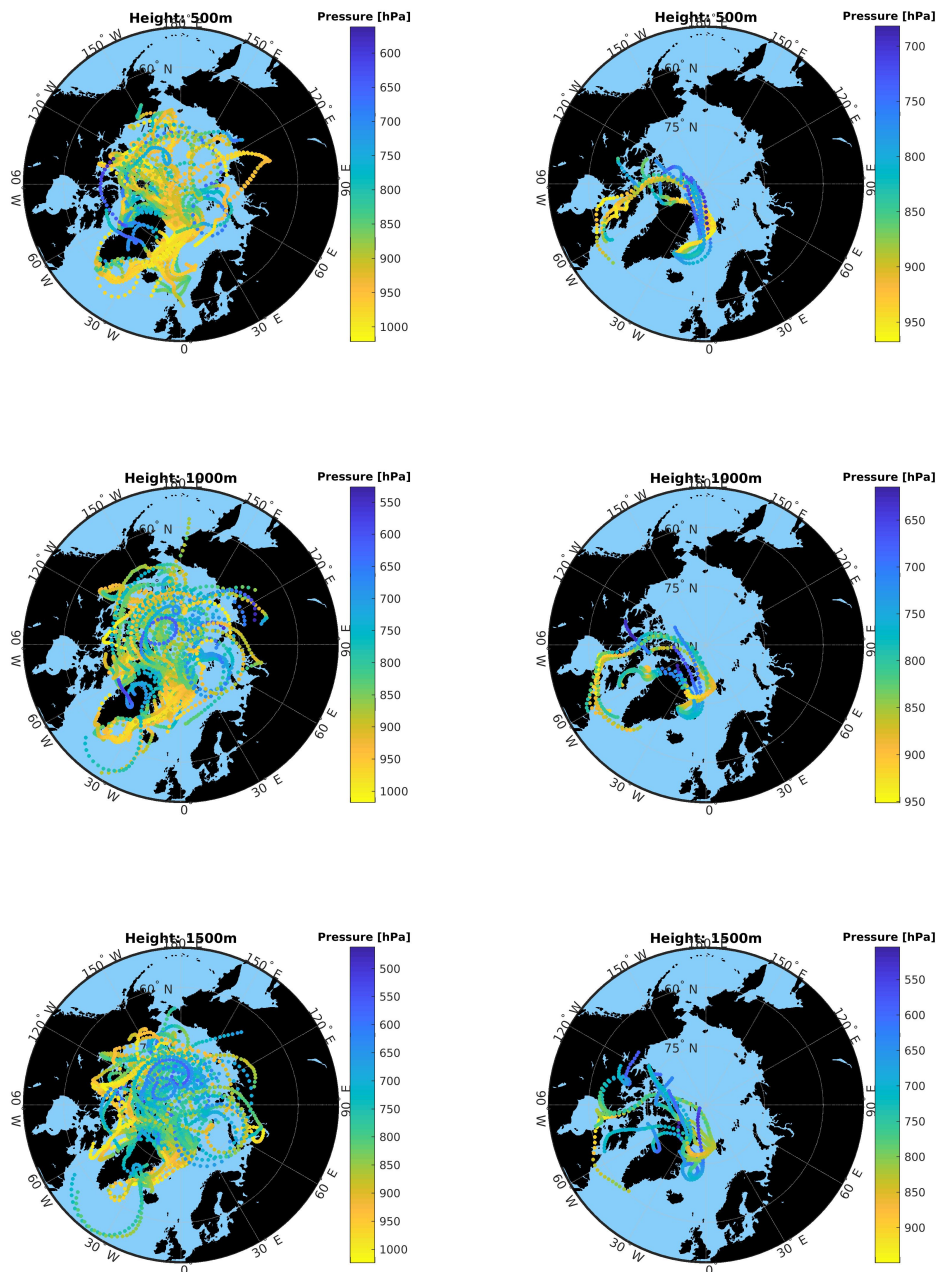
A. Appendix

August 2015:



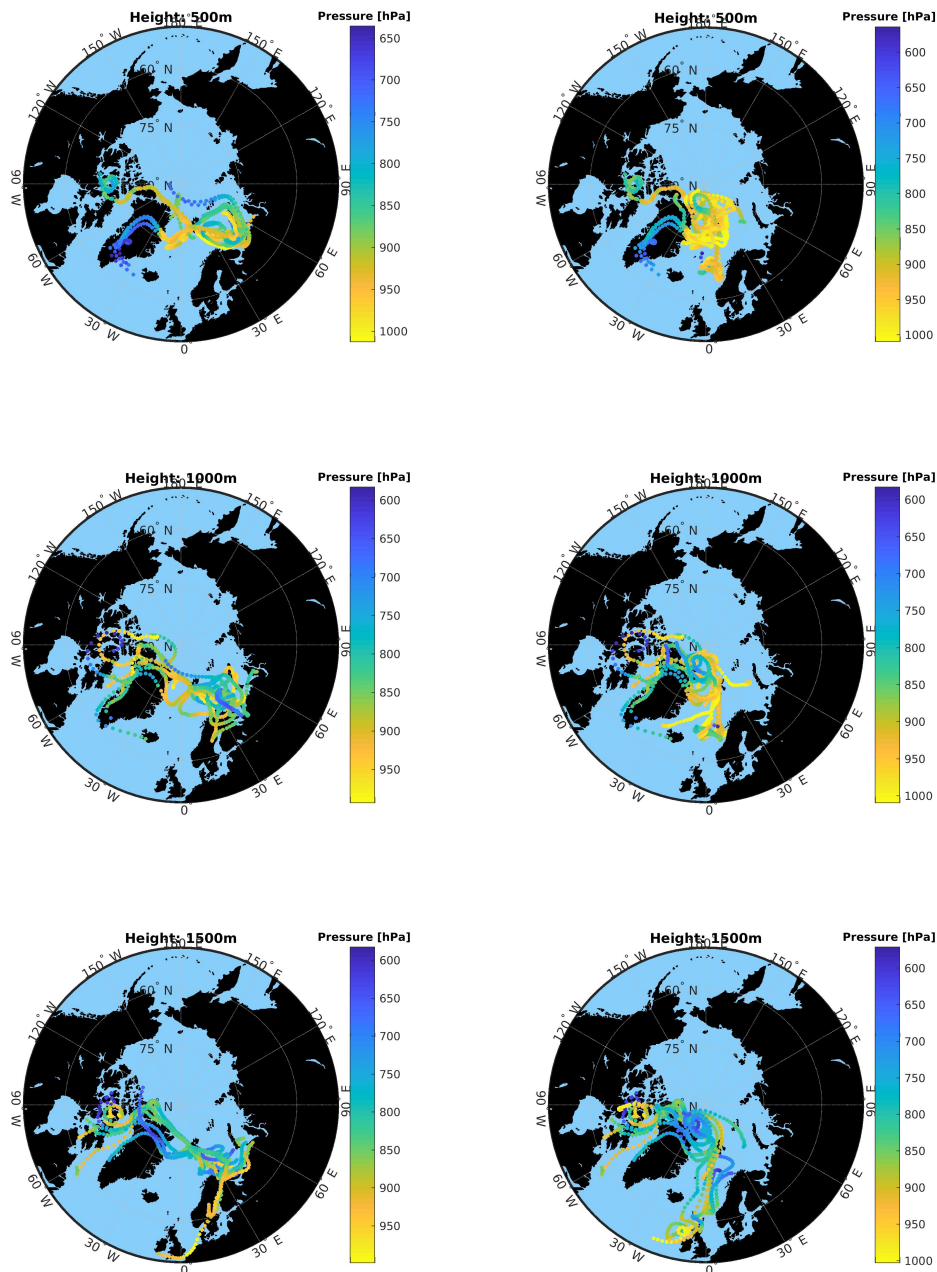
A. Appendix

August 2016:



A. Appendix

August 2017:



B. Abbreviations

Physical quantities

A	Ångström exponent
Aer	aerosol
a	monochromatic extinction
α, β	parameters of wavelength dependent Ångström exponent
b	backscatter ratio
CN	residual counts of photons
χ^2	fitting accuracy
λ	wavelength
LR	Lidar ratio
m	air mass
M	stellar apparent magnitude
O_3	ozone
Ray	Rayleigh
r_{eff}	effective radius
ρ	Pearson's empirical correlation coefficient
τ	optical depth
θ	solar zenith angle
AOD	aerosol optical depth
BL	Boundary layer
CCN	cloud condensation nuclei
FWHM	Full Width Half Maximum
IR	near-infrared part of electromagnetic spectrum (700nm...1070.5nm)
PSC	Polar Stratospheric Clouds
PW	Precipitable Water
VIS	visible part of electromagnetic spectrum (349.7nm...700nm)

Instruments and organisations

DWD	Deutscher Wetterdienst
FLEXTRA	FLEXible TRAjectory model
GRUAN	Global Climate Observing System Reference Upper-Air Network
Lidar	Light Detection And Ranging
MPL	Micropulse Lidar
WMO	World Meteorological Organization

Erklärung

Hiermit erkläre ich, die vorliegende Arbeit selbstständig verfasst zu haben und keine anderen als die in der Arbeit angegebenen Quellen und Hilfsmittel benutzt zu haben.

Ort, Datum

Unterschrift